Changes in runup characteristics between swash and collision conditions

a Field Study

T. Dijkstra

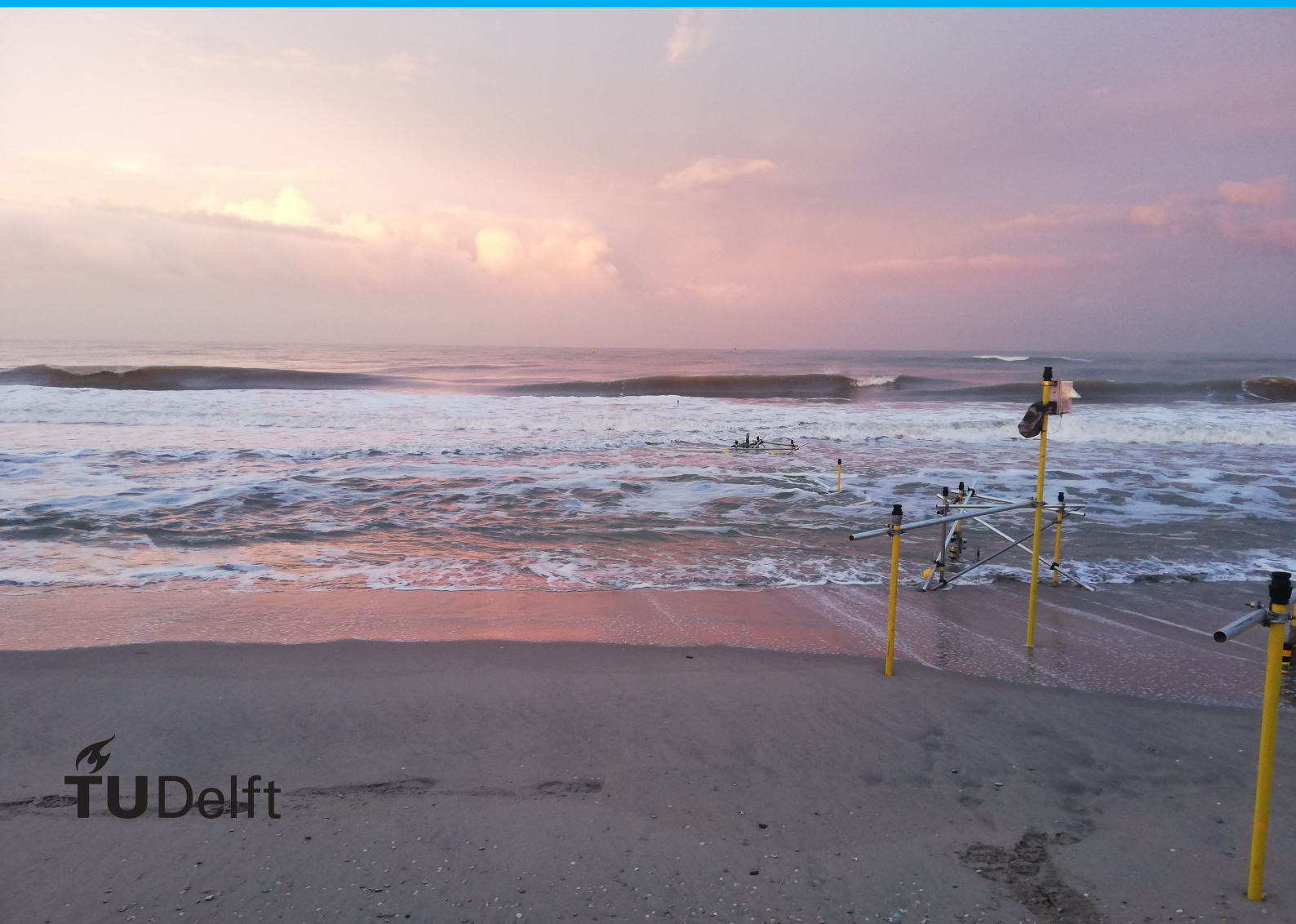

TU Delft

A field study about changes in runup characteristics between swash and collision conditions

a Master Thesis

by

T. Dijkstra

to obtain the degree of Master of Science
at the Delft University of Technology,

Student number: 4723988
Project duration: October , 2021 – September, 2022
Thesis committee:
Dr. ir. S. (Sierd) de Vries, Assistant professor Coastal Engineering
Dr. ir. M. F. S. (Marion) Tissier, Assistant professor Ocean Waves
Dr. ir. J. (Jantien) Rutten, Post doctoral researcher
Ir. P. (Paul) van Wiechen, PhD Candidate
Dr. ir. R. (Ryan) Mieras, Assistant Professor of Coastal Engineering, UNCW

TU Delft

Abstract

Estimating wave runup is of crucial importance during a coastal risk assessment. Currently, runup levels are usually calculated using empirical formula derived from experiments conducted at beaches all over the world, and during different beach states. During this research, conditions are analyzed where runup reaches the dune toe and above. The main objective of this research is to examine the changes in the runup characteristics, which are the wave setup, the infragravity swash motions (low frequency wave motion) and the incident swash motions (high frequency wave motion).

In order to examine these conditions, a fieldwork experiment has be conducted at the Sand engine near Kijkduin (South Holland). a dune of 150 (m) in width and 5.5 (m) above NAP (Nieuw Amsterdams Peil) have be constructed near the waterline. Instruments have been installed which have monitored the incoming wave conditions and the behavior of the hydrodynamic conditions at the waterline. One of these instruments was an instrument new to measurements conducted at the coast. This was a LLC (Line scanning Low Cost) LiDAR, which was used to track the runup during extreme wave conditions. The LLC LiDAR was evaluated in terms of measuring the nearshore hydrodynamics by comparing the water level measured by the LLC LiDAR to the water level measured by a pressure sensor. The water levels from both instruments compared well with an R^2 ranging from $R^2 = -0.86$. The match in the peaks of the water levels were lower, showing R^2 in the range of $0.34 - 0.78$.

Data from the Fieldwork Experiment showed an increase in incident swash wave height during collision conditions when compared to swash conditions. Although the nearshore wave field showed similar conditions between the swash and collision conditions, the swash height showed an increase. Several parameters have been investigated to find the dependence of runup height to the offshore wave or beach characteristics. A best fit is found between runup and the beach slope ($R^2 = 0.86$), also indicating that swash motions are significant. Runup heights during these conditions are also compared to an empirical runup formula. This comparison indicated that runup elevations could still be predicted during conditions where runup reaches above the dune toe elevation.

Preface

This Thesis touches upon the transfromation of the runup characteristics during swash and collision conditions. The behaviour of runup and the interaction with the dune face is yet to be understood, and with an increasing importance of accurate runup predictions due to the increase in coastal flood risk, the assesment of the runup behaviour needs to be well understood.

I would like to thank my supervisors for Paul, Sierd, Marion, Jantien and Ryan. Sierd for his supervision and perspective. Marion for her critical thinking and supportive nature. Jantien for her many insights and helpful ideas. Ryan for his passion for LiDAR's and his many technical insights. And especially Paul for his continuous enthusiasm and moral support.

But also many thanks to my family and friends for their moral support, which without this project would have never existed.

T. Dijkstra
Delft, September 2022

Contents

List of Figures

List of Tables

1

Introduction

This chapter gives an introduction into the research topic and defines current day problems withing the field of research. Background information is given and research objectives are formed from the knowledge gaps presented in the chapter.

1.1. Problem definition

Coastal systems in the Netherlands are mainly composed of sandy beaches with dune systems behind them. One of the functions of the dutch dune systems is to protect the hinterland with coastal protection. In the hinterland resides around 60% of the Dutch population, thus a breach of the dune system can have large consequences in terms of safety and economic assets for the people living in the hinterland.

Expanding insight into the governing processes that cause dune erosion can improve the effectiveness of flood preventive measures. An important parameter in determining the coastal safety of a dune system is the runup level (R), which is widely used in the assessment of predicting storm intensity (Asbury H. Sallenger, 2000, Pinault et al., 2020). Correct predictions of the runup height will provide more insight into the processes governing runup excursion and can improve the accuracy of future dune erosion models.

Figure 1.1: The image shows a runup around the dune toe of an eroded dune face. Hydrodynamic action causes dune erosion and can cause a retreat of the coastal system and can reduce flood safety.

1.2. Coastal systems

Waves approaching the coast will deform (become increasingly skewed and asymmetric) and dissipate towards the coast by wave breaking, and the magnitude of dissipation and the breaker type are influenced by the coastal system (Davidson-Arnott et al., 2019). The coastal profile can be separated into different sections. Also, certain processes that characterize this coastal profile can be identified by parameters like the Dean parameter and the Irribarren number. Changes in the coastal profile during these sections can influence the runup behaviour on the beach.

Coastal profile:
The coastal profile can be separated into 5 different sections which are, going from offshore to onshore, the deep water region, the lower shoreface, the upper shoreface which is also called the surf zone, the beach and finally the dune system (Clifton, 2005, Hoekstra and Stolk, 1990 and Holthuijsen, 2010). The first three sections (deep water, lower shoreface and upper shoreface) are regions in the coastal profile which are always under water, and can be separated by two depths. The closure depth (d_{out}),

and the transition depth (d_{in}) respectively (Hallermeier, 1980). The closure depth is the water depth above which waves do not interact with the seabed under average wave conditions, and corresponds to the offshore limit of the shoreface. The transition depth is the water depth which separates the lower from the upper shoreface. In deep water, waves are not influenced by the seabed. When waves enter the lower shoreface, waves start to get affected by the interaction with the seabed and will start shoaling and refracting. In the upper shoreface, waves will break and dissipate (Clifton, 2005). The hydrodynamic and aeolian processes are separated by the waterline, which is continuously changing due to the tide and storm set-up. The first landward area is the beach, which is an area where during calm conditions most of the swash processes are happening. The beach and the dune system are separated by the dune toe (d_{toe}), which signifies a quick steepening of the coastal profile towards the dune system.

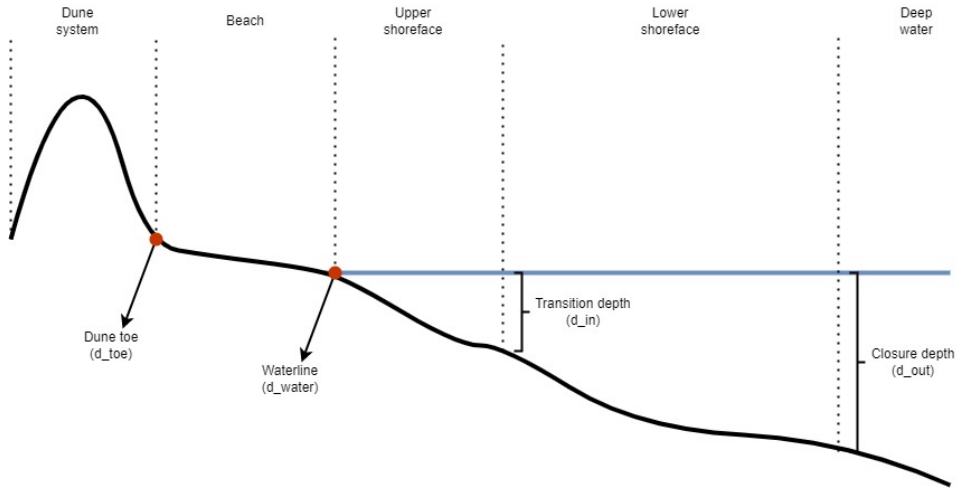

Figure 1.2: In this schematized figure, the coastal profile is characterized into 5 different regions. From right to left, the deep water region, the lower shoreface, the upper shoreface ,the beach and the dune region. The location of the closure depth (d_{out}) and the transition depth (d_{in}) are visible, as well as the location of the waterline and the the dune toe are visible as well.

Beach state

In the upper shoreface, the beach profile can be highly variable in different hydrodynamic conditions, since low energy waves will cause the shoreface profile to steepen and high energy waves will cause the shoreface to flatten (Davidson-Arnott et al., 2019). A steeper foreshore profile tends to be more reflective compared to a flatter foreshore, which will have a more dissipative behaviour. To be able to distinguish between the beach type, the Dean parameter (Ω) can be used (Dean, 1973). The Dean parameter gives the equilibrium shoreline response from the offshore conditions.

$$\Omega = \frac{H_s}{\omega T_p} \tag{1.1}$$

In which H_s is the significant wave height, ω is the sediment fall velocity and T_p is the peak spectral wave period. The sediment fall velocity is closely related to the beach slope (Davidson-Arnott et al., 2019). Beach types can be classified as follows.

- $\Omega \leq 1$ are reflective beaches;
- $1 \leq \Omega \leq 6$ are intermediate beach types;
- $\Omega \geq 6$ are dissipative beaches.

Breaker type

Another parameter to determine the beach response is the Iribarren number (ξ), also called the surf similarity parameter, which classifies the breaker type of the beach (Battjes, 1974). The formula for deriving the Iribarren number has three variables that determine the beach state, namely, the beach slope ($tan\beta$), the offshore wave length (L_0) and the wave height (H), which results in the formula.

$$\xi = \frac{tan\beta}{H/L_0} \tag{1.2}$$

Wave height can be expressed as the offshore wave height (H_0) or the breaker wave height (H_b) which is the height of right before it collapses. The combination of H_0/L_0 can also be written as the offshore wave steepness (s_0).

In the study of Battjes, 1974, the Iribarren parameter identifies four different breaker conditions. The first condition ($\xi \leq 0.5$) generated a spilling beaker type wave. The second condition ($0.5 \leq \xi \leq 3.3$) a plunging breaker, the third and fourth conditions ($\xi \geq 3.3$) a collapsing breaker or surging breaker type wave. These breaker types are schematized in figure 1.3.

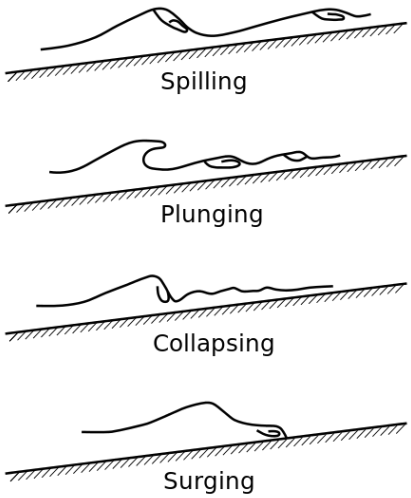

Figure 1.3: Iribarren parameter. From top to bottom, spilling breakers occur at $\xi \leq 0.5$, plunging breakers at $0.5 \leq \xi \leq 3.3$, surging or collapsing breakers at $\xi \geq 3.3$ using the offshore wave height version of the equation (Asbury H. Sallenger, 2000).

Thornton and Guza, 1982 found that the Irribarren parameter can be linked to the amount of wave dissipation present at the beach. This has later been confirmed by Ruggiero et al., 2004. Low Irribarren parameters have been linked to high wave dissipation on the beach, whilst high Irribarren parameters indicate low wave dissipation. Dissipation mainly takes place for waves in the incident wave band (waves with frequencies $0.05Hz$ and above). However, some studie have also shown that IG waves could also dissipate (Battjes et al., 2004)

1.3. Storm regimes

Wave impact on coastal dune environments can be separated into 4 storm regimes which all have different physical characteristics.

Swash regime
The first regime is named the ”Swash regime”. It describes the wave attack on the beach, where the run-up of the waves is below the base of the dune. Under these conditions the beach is being eroded by the large waves attacking the beach.

Collision regime
The second regime is named the ”Collision regime”. This is where the waves are colliding with the dune, but are not overtopping the dune ridge. The dune face and beach are being eroded under these conditions, but contrary to the beach, the eroded dune sediment will most likely not be returned to the dune face.

Overwash regime
The third regime is named the ”Overwash regime”. In this regime the dune is being overtopped by waves which can cause water to overflow the dune. This will transport transported sediment to behind

the dune where it will be lost from the coastal beach-dune system.

Inundation regime
The fourth and last regime is named the ”Inundation regime”. This is where the storm induced sea level rise is high enough to submerge the dune. Processes governing this regime are conceptually least understood, but often the entire dune face is completely eroded. This erosion pattern usually takes place in landward direction (Asbury H. Sallenger, 2000).

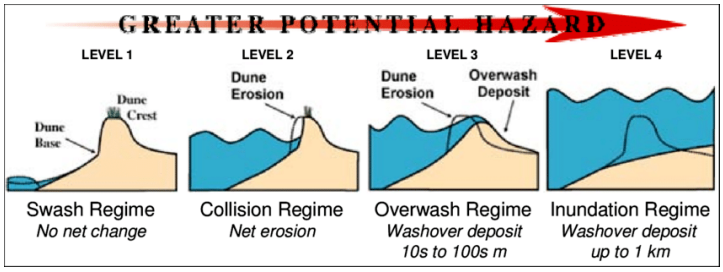

Figure 1.4: Storm regimes from left to right, the swash regime, the collision regime, the overwash regime and the inundation regime (Asbury H. Sallenger, 2000).

1.4. Total water level and runup

Total water level ($h(t)$) is defined as the maximum onshore elevation reached by waves relative to the shoreline when in the absence of waves and setup (Pinault et al., 2020). The total water level can be divided into 5 time varying variables. The tide ($T(t)$), wind setup ($\mu_{wind}(t)$), wave setup ($\mu_{wave}(t)$), and swash induced motion ($S(t)$). The tidal change and wind setup are generated offshore and together form the water level. Both setup levels generally vary in time in the order of hours. The wave setup and swash induced motion are caused by nearshore and wave processes, and together form the runup (R). Dissipation of the waves results in a heightening of the waterline which has a time average and a time varying component. All variables together form equation 1.3.

$$h(t) = \mu_{tide}(t) + \mu_{wind}(t) + \mu_{wave}(t) + S(t) \tag{1.3}$$

As for the runup ($R(t)$), equation 1.3 reduces to Equation 1.4 and **??**. The components $S_{SS}(t)$ and $S_{IG}(t)$ indicate the components of swash ($S(t)$) of the incident waves and infragravity waves respectively.

$$R(t) = \mu_{wave}(t) + S(t) \tag{1.4}$$

Wave setup
Wave setup (μ_{wave}), which is caused by the energy of the waves which is dissipated during wave breaking, causes a rise in water level shoreward of the breaking point of the waves (Longuet-Higgins and Stewart, 1964). The dissipation of the waves, and the accompanying water level changes are related to the radiation stresses. Meaning that wave momentum, which is present in the orbital motion of the waves, is transferred to the water level. In other words, there is an equilibrium net force in shoreward direction (waves cannot pass the beach and dune). This means the in going force is equal to the outgoing force over the domain. For an overview, look at Figure 1.5.

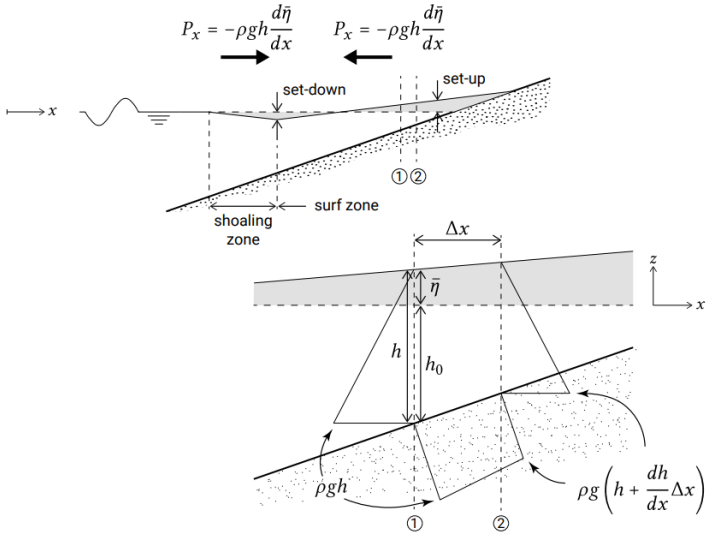

Figure 1.5: This figure shows a schematized version of radiation stresses in the surf zone. Momentum balance is assumed in this region, meaning incoming forces are equal to outgoing forces. Since waves travelling in shoreward direction bring momentum towards the waterline, the water level increases at the waterline to counteract the shoreward momentum, (Longuet-Higgins and Stewart, 1964)

Going from the location where the first waves are breaking, until the waterline, the wave set-up can be calculated using equation $\mu_{wave} = -\frac{3}{8}\gamma^2 h + C = -\frac{3}{8}\gamma^2(h_b - h)$. This can be solved for the the setup at the waterline, where the maximum set-up is located. This is where almost all energy of the waves has been dissipated. The equation can be simplified at the waterline into equation 1.5.

$$\mu_{wave} = \frac{5}{16}\gamma H_b \tag{1.5}$$

Within these equations there are two variables which determine the set-up height. The first parameter is the wave height during breaking, H_b. The second parameter is the breaker index (γ_b), which is a ratio of breaking wave height over water depth 1.6 (Battjes, 1974).

$$\gamma = \frac{H_b}{h_b} \tag{1.6}$$

Swash action

Swash (S), is the up and down propagation the bores generated by breaking waves. This fluctuation motion is caused by incoming incident (INC) waves and infragravity (IG) waves (Stockdon et al., 2006, Guedes et al., 2013 and Davidson-Arnott et al., 2019). The location of the swash zone is the area within the maximum uprush and downrush, and is a very dynamic part of the beach in terms of hydrodynamic and morphological changes (Guedes et al., 2013 and Elfrink and Baldock, 2002).

INC are wave periods within a band range of $f_{INC} \leq 0.005Hz$ are the generators of the short period swash component (S_{INC}). These waves can be classified under wind waves and swell waves (Davidson-Arnott et al., 2019). Wind waves are generated offshore by local wind fields and form relatively steep and irregular wave fields. Sea swell waves are generated by far away wave fields which have a more regular and unidirectional wave pattern. Previous studies relate the short period swash component to β_f, H_0 and L_0, with the '$_0$' indicating offshore statistics (Stockdon et al., 2006).

IG waves are large period waves with periods with a band range of $0.05Hz \leq f_{IG} \leq 0.004Hz$, which are directly or indirectly formed by sea swell wave groups (Longuet-Higgins and Stewart, 1962) and form the long period swash component (S_{IG}). In the offshore region, IG waves are generated by a slight difference in wave period between SS waves in the wave field (Bertin et al., 2018). The addition of the wave amplitudes of the wave fields causes the total wave amplitude to increase when the waves

are in phase, and to decrease when the waves are out of phase. These IG waves are named bound long waves. The addition or subtraction of the short wave field causes a change in the energy balance. Energy from the water level is transferred to the wave height when the short waves increase due to the addition of the waves when they are in phase, and energy from the wave height is transferred to the water level when the waves are out of phase. This change in water level due to the energy transfer generates bound IG waves. The process is visualized in figure 1.7. The IG swash component is mainly influenced by H_0 and L_0 according to (Stockdon et al., 2006), which leaves the beach slope (β_f) absent compared to the incident wave component.

better not to talk about an energy balance here. Again, as for setup/setdown, we are looking at changes in radiation stress, so changes in wave-induced momentum.

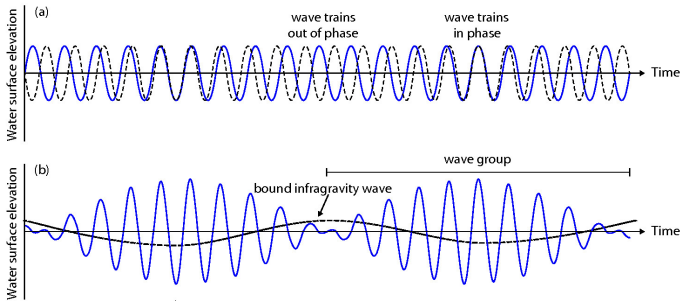

Figure 1.6: This figure is an example of an IG wave generated by a bi-chromatic SS waves field. The top of the figure shows the SS wave groups Independently. The bottom figure shows the sum of the wave fields and the resulting IG wave (Holthuijsen, 2010).

In the nearshore behaviour of IG waves there are two important processes that are associated to their behaviour. Namely, the release of the bound long wave, the variation of the breaking point mechanism and the merging of bores in the swash zone. The first mechanism, the release of the bound long wave, is caused by the offshore generated bound long waves (Bertin et al., 2018). When bound long waves reach the upper shoreface, the incident waves start to break and transfer their energy to the long waves, which will create free long waves (Bertin et al., 2018). A complete image of the bound to free long wave process is schematized in figure 1.7.

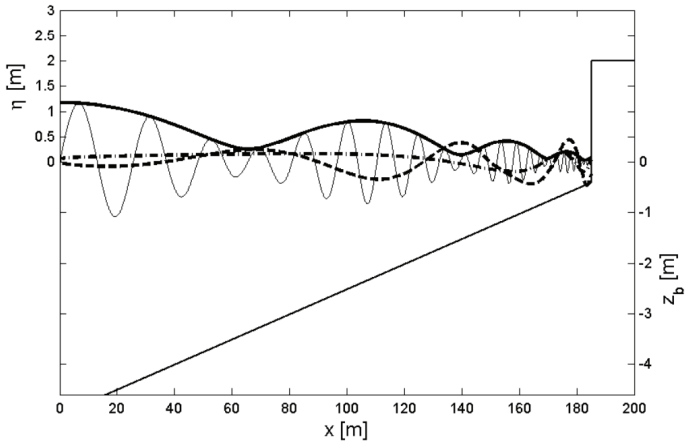

Figure 1.7: The figure shows the SS waves (thin solid line) and the wave envelope (thick solid line). As a results of the incoming SS waves, bound long waves are generated which are transformed to free long waves (dotted line), (van Gent et al., 2008).

The second mechanism causing IG is caused by the variation in the breaking point of the short waves (see location of x_1 and x_2 in figure 1.8). Larger waves break earlier than lower waves. Since the wave grouping causes the the wave height to change over time, there is a time dependent variation of the

breaking point. The magnitude of the radiation sheer stresses alter due to the changes of the wave groups and the breaking point. Looking at the beach slopes, the release of the bound long wave mechanism is strongest on dissipative beaches and the breaking point mechanism is strongest on steep beaches (Battjes et al., 2004).

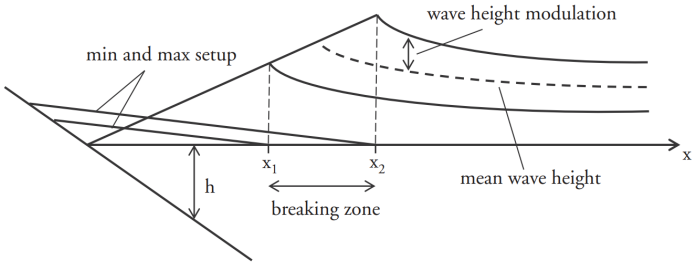

Figure 1.8: Changing location of the breaking point and set-up height due to altering wave height from wave groups. The waterlevel changes resulting from the changing breaker location result in the formation of free long waves (Bertin et al., 2018).

The magnitude of bound and free IG waves can be approximated using Longuet-Higgins and Steward and green's law respectively (Longuet-Higgins and Stewart, 1964 and Battjes et al., 2004). Both approximations relate the deep water long wave height to the wave height in shallower waters. Bound and free IG both have a different dependency on water depth. The depth dependency of bound long waves can be approximated using $\mu_{l,b} \sim h^{-5/2}$, and the dependency for free IG can be approximated using $\mu_{l,f} \sim h^{-1/4}$.

The influence on the runup from INC waves and IG waves depends on the beach characteristics. On dissipative beaches the influence of IG waves is more prevalent, whilst INC waves dominate on reflective beaches. On dissipative beaches, the swash zone of the coastal system is completely saturated with wave breaking. This characteristic has been observed in several studies including Stockdon et al., 2014, van Gent et al., 2008 and Pinault et al., 2020.

1.5. Background Literature

Generally runup is defined as $R_2\%$, which is the runup height which is exceeded only 2% of the time. There are several (empirical) studies that estimate the runup level. These usually include the variables of deep water wave height (H_0), deep water wave length (L_0) and an averaged beach slope (β). One of these was by Stockdon et al., 2006, which derived an equation which separates the three characteristics that dominate in runup elevations (set-up, S_{INC} and S_{IG}). The magnitude of each characteristic is determined by the beach type, like dissipative, mildly sloping or steep beaches. A useful parameter for determining the beach type is the Irribarren number, as mentioned in section 1.2. When the Irribarren number is below 0.3, a dissipative beach can be assumed. During this research, the Irribarren number is always below 0.3, thus the assumption of a dissipative beach can be made. In dissipative beaches, IG wave action is dominant over the swash action by the SS waves, thus equation 1.8 can be used to calculate the runup (Stockdon et al., 2006). In this simplified equation from Stockdon et al., 2006, beach slope has been omitted the full equation.

$$R_{2\%,P} = 1.1\left(0.35\beta_f (H_{0,eff}L_0)^{1/2} + \frac{[H_{0,eff}L_0(0.563\beta_f^2 + 0.004)]^{1/2}}{2}\right) \tag{1.7}$$

$$R_{2\%} = 0.043(H_0L_0)^{1/2} \tag{1.8}$$

1.6. Research objective

Little research has been done for runup predictions during storm conditions where the dune face is being hit by wave attack. In analysis performed by previous research, experiments are not catered towards changing conditions on the same beach, and the maximum runup level does not reach further

than the dune toe, even though the runup level is one of the main drivers of dune erosion. The purpose of this research is to provide insight into the changes of the runup characteristics between the swash regime and the collision regime.

Primary objective

How do the runup characteristics change when comparing conditions in the swash regime to conditions in the collision regime on a dissipative beach?

To answer the primary objective, the following sub questions are formed.

Secondary objectives

1. How can a LiDAR scanner be used to measure runup events on a dune and dune scarp?

Firstly, during data gathering, a LiDAR (Light Detection And Ranging) scanner has been used to measure the total waterline ($h(t)$). Since this is a new instrument, an investigation is needed that shows the applicability if the LiDAR scanner.

2. How does the composition of the runup characteristics change going from a swash regime to the collision regime? And if so, what processes cause these changes?

Secondly, in order to answer the main objective, the magnitude of the runup characteristics (S_{INC} and S_{IG}) relative to each other is investigated. For example, the IG component increases but the INC component remains the same. The cause for these changes is also investigated.

3. How do runup elevations during swash regime, derived using empirical runup formula, compare to measurements derived from a runup camera and a LiDAR instrument?

An lastly, measured runup elevation during swash and collision conditions are compared to the empirical Equation 1.7. The validity of the empirical equation during collision conditions is investigated.

1.7. Thesis outline

This master thesis is divided into 6 chapters which will each will answer certain aspects about the research topic. In Chapter 1, an introduction of the research topic, as well as the problem definition and research scope are elaborated upon. Chapter 2 explains the setup of the research experiment and instrument locations, goes in depth to the gathered data has been processed. In Chapter 3, the processed and parameterized data will be analyzed and compared. In Chapter 4, the results will be discussed and compared to previous work. In Chapter 5, a general conclusion will be drawn from the gathered results. And lastly, in Chapter 6, recommendations will be made for future research within the scope of this topic. In figure 1.9, a flow chart is presented that summarizes the chapter structure and topics.

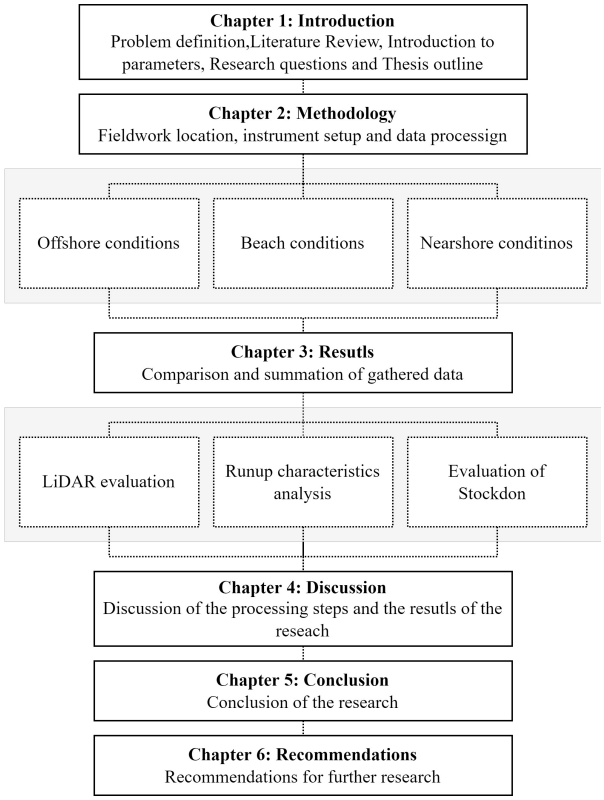

Figure 1.9: Outline of the Msc Thesis. A traditional structure is followed for the report.

2

Methodology

This chapter describes how data has been gathered and processed with the aim of gathering usefull results which can anwser the research questions. At the start of this chapter, an overview of the Field-work Site is given. Then the chapter will follow the reader trough the processing steps taken which transform the raw data gathered to the final results.

2.1. Experimental setup

In order to answer the research questions, measurements are conducted during a fieldwork deployment at the Sand Sngine, located near Kijkduin, South Holland. The experiment took place from November 15th until December 12th and a single deployment on January 5th. During this time, several instruments were used to capture incoming waves in intermediate and shallow water in order to capture the runup characteristics during swash and during collision conditions. The type and location of the instruments used will be elaborated upon in this chapter, as well as the characteristics of the coastal system where the measurements have taken place.

2.1.1. Fieldwork site location

The Fieldwork Experiment was located at the Sand Engine near Kijkduin which is a sand nourishment on the sandy beaches of South Holland. At this site, two dunes of 150m long and 5.5m high relative to NAP (Nieuw Amsterdams Peil) have been mechanically constructed near the waterline on the outer part of the Sand Engine. Since the length of the dune is significant it has been assumed that alongshore uniform conditions apply. For this research, the focus lies on the southernmost dune (see Appendix **??** and Figure 2.1). The other dune is not used in this Master Thesis. A birds eye view of the Field Site is given in figure 2.1. For an overview and location of the field site of the dune, a map is made (Figure 2.2).

Figure 2.1: Birds eye view at the start of the experiment. The nearest dune is dune 1, and the dune further away is named dune 2. At the start of the experiment the duneface still has a gentle slope, but further into the experiment a scarp is formed.

There are three offshore stations which measure the offshore tide wind setup and wave conditions. These are the ”Hoek van Holland”, ”Scheveningen” and the ”Europlatform” (see Figure 2.2). At the locations Hoek van Holland and Scheveningen, tide and wind setup levels are measured. The offshore wave statistics are measured at a depth of $32m$ at the Europlatform. A birds eye view of the field site is given in figure 2.1. For an overview and location of the field site of the dune a map is made (Figure 2.2).

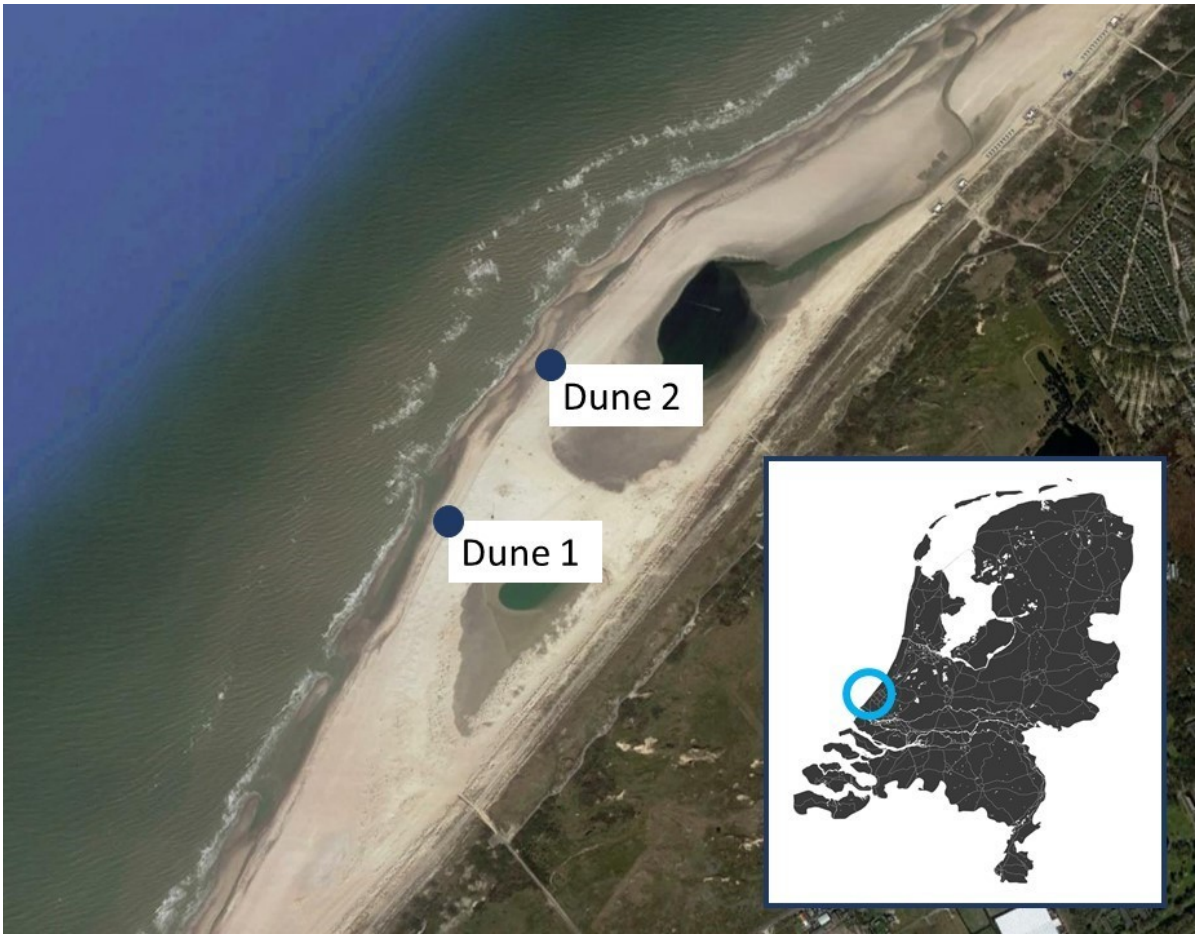

Figure 2.2: The image gives an overview of the sand engine and artificial dunes created for the experiment. The small chart on the bottom right indicates the location of the Sand engine within the Netherlands.

2.1.2. Coordinate systems

The RD (RijksDriehoekscoördinaten) coordinate system and a local cross shore coordinate system have been used in this master thesis. The RD coordinate system is widely used in the Netherlands, and has the dimension E (Easting), N (Norting) and U (Elevation). All the dimensions of the coordinate system are the unit meters, and the elevation in this coordinate system is relative to NAP. The local cross shore coordinate system is introduced to simplify the complex 3D situation to a more manageable 2D system. The The local coordinate system uses the dimensions of the cross shore distance (x) and elevation (z), and is orientated in a cross shore direction to the beach orientation. This means the orientation of the cross shore system is $112\,\mathrm{deg}$ relative to true North. The origin of the coordinate system is:

- $E_{origin} = 71505.885m$
- $N_{origin} = 452293.534m$

The origin is located at the most offshore location of the transect of the cross shore cross shore coordinate system. Figure 2.3 shows an abstract plot of the orientation of both coordinate systems.

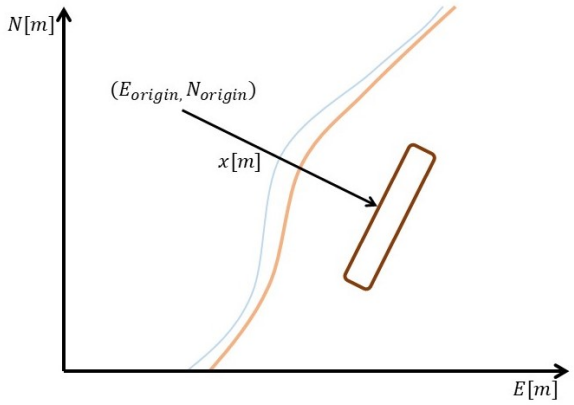

Figure 2.3: An abstract representation of the local coordinate system when plotted in the RD coordinate system together with the origin of the local coordinate system. The orientation of the x-axis of the local coordinate system is $112\ \mathrm{deg}$ relative to true North, which is also relative to the N-axis in the RD coordinate system. The x-axis is directed towards the dune which is indicated with a brown square.

The conversion of the RD coordinate system to the local coordinate system is done using Equation 2.12. In which x is the cross shore location, E are the Eastings of the LLC LiDAR point cloud and N are the Northings of the LLC LiDAR point cloud. Since the orientation of the LLC LiDAR is not exactly cross shore, there might occur small errors from this conversion. But for the sake of this research, this is neglected. This assumption is made since the main interest lies in the height of data, and not the cross shore location. 2.12.

$$x = \sqrt{(E - E_{ref})^2 + (N - N_{ref})^2} \tag{2.1}$$

2.1.3. Nearshore instruments within cross shore transect

Three different types of instruments have been used in this Master Thesis to capture the nearshore hydrodynamics and the beach and dune morphology changes. These instruments are pressure sensors, a runup camera and a LLC (Line scanning Low Cost) LiDAR. Many more instruments have been used during the RealDune/ReFlex Fieldwork Experiment, but these have not been used for this research. The instruments were located at the center of the dune in alongshore direction, and have been placed in the orientation of the local cross shore coordinate system. Every instrument location is measured by a RTK-GPS which measured in the RD coordinate system. The instrument Locations in the local coordinate system at the dune can be viewed in Figures 2.4 and 2.5. During the RealDune/Reflex Fieldwork Experiment, ten different sensor locations were used om the beach during November until December, however, only three locations have been used during this master thesis. These locations have been named L1a, L2a and L3a.

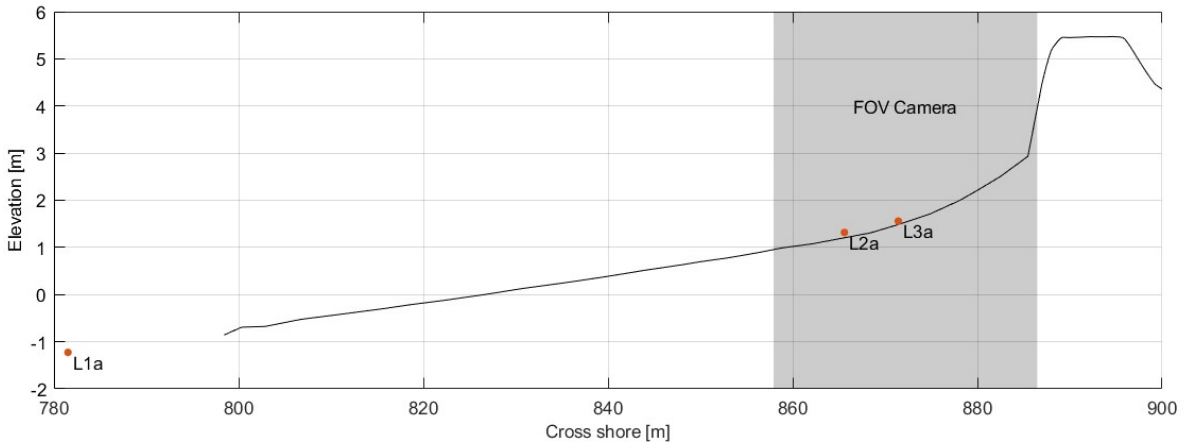

Figure 2.4: The transect with instrument locations L1a, L2a and L2a during the November until December. The filled in gray area indicates the FOV (Field OF View) of the runup camera. The black line is the beach elevation during November 30th.

The instrument locations changed during the January deployment, which resulted in the instrument setup in Figure 2.4. In this instrument setup, the locations of the pressure sensors are named Location L1b, L2b and L3b. During the January setup, the locations of the pressure sensors have been placed higher up on the beach relative to the deployment from November until December.

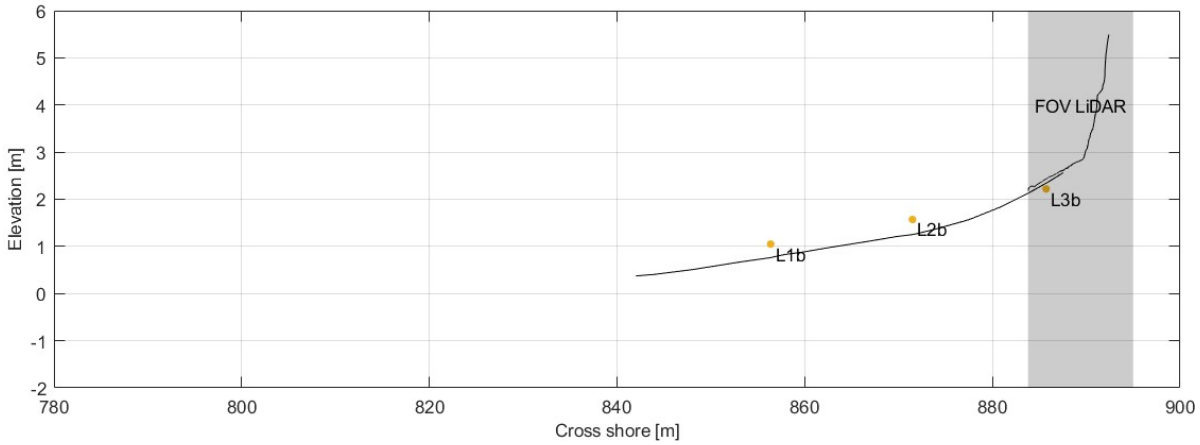

Figure 2.5: The transect with instrument locations during the single deployment in January. A local coordinate system is used in this chart. L1b, L2b and L3b indicate the locations of the pressure sensors. The filled gray area indicates the FOV (Field OF View) of the LLC LiDAR. There are two black lines in this plot. The line left of the FOV of the LLC LiDAR is the beach profile measured on the 5th of January before the high water event. The black line inside the LLC LiDAR FOV is the beach profile measured at 17:00 by the LLC LiDAR.

2.2. Event selection

Certain events from the fieldwork experiment have been chosen to be fully processed and analysed further. An event is defined as the duration of a single high water tide. A selection of 4 different events have been evaluated during this research. Swash conditions have been present during three of these conditions and collision conditions have been present during one of them. The difference in these events will show the changing characteristics during the different swash events, and an evaluation will be made upon the changing processes between the swash and collision conditions. These events have been separated into segments of 25-30 minutes. This allows an assumption of constant tidal and wave conditions during the duration of the segments.

The selection of the events is based on the dominant wave direction, image quality, the beach state and certain event characteristics. The preferred wave direction is a direction normal to the orientation of the dune system, since the runup camera, lidar and empirical runup formula operate in a one dimensional plane. This would mean the preferred wave heading is $292[^{\circ}]$. Image quality should have been such that the swash front can be properly tracked using the processing methods defined in Section **??**. Reduced clarity in the images can result in an improper identification of the waterline. The beach state should be in a concave upward profile (no runnels or other sudden elevation changes present), since changes in the profile could have an effect on the runup characteristics. Similar beach profiles during the events will simplify the comparison of the events.

Swash events with conditions closest to ideal have been found during the high water events on November 30th, December 1st and December 2nd. The high water event of January 5th has been evaluated for the collision conditions. Looking at Figure 2.6, the offshore wave orientation is relatively normal to the beach orientation, except for the event on December 2nd, which corrected for in Section **??**. Image quality during these events is sufficient, and beach profiles have a concave upward shape (see figure 2.37).

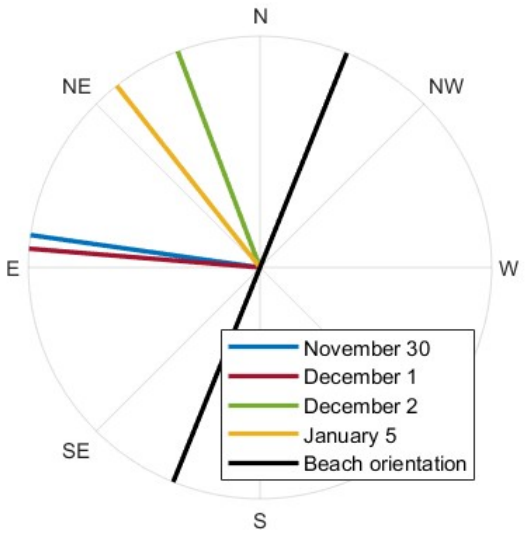

Figure 2.6: The dominant offshore wave angle of the incoming waves during the three events.

2.3. Offshore hydrodynamics

During the exctent of the Fieldwork Experiment, offshore wave and wind parameters have been gathered at the offshore stations. There were three offshore stations which measure the offshore tide wind setup and wave conditions. These are the ”Hoek van Holland”, ”Scheveningen” and the ”Europlatform” (see Figure 2.7). The offshore parameters of November 30th December 1st, December 2nd and January 5th.

Figure 2.7: The location of the Sand Engine is in between the two tidal stations and the location of the offshore wave station is located offshore at a depth of 32m.

At the locations ”Hoek van Holland” and ”Scheveningen”, tide (μ_{tide}) and wind setup (μ_{wave}) levels have been measured. The offshore significant wave height (H_0), offshore peak wave period (T_0) and incoming wave angle (α_0) have been measured at the ”Europlatform” at a depth of $32m$. The tidal wave heights and wind setup values of the events have been summarized in Figure 2.8. The sum of the tidal and wind driven setup levels is named $\mu_{offshore}$.

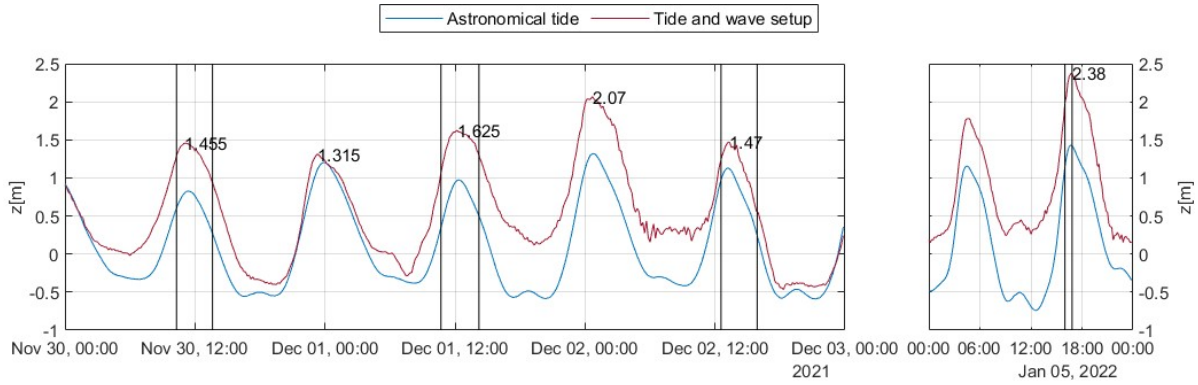

Figure 2.8: Tidal (μ_{tide}) and wind setup (μ_{wind}) data from November 30th to December 2nd and January 5th is measured by averaging between the measuring locations Hoek van Holland and Scheveningen. $\mu_{offshore}$ is indicated with the red line. The vertical lines indicate the time span of each event.

The offshore significant wave height (H_0), offshore peak wave period (T_0) and incoming wave angle (α_0) have been measured at the Europlatform at a depth of $32m$. The wavelength has been calculated according to the dispersion relation from the offshore wave period and wave length. The wave parameters of November 30th December 1st, December 2nd and January 5th have been plotted in Figure 2.9. Average wave characteristics during all segments of the events are also summarized in Table 2.1.

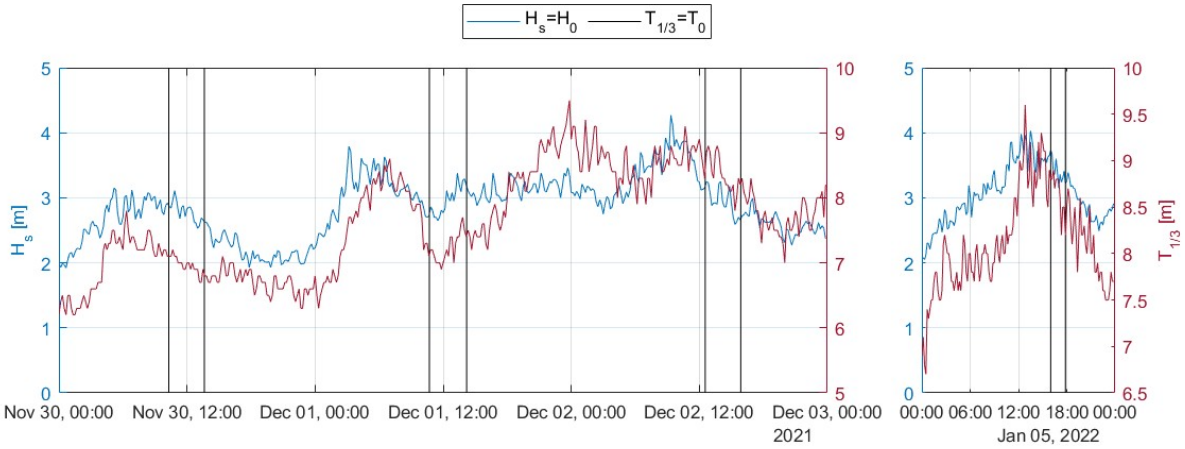

Figure 2.9: Significant wave heigth (H_s) and significant wave period ($H_{1/3}$) are measured from November 30th to December 2nd and January 5th at the Europlatform. Again the vertical lines indicate the time span of each event.

When relating the offshore conditions to nearshore conditions at the waterline, wave refraction could be influential. Waves conditions with larger incoming wave angle normal to the shore are expected to have reduced runup heights compared to the same wave conditions with smaller incoming wave angle. The influence of refraction is estimated using Equation 2.2. While using the offshore wave angle (α_0), and assuming that the wave angle at the waterline is $\alpha_h = 0°$ (Goda, 2000). Refraction factors (K_R) have been calculated at each time segment during the events using the offshore wave angels and wavelengths. Using the refraction factor, an estimate of the effective significant offshore wave height ($H_{0,eff}$) has been calculated, which will be referred to as the effective (offshore) wave height.

$$K_R = \sqrt{\frac{cos(\alpha_h)}{cos(\alpha_0)}} \tag{2.2}$$

Offshore parameters during the events of November 30th December 1st, December 2nd and January 5th have been averaged in segments of 20 to 30 minutes. These segments have been created according to the processing steps of the runup camera and LLC LiDAR (see Sections 2.4.2 and 2.4.3). From the offshore wave data is becomes apparent that during the swash events, the wave height did not differ much between the events, but the wave periods did change significantly. The highest wave height was recorded during the event on December 2nd and the lowest wave height during November 30th.

Segment $[hh:mm]$	$\mu_{offshore}[m]$	$L_0[m]$	$\alpha_0[^\circ]$	K_R	$H_0[m]$	$H_{0,eff}[m]$
November 30						
10:18 - 10:51	1.38	79	12.5	0.99	2.95	2.91
10:51 - 11:24	1.45	77	13.3	0.99	2.83	2.79
11:24 - 11:57	1.42	75	12.3	0.99	2.81	2.78
11:57 - 12:31	1.33	76	14.0	0.99	2.83	2.79
12:31 - 13:04	1.20	74	16.3	0.98	2.59	2.54
13:04 - 13:37	1.05	71	15.7	0.98	2.64	2.59
December 1						
10:42 - 11:14	1.27	80	37.0	0.89	2.79	2.49
11:26 - 11:59	1.57	76	27.3	0.94	2.72	2.56
11:59 - 12:32	1.61	79	19.8	0.97	2.93	2.84
12:32 - 13:06	1.58	82	11.7	0.99	2.99	2.96
13:06 - 13:39	1.53	85	5.3	1.00	3.23	3.22
13:39 - 14:12	1.40	89	2.5	1.00	3.21	3.21
December 2						
12:33 - 13:06	1.36	119	41.0	0.87	3.19	2.42
13:06 - 13:40	1.46	112	41.3	0.87	2.91	2.36
13:40 - 14:13	1.38	114	48.3	0.81	3.08	2.39
14:13 - 14:46	1.16	106	46.3	0.83	2.91	2.49
14:46 - 15:20	0.99	103	50.0	0.80	2.94	2.59
15:20 - 15:52	0.71	102	53.8	0.77	2.65	2.47
January 5						
16:00 - 16:25	2.10	122	29.0	0.93	3.60	3.35
16:25 - 16:50	2.36	120	30.0	0.94	3.45	3.24
17:00 - 17:25	2.28	114	29.3	0.93	3.25	3.03
17:25 - 17:50	2.12	110	28.0	0.94	3.31	3.11

Table 2.1: Offshore wave and tidal conditions during the events measured at the offshore stations. Wavelength L_0 is calculated using the dispersion relation for deep water. The effective offshore wave heights ($H_{0,eff}$) are calculated with the refraction coefficient using the offshore wave angle relative to beach orientation (α_0), and an assumption of the incoming wave angle at the waterline of $\alpha_h = 0$.

From the offshore wave data is becomes apparent that during the swash events, the wave height did not change much between the events, but the wave periods did change significantly. The highest wave height was recorded during the event on December 2nd and the lowest wave height during November 30th.

2.4. Nearshore hydrodynamic conditions

During the experiment, three different types of instruments have been used to measure nearshore hydrodynamics and beach and dune morphology, namely: pressure sensors, a runup camera and a LLC LiDAR (Line scanning Low Cost Light Detection And Ranging). The positioning, technical specifications and processing steps of each of the nearshore instruments will be elaborated upon in this section.

2.4.1. Nearshore wave field

The pressure sensors have been used to capture the incoming wave field at three nearshore locations of the Fieldwork Site. The pressure sensor used from the Fieldwork Experiment were RBR (Richard Brancker Research) pressure sensors (see Figure 2.10). The RBR pressure sensors measured the total pressure at the sensor at a sampling frequency of $8Hz$ (this includes both water pressure and air pressure). The total pressure signal can be converted to water level elevation ($z(t)$) by means of the processing steps presented in this Section.

Figure 2.10: RBR pressure sensor used during the Fieldwork Experiment.

Pressure sensor location
The pressure sensors were spaced in cross-shore direction in order to capture the wave dissipation in the IG band and the INC bands over the transect. The location in E and N of the pressure sensor was measured at the start of the Fieldwork Experiment using an RTK-GPS. The elevation of the pressure sensors (z_{rbr}) has been determined by measuring the distance between the sensor and the bed elevation (Δh_{rbr}) each day during the Fieldwork Experiment. The location of the sensor (z_{rbr}) is at the underside of the pressure sensor. Since the bed elevation (z_{bed}) has been measured using an RTK-GPS (see Section 2.5), the elevation of the pressure sensor could be determined. Figure 2.11 shows the derivation of the pressure sensor height during swash conditions.

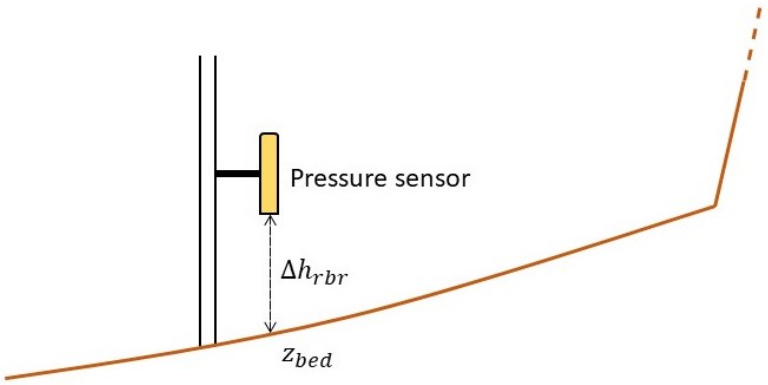

Figure 2.11: Derivation of an RBR pressure sensor height during the swash conditions. The yellow tube shows the RBR like it was attached to a pole during the Fieldwork Experiment. The brown line shows an abstract representation of the beach slope.

During the January 5th deployment, the top side of the pressure sensor has been measured using the RTK-GPS. This is done before and after the January 5th deployment. The height has not been altered during the deployment, thus the height of the sensor before and after the deployment should be the same. The location of the sensor lies around $20cm$ below the top of the RBR pressure sensor. In other words, the pressure sensor has a length of $20cm$.

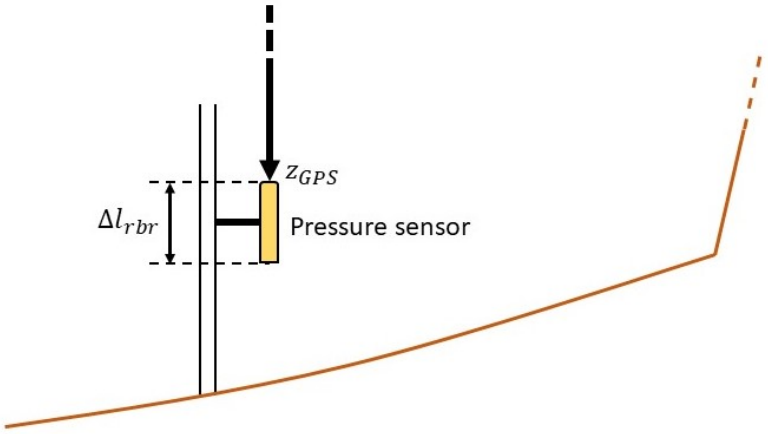

Figure 2.12: Derivation of an RBR pressure sensor height during the collision conditions.The yellow tube shows the RBR like it was attached to a pole during the Fieldwork Experiment. The brown line shows an abstract representation of the beach slope.

Segmentation pressure sensor data

A selection of pressure sensor data has been extracted from the full pressure sensor data set. This selection has been determined by the segments of the data of the runup camera and the LLC LiDAR. The segments of the runup camera and the LLC LiDAR have been defined in Sections 2.4.2 and 2.4.3 respectively, resulting in the same segments of pressure sensor data. Any segment duration (D) during swash and collision conditions is the same as the segments for the pressure sensor data. This has resulted in a segment duration of $D = 33$ minutes during swash conditions and $D = 25$ minutes during collision conditions.

Processing steps of the pressure sensor

Raw data from the pressure sensors has been processed according the the steps taken in the flow chart in Figure 2.13. The steps in the flow chart will be elaborated upon further in this section.

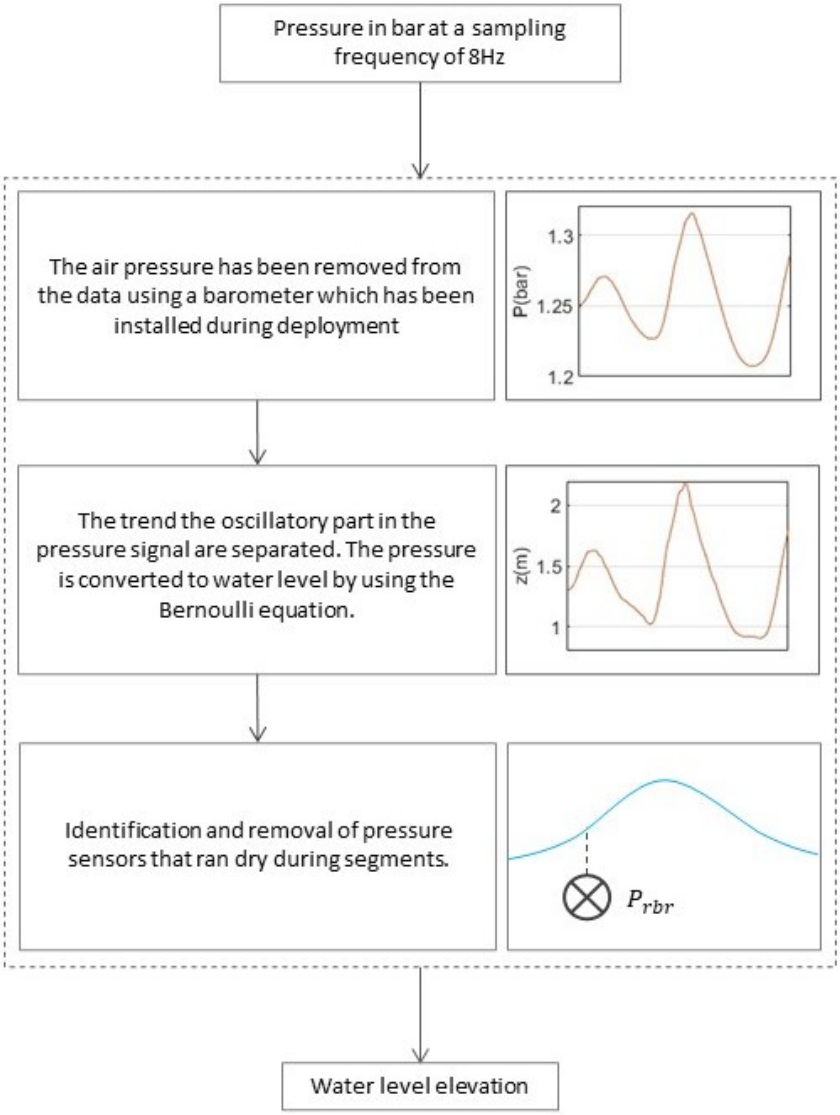

Figure 2.13: Data processing flow chart of the pressure sensor data. On the left side an explanation is given of each step. On the right side a snapshot of the processed data is showcased to give a better understanding of the data. The final result gives the water level elevation relative to the location of the pressure sensor.

Air pressure correction

The total pressure (P_{RBR}) includes both water pressure (P_{water}) and air pressure (P_{air}), however the main interest lies in the water pressure signal. For this reason, a barometer has been used in conjunction with the waterborne pressure sensors. Using the barometer, the air pressure during each segment has been determined. Then, the air pressure was subtracted from the total pressure signal. The results gives the water pressure signal.

$$P_{water} = P_{RBR} - P_{air} \tag{2.3}$$

Pressure to water level above pressure sensor

The corrected pressure signal from the pressure sensors was transformed to surface elevation using linear wave theory. This method uses the Bernoulli equation, and separates wave induced pressure and mean water level pressure. The complete equation is shown in Equation 2.4.

$$P = -\rho g z_w + \rho g a \frac{cosh(k(d + z_w))}{cosh(kd)} \tag{2.4}$$

In which P is the total water pressure, $\rho = 1025kg/m^3$ is the water density, $g = 9.81m^2/s$ is the gravity constant, a is the wave amplitude, z_w is the water level relative to the mean water level, k is the wave number and d is the depth relative to the trend of z_w ($z_{w,trend}$). Before deriving the Equation 2.4, the pressure data has been detrended, and a Fourier transformation was performed on the data set. This does two things. Firstly, the trend of the pressure data set was subtracted which results in $d = z_{w,trend} = 0$, and reduces equation 2.4 to equation 2.5.

$$P_{wave} = \rho g a \frac{cosh(k(d + z_w))}{cosh(kd)} \tag{2.5}$$

And secondly, the wave amplitudes could be estimated by looking at the individual harmonics of the Fourier transformation. The wavenumber k, which is the last unknown, was calculated using Guo's equation (Guo, 2002), which is a simple yet accurate estimation of the dispersion relation.

$$\sigma = \frac{2\pi}{T} \tag{2.6}$$

$$X = d\sigma\sqrt{gd} \tag{2.7}$$

$$y = X^2(1 - \exp(-X^\beta))^{(\frac{-1}{\beta})} \tag{2.8}$$

$$k = \frac{y}{h} \tag{2.9}$$

In which $\beta = 2.4908$ is a constant and T is the wave period. After solving equation 2.5 for the wave amplitude (a), only three steps remain in the transformation of the pressure signal to water level series. Firstly, the wave components resulting from equation 2.5 have been inverted to a time series using an inverse Fourier transformation, creating $a(t)$. Secondly, the trend of the pressure data was transformed into a water level using the first part of equation 2.4, $P_{trend} = -\rho g z$, and solving for water level (z). Thirdly, a complete water level time series has been created by adding water level trend to the wave amplitude time series and the instrument height, $z(t) = z_{w,trend} + a(t) + z_{rbr}$, in which $h(t)$ is the water level time series. Examples of the results from the pressure sensor processing can be found in Figure 2.16. A comparison is drawn between the offshore (location 1) and the nearshore locations (locations 7 and 8).

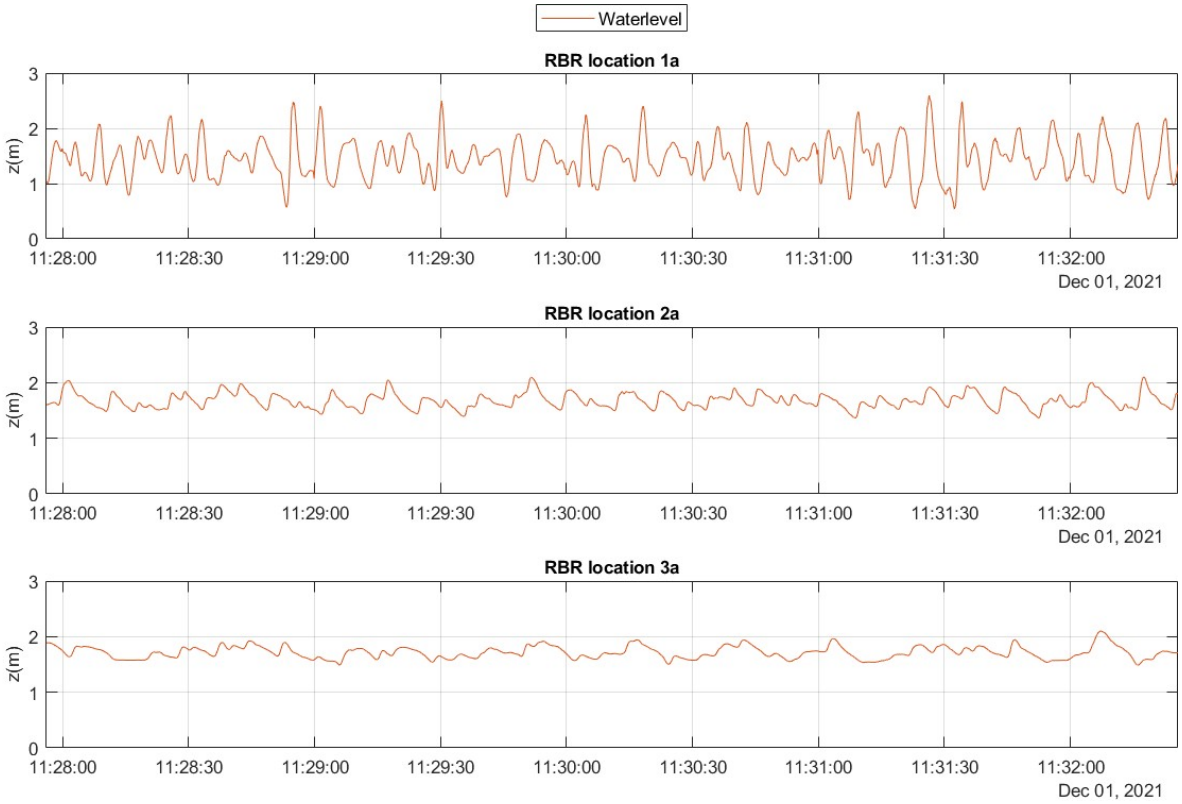

Figure 2.14: While focusing on a section of the water level height from each of the pressure sensors, several changes are found between the offshore and more onshore locations. Firstly, the wave height has significantly decreased. Secondly, At location 1, wave groupiness is still visible at location 1, while at the nearshore locations (7 and 8) this groupiness visibly is absent. Thirdly, the amount of waves measured at the offshore locations was more than at the nearshore locations. And lastly, the the wave skewness increases while the waves were moving nearshore.

.

Removal of segments

Pressure sensors which incidentally ran dry during segments have been removed before analyzing the data from the pressure sensors further. This is to prevent working with incomplete water level records, which can alter the outcome of the research without any physical basis. During the swash events, the cross shore location of the waterline has been tracked by the runup camera (see Section 2.4.2). In order to determine whether a pressure sensor was located above water at any instances during a segment, a distribution is created from the cross shore location of the runup camera. If the cross shore location of the pressure sensor is above 1% in the distribution of the cross shore location of the waterline, the segment of the pressure sensor has been removed. The probability of the pressure senor running dry is P_{rbr}, with subscript ”rbr” indicating the pressure sensor location L2a or L3a. Location L1a has not been investigated, since this pressure sensor was located much further offshore, and would never had the possibility of running dry during a high water event.

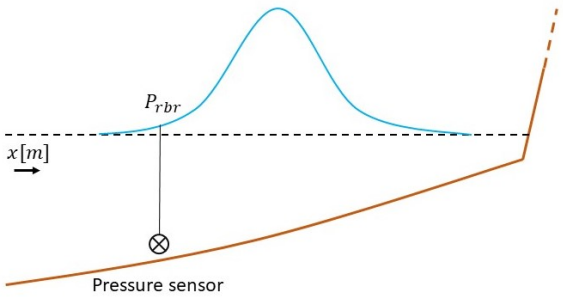

Figure 2.15: Abstract example of the distribution of waterline (in blue) and the location of the pressure sensor and the percentage the pressure sensor is above water (P_{rbr}). The brown line represents the beach and dune and the blue line an example of the distribution of the swash.

.

The pressure sensor segments have been removed according to the method above. The probability of the pressure senor running dry is P_{rbr}, with subscript "rbr" indicating the pressure sensor location L2a or L3a. Location L1a has not been investigated, since this pressure sensor was located much further offshore, and would never run dry during any high water event. The probability of the pressure sensors running dry is summarized in Table 2.2 This means the records from pressure sensor at location L3a will not be used at all since this pressure sensor is above water the entire duration of each event. Certain segments of pressure sensor L2a have also been omitted from the dataset.

Segment	$P_{L2a}[\%]$	$P_{L3a}[\%]$
November 30		
10:18 - 10:51	0.70	17.3
10:51 - 11:24	0.13	11.7
11:24 - 11:57	0.16	11.2
11:57 - 12:31	1.69	22.5
12:31 - 13:04	6.23	45.0
13:04 - 13:37	27.4	78.5
November 30		
10:42 - 11:14	3.63	27.1
11:26 - 11:59	0	1.70
11:59 - 12:32	0	1.00
12:32 - 13:06	0	1.25
13:06 - 13:39	0.01	2.8
13:39 - 14:12	0	6.07
November 30		
12:33 - 13:06	0	6.03
13:06 - 13:40	0	3.24
13:40 - 14:13	0	4.75
14:13 - 14:46	0.56	14.1
14:46 - 15:20	12.7	66.7
15:20 - 15:52	33.3	84.9

Table 2.2: Probability of presssure sensors running dry during all swash events.

During the January event, the pressure sensors at locations L2b and L3b were constantly located above water. This could visually be identified in the data, and the data of these pressure sensors has been remover. However, the pressure sensor at L3b has been used in the comparison of between the pressure sensor elevation and the elevation profile of the LLC LiDAR. A different processing procedure has been used for the pressure sensor located in the swash zone, which has been described in the text below.

Pressure sensor in swash zone

The January data of the pressure sensor at location L3b has been processed hydrostatically via Equation 2.10. Reason being the uncertainties in the physics of the pressure to water level conversion of the sensor located in the swash zone. Additionally, the pressure sensor at L3b was buried during the January event by about 10 to 20 cm (see Section 2.5), which increases the uncertainties for the conversion. Barometric pressure was removed in the same manner as for pressure sensors located constantly under water via Equation 2.3.

$$P = -\rho g z \tag{2.10}$$

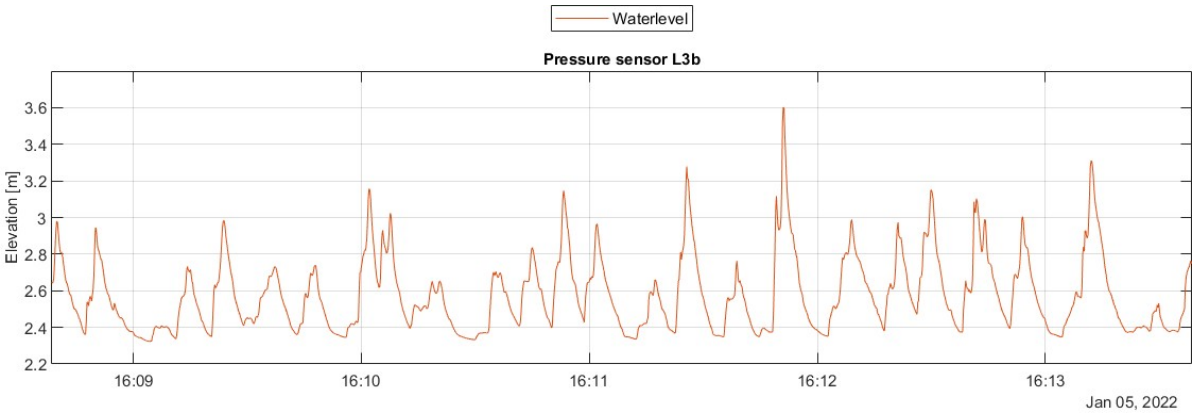

Figure 2.16: The water level elevation at location 3b show high and sharp peaks and flat troughs. This indicates that the pressure sensor continuously ran dry during run down.

.

2.4.2. Runup during swash conditions

During swash conditions, a runup camera has been used to monitor the upper shoreface and the beach in order to track the waterline elevation ($h(t)$) during the Fieldwork Experiment. The camera used during the Fieldwork Experiment is a GOPRO Hero 5 camera, which was setup to take pictures at 4k quality. The runup camera is not used to measure runup on the duneface. This is because of difficulties with image rectification at the suddenly steep surfaces of the dune. The difficulties are caused due to slumping of the duneface. When waves reach the duneface, slumping occurs which causes large changes in bathymetry and subsequently causes incorrect rectification of the images.

Figure 2.17: View of the runup camera towards the transect.

The runup camera was directed towards the transect and measures the location of the waterline on the transect (see Figure 2.17). The FOV (Field Of View) is the extend to which the beach is visible to the instrument, which is from the most offshore location to the most nearshore location visible for the runup camera. The hydrodynamic variability within this transect is where the main focus of this study lies.

The sampling frequency of the runup camera has been chosen by looking at two criteria, the wave frequency and the storage capacity of the camera. When defining the first criteria, the sampling frequency needed to be an order lower than the wave period to ensure the peaks of the swash excursions are properly tracked. The second criteria, which depends of the storage capacity of the camera, was determined by the duration of a high water event. A minimum filming duration of 6 hours is set to ensure enough time is available to measure the entire high water event. For these reasons, pictures have been taken at a frequency of $1.5Hz$.

Runup camera location and FOV
The location of the camera has been determined by three different criteria: the image accuracy, the desired measuring location and the mounting capabilities. Firstly, when the footprint of the pixel becomes to large, the swash tracking capabilities of the camera diminish. Secondly, the desired section to be measured of the event was the upper beach section, since high water events are investigated. Thirdly, the camera could have interference with waves if the camera is placed too close to the bed, thus the camera needed to be positioned as high as possible. Taking into account these criteria, the following location relative to the cross shore transect was chosen. The location of the camera was about $35m$ from the transect, at a height of $2.5m$ relative to the bed. This ensured the footprint of the camera is accurate enough to detect the swash motions.

Due to the significant height, the camera was placed on a tri-pole frame to in order to provide enough support and prevent vibration of the frame due to waves. At this location from the transect, the pixel footprint is around $0.025-0.04m^2$ which is sufficiently accurate for tracking the waterline location ($h(t)$). The cross shore transect in Figure 2.20a 2.18, was the transect where the swash motions have been measured by the run-up camera. The tri-pole frame design can be viewed in Figure 2.18.

Figure 2.18: View of the frame on the beach. The picture is taken form the location of the cross shore transect

.

Segmentation of runup camera data
The images of the runup camera have been separated into segments of 33 minutes. Each of these segments has been processed individually trough the steps following this step. The duration of the segments are summarized in Table 2.3. There are 6 segments during each of the events, resulting in a total duration of 5 hours and 34 minutes for each event.

November 30	December 1	December 2
10:18 - 10:51	10:42 - 11:14	12:33 - 13:06
10:51 - 11:24	11:26 - 11:59	13:06 - 13:40
11:24 - 11:57	11:59 - 12:32	13:40 - 14:13
11:57 - 12:31	12:32 - 13:06	14:13 - 14:46
12:31 - 13:04	13:06 - 13:39	14:46 - 15:20
13:04 - 13:37	13:39 - 14:12	15:20 - 15:52

Table 2.3: Segments of the runup camera during the swash condition events

Processing steps of the runup camera
Images gathered by the runup camera during the events have been run trough several steps before finally arriving at the waterline variations in time ($h(t)$). These steps have been summarized in a flow chart (Figure 2.19).

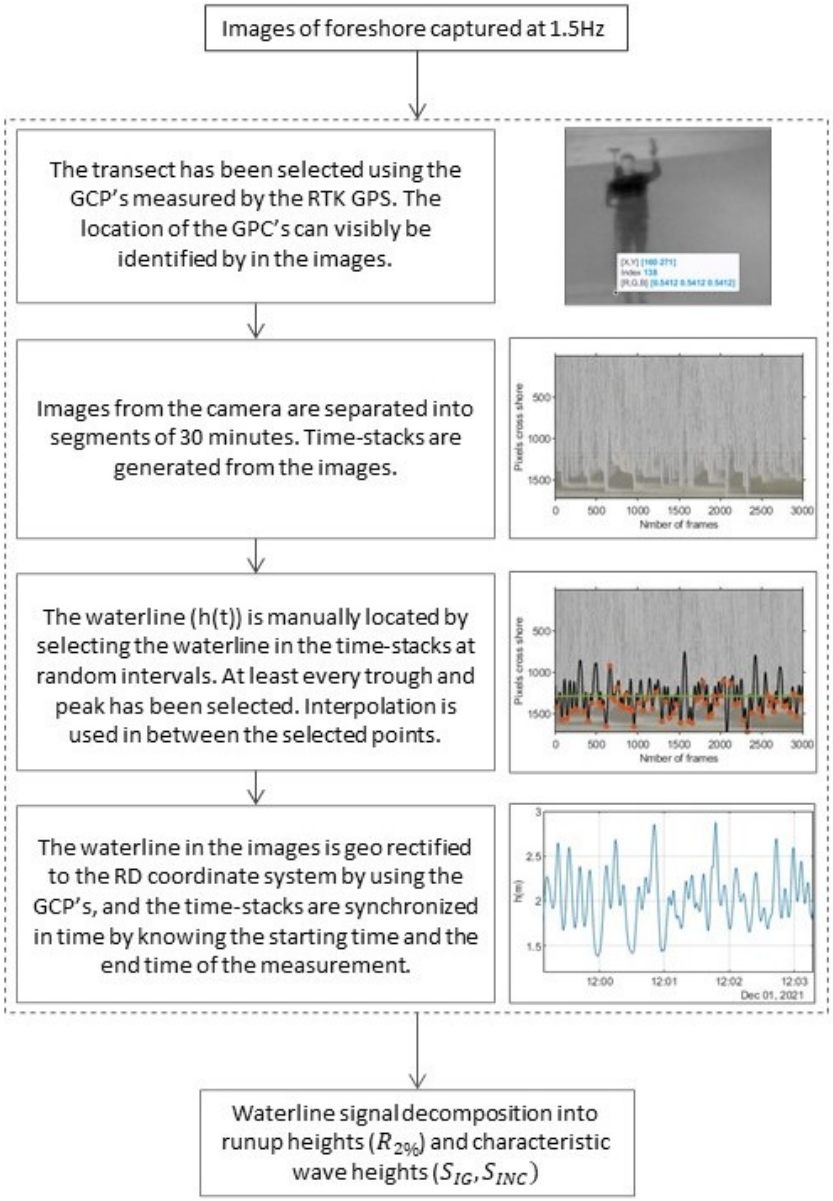

Figure 2.19: Processing steps of the runup camera are explained step-by-step in this flow chart. The processing steps are described in words on the left and there is a graphical representation of the steps on the right. The flow chart starts with the images gathered by the runup camera, where after steps are taken which finally result in the waterline elevation signal ($h(t)$). The processing steps are elaborated upon further in this Section (Section 2.4.2).

The summarized steps are elaborated upon the the paragraphs below. Specifics of each step are specified and figures will give a better visual understanding of each step taken.

Time stack generation
Time stacks are created from the images by stacking pixels along a transect in the images. The transect in the images has been located using the GPS location in the images. Whilst measuring the location of the transect with the GPS, the runup camera has also been taking pictures. In the pictures taken during the GPS measurement, the pixel location of each GPS point can be extracted. An example of

this method can be found in figure 2.20b. By identifying all GPS locations within the images, the transect of figure 2.20a can be drawn. During this event, the transect of the runup camera is from station 4 until the dune toe. Other events did not necessarily have the same transect length. This depends on the GCP's measured during each event.

(a) The location of the transect within an images taken by the runup camera.

(b) GPS location in the image.

Figure 2.20: In the left image, the red line is represents the transect which has been identified by the RTK-GPS location in the images at the start and at the end of an event. In the right Figure, an example is given of the identification of a GCP location in the image. The GCP is selected from the location of the RTK-GPS.

A time-stack is created from the images and the transect drawn in Figure 2.20a. This is done by stacking the transects of all images of a segment on top of each other. A segment of the time-stack can be seen in figure 2.21. Each pixel stack represents frames which have time steps of 1.5s in between.

Manual waterline extraction

Thirdly, the waterline is manually determined from the time-stack. The pixel locations of the runup maxima, minima and other defining features have been selected. Trough interpolation between the selected points, a line can be created. This is done using a spline-interpolation method, since this is more in agreement with the waterline compared to a simple linear interpolation. Figure 2.21 shows the waterline in the time-stack. The waterline has been carefully investigated after the interpolation has been performed, and any significant errors have been corrected for.

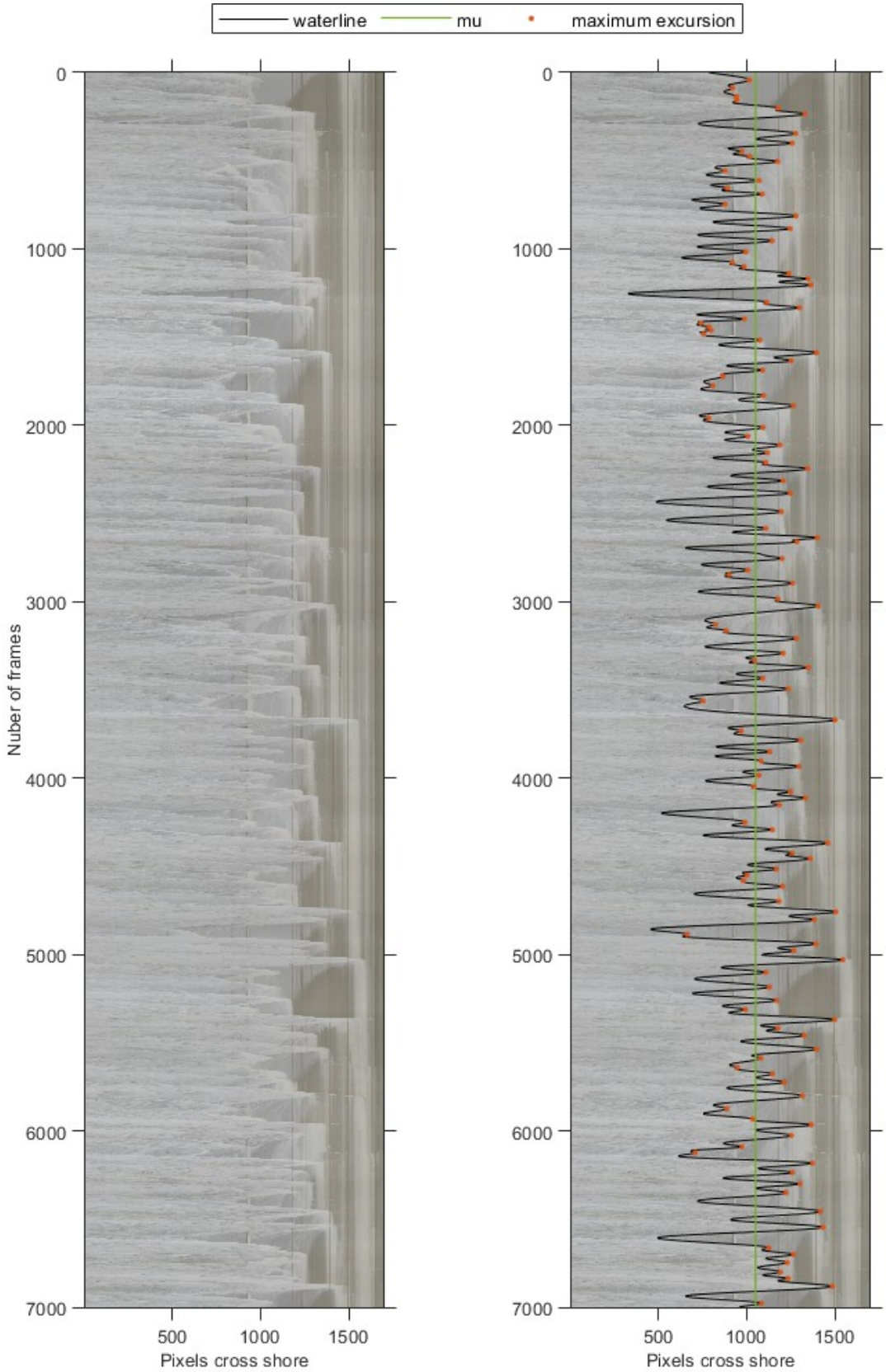

Figure 2.21: The figure on the left is a preview of the time stacks during the December second event generated by the data extraction process. The waterline from November 30th, as well as the runup maxima and the mean runup level can be seen in the figure on the right.

Geo referencing
Via linear interpolation between the GPS points and the manually extracted waterline in image coordinates, the waterline ($h(t)$) can be geo rectified. Geo rectification is the transformation of image coordinates to, in this case, the RD coordinate system. The location of the GCP's are known in both image coordinates and pixel coordinates. Via linear interpolation between the GCP locations, the waterline has been transformed to the RD-coordinate system. Where after the RD-coordinate system has been transformed to the local cross-shore coordinate system.

Time synchronization
Time synchronization has been done by using an external clock and the internal clock of the GOPRO Hero 5. The starting time and end time of the measurement have been identified using the external clock. The external clock uses time corrected by an atomic clock. The time at the start of the measurement are compared to the time at the end, and since the number of pictures taken is known, the capturing frequency can be calculated. The calculated time has been compared to the time from the GOPRO Hero 5 clock. The GOPRO Hero 5 clock is around 2 minutes off from the actual time, but the difference stayed constant during all measurements. For that reason it is concluded that the time synchronization is correct. The final result of the runup camera processing procedures gives the waterline location of the transect during the each of the selected events. A snapshot of the final result can be viewed in figure 2.22.

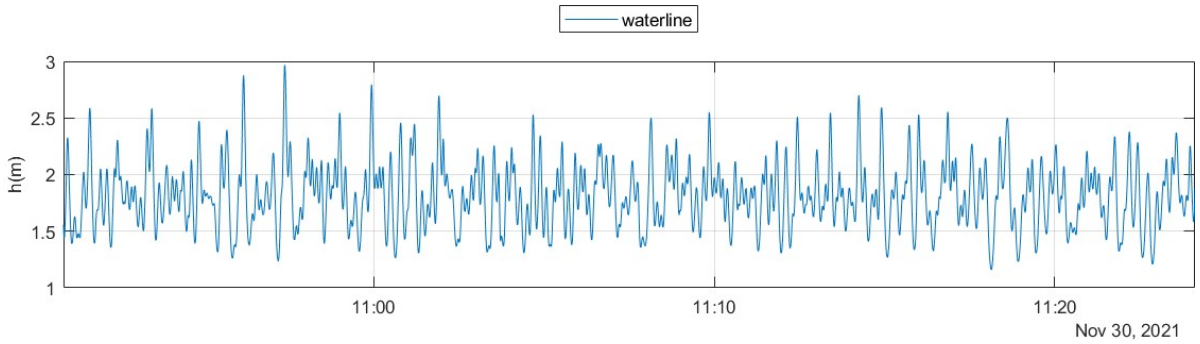

Figure 2.22: This is a time segment of the waterline at during the December 1st evetn. The final result of the processing steps gives the height of the waterline continuous in time.

Runup heights
The runup heights $R_{\%}$ have been calculated from the distribution of the maximum excursion heights during each segment. An example of the location of the maximum excursion can be found in the time stack of Figure 2.21, in which the green dots indicate the maximum excursion location. A (empirical) distribution is created from the maximum excursion elevations (see Figure 2.23). From the distribution, the $R_2\%$ can be calculated by finding at which elevation the maximum runup excursion is exceeded only two percent of the time. Additionally, a normal distribution has been fitted to the maximum excursion elevations, which follows the distribution of the empirical fit closely.

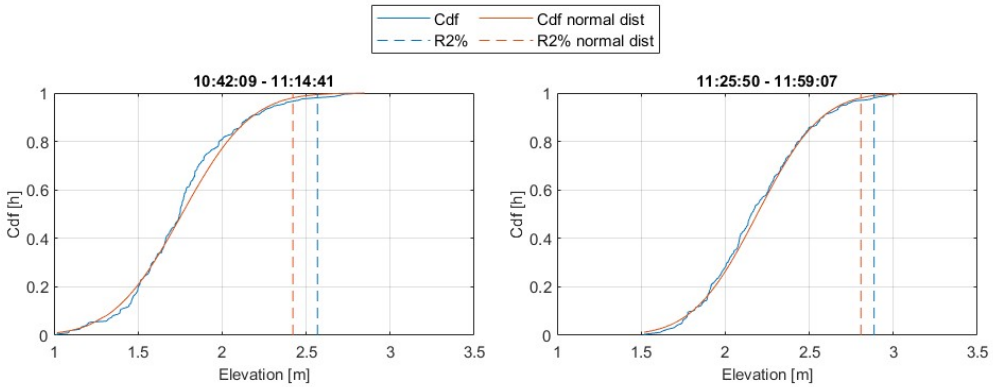

Figure 2.23: The distribution of runup during the swash conditions on December 1st, with the empirical distribution in red and a fitted normal distribution in blue. The vertical lines indicate the $R_2\%$ height relative to NAP, so $R_2\% + \mu_{wave} + \mu_{wind} + \mu_{tide}$.

2.4.3. Runup during collision conditions

In order to measure the runup elevations during collision conditions a LLC (Line-scanning Low Cost) LiDAR has been used. The LLC LiDAR measured the conditions of on the beach dune and hydrodynamics on a single line in cross-shore direction at a sampling rate of $6Hz$. The LLC LiDAR provides continuous measurements of both the water level elevations and the morphology changes.

Figure 2.24: Image of the LLC LiDAR during the Fieldwork Experiment. The LLC LiDAR is inside the silver box with the triangle shaped extension. This is a water tight cover to protect the instrument from wave impact. The other instrument, located on the bottom right of the image, has not been used in this MSc Thesis.

Measurements performed by LLC LiDAR has become increasingly popular as an alternative to other nearshore devices (Pinault et al., 2020). The LLC LiDAR is an accurate (mm) system, and contrary to the runup camera, the system can measure during all conditions during low visibility conditions and on steep slopes. This versatility has been useful in the fieldwork experiment, since this system provides a good solution to measurements during collision conditions. Another benefit of the LLC LiDAR is the non-intrusiveness of the instrument, which means the instrument itself has little to no impact on the nearshore conditions. These benefits are the reason the LLC LiDAR is used as the device of choice in order to measure runup during collision conditions.

LLC LiDAR location and FOV

The location of the LLC LiDAR is determined by the FOV and the range of the device. The FOV is about $110°$ and the range is around $8m$ for this specific LLC LiDAR. The LLC LiDAR has been directed towards the dune, since measuring hydrodynamic conditions at the duneface is a requirement during collision conditions. The device has been positioned around $6[m]$ from the duneface at a height of $2.7m$ from the beach, while having a pitch angle of $50°$. This will allow the LLC LiDAR to see the entire duneface and a section of the upper beach. However, due to the position and the limited range of the LLC LiDAR, the full rundown cannot be measured. The limited range is also the reason why the LLC LiDAR has not been used during swash conditions.

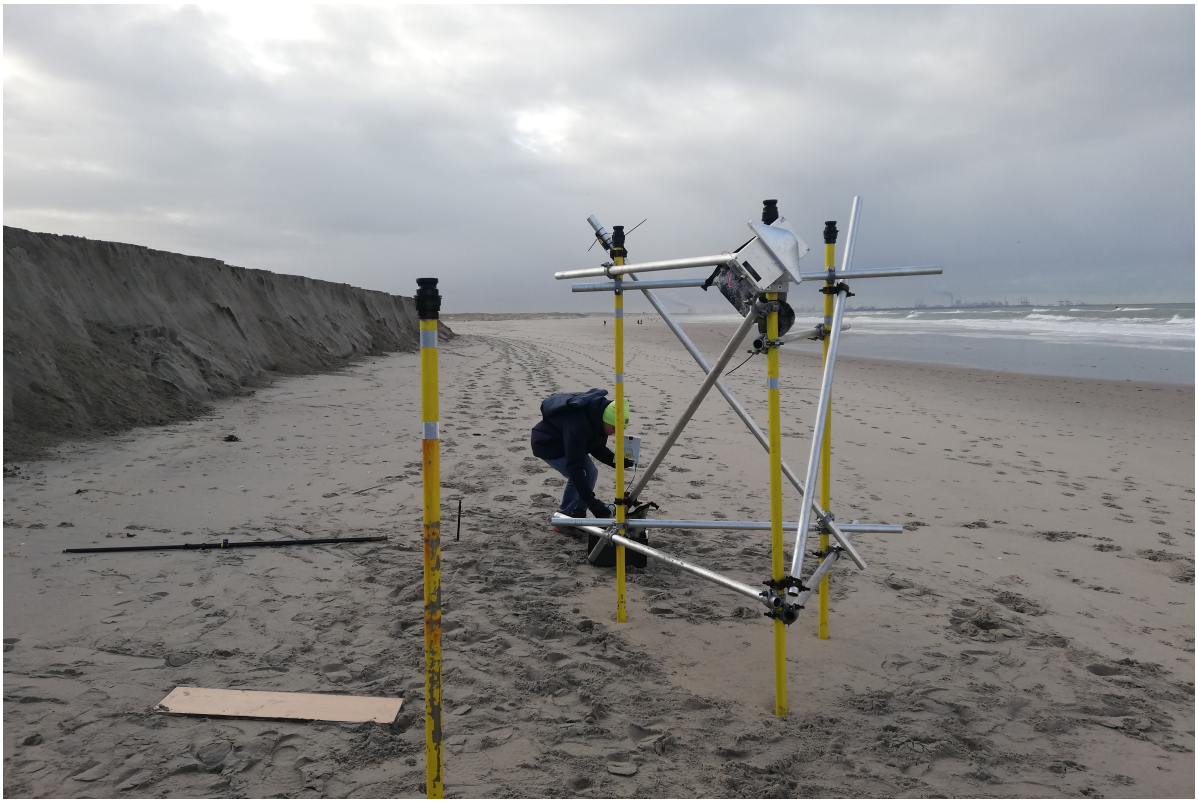

Figure 2.25: The location and orientation of the LLC LiDAR.

LLC LiDAR processing steps

The processing steps of the data from the Fieldwork Experiment will be described in this section. The original LLC LiDAR data consists of two variables, angles ($\theta(t)$) and distances ($l(t)$). In order to convert the data to real world coordinates, the following steps are taken (see Figure 2.26).

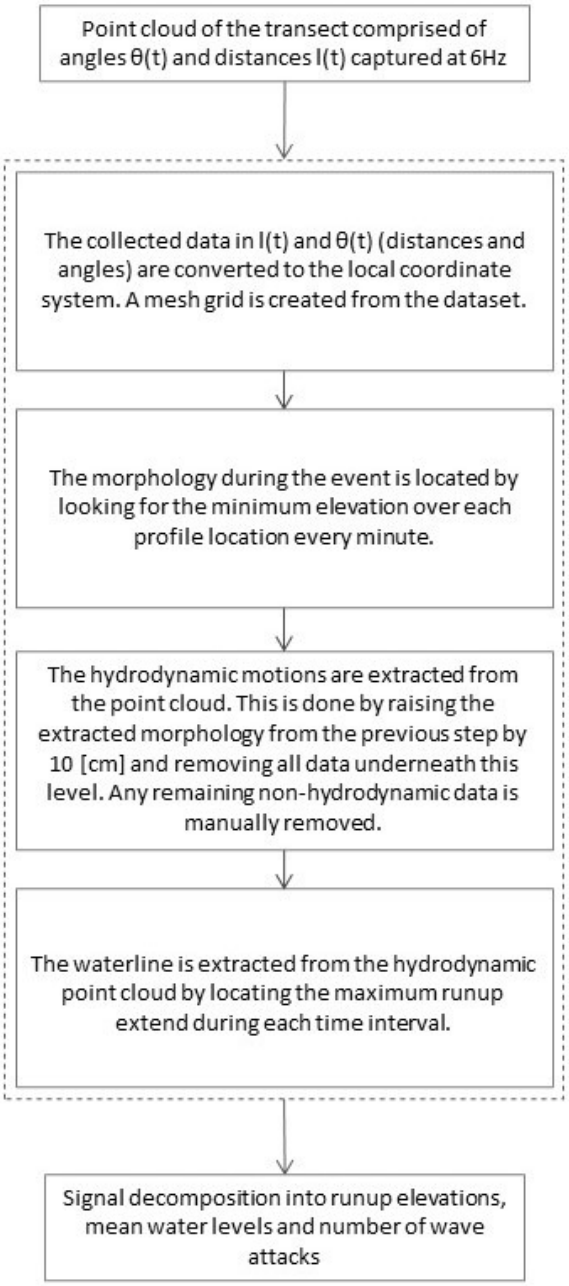

Figure 2.26: Data processing flow chart of the LLC LiDAR data. On the left side an explanation is given of each step. On the right side a snapshot of the processed data is showcased to give a better understanding of the data. The final result gives the locations of the waterline which can be used to extract the runup elevations from the data. Further explanation of teach step is given in the rest of the Section.

Segmentation of LLC LiDAR data

A selection of LLC LiDAR data has been used for the analysis of the collision conditions. The LLC LiDAR continuously measured the dune face and part of the upper beach during the Fieldwork Experiment. The selection of collision event data ranges from 16:00 until 17:50 on January 5th. During this time, a storm was present that induced the collision conditions. The tidal high water peak during the storm was at 16:50 (see Figure 2.8), which is why this time range was chosen. The collision conditions have been most severe around the high water peak. From the data ranging from 16:00 until 17:50, four segments of 25 minutes each are created. These segments range from 16:00 - 16:25; 16:25 - 16:50; 17:00 - 17:25; 17:25 - 17:50. A small section from 16:50 to 17:00 has not been measured due to the settings at which the LLC LiDAR has been operating during the Fieldwork Experiment. The LLC LiDAR

measured for 50 minutes which starts on the hour.

Translation and rotation of the point cloud
The raw data from the LLC LiDAR (in $l(t)$ and $\theta(t)$) has been converted to the local cross shore coordinate system via the three steps. Firstly, the raw data of the LLC LiDAR, which consist of distances ($l(t)$) and angles ($\theta(t)$), have been converted to a local coordinate system of the LLC LiDAR, which consists of $(x(t), y(t), z(t))$. The local coordinate system of the LLC LiDAR does not represent the real world coordinates, but this step is necessary to move on to apply the rotation matrices in the next steps. The center of the local coordinate system is the origin of the point cloud, which is the puck of the LLC LiDAR.

The second step involved positioning point cloud in the RD-coordinate system $(E(t), N(t), U(t))$. This has been achieved by determining the position and orientation of the LLC LiDAR with an RTK-GPS. The top corners of the LLC LiDAR have been measured before and after the collision event (see Figure 2.27).

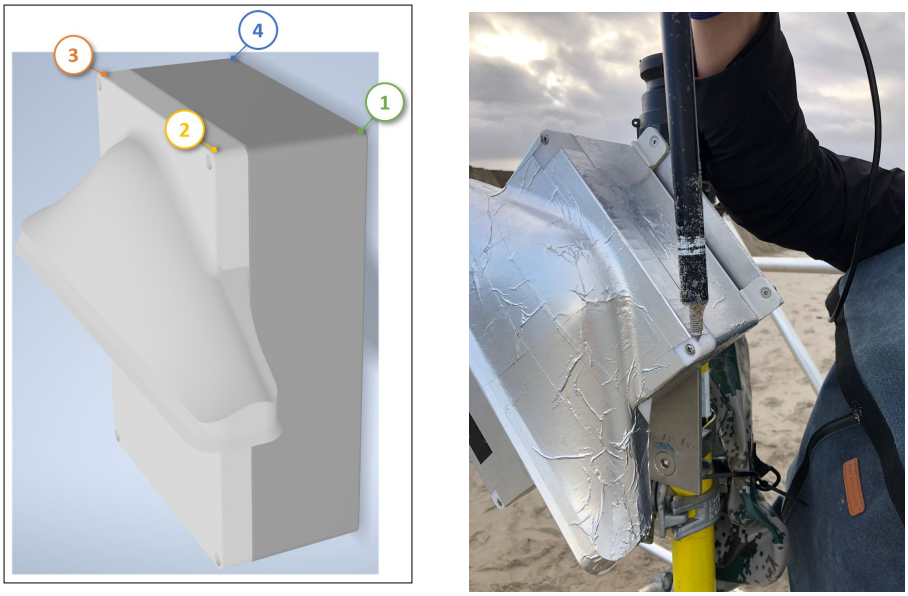

(a) Location of top LLC LiDAR corners

(b) Example of a corner measurement

Figure 2.27: The location of the corners of the LLC LiDAR relative to the points measured by the RTK-GPS in the local coordinate system of the LLC LiDAR. These points are used to determine the orientation and location of the LLC LiDAR box.

This gives four points in the RD-coordinate system which can be used to position the point cloud from the LLC LiDAR. The corners have been measured three times each. The average of each RTK-GPS corner points can the puck location can be found in Table 2.4.

Location	E [m]	N [m]	U [m]
Corner 1	72300.269	451904.819	4.343
Corner 2	72300.281	451904.892	4.340
Corner 3	72300.365	451904.850	4.475
Corner 4	72300.349	451904.777	4.475
Puck origin	72300.399	451904.878	4.366

Table 2.4: The corner coordinates of the LLC LiDAR during the January 5th event. The center is the mean of all the corner coordinates.

The rotation of the LLC LiDAR has been determined by finding the best fit between the four points measured by the RTK-GPS and the top corners of the LLC LiDAR. By subtracting the mean of the RTK-GPS coordinates (see Table 2.4) from the RTK-GPS coordinates, and lining up the RTK-GPS corner points with the corners of the LLC LiDAR box, the rotation parameters (Heading, Pitch Roll) can

be found. This resulted in the rotations, Heading: $287\,\mathrm{deg}$, Pitch $53\,\mathrm{deg}$ and Roll $-7\,\mathrm{deg}$. See Figure 2.29 for the corner match up.

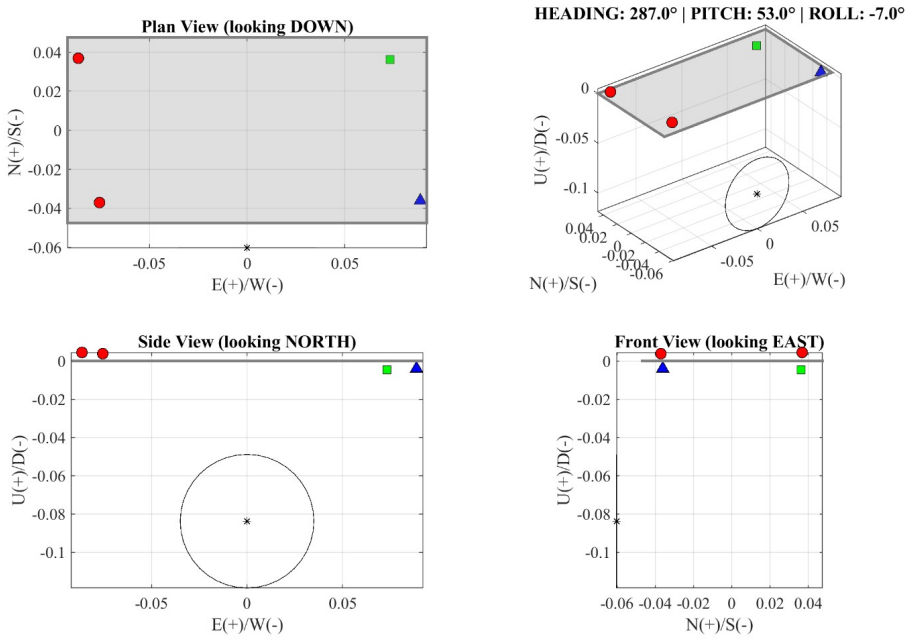

Figure 2.28: Each plot gives a different view of the comparison between the measured corners and the box orientation created by the best fit. The corner match up gives an orientation with a heading of $287°$, a pitch of $53°$ and a roll of $-7°$. The circle in the top-right and bottom-left plots indicate the puck of the LLC LiDAR. The puck is the origin of the LLC LiDAR point cloud.

In order to apply the rotation and translation to the point cloud in the local coordinate system of the LLC LiDAR, the origin of the point cloud relative to the corners has to be determined. The origin of the LLC LiDAR point cloud is the puck inside the casing of the instrument. The distance of the LLC LiDAR puck relative to the center of the top of the box are 0 mm in x-direction (in the center of the box), -60.3 mm in y-direction and -83.82 mm in z-direction (beneath the top of the box). With the origin of the point cloud known in local and RD-coordinates (see Table 2.4), and the rotation of the point cloud determined, the point cloud can be positioned correctly. The rotation is done by using the following rotation matrices:

$$R_x = \begin{pmatrix} 1 & 0 & 0 \\ 0 & cos(roll) & -sin(roll) \\ 0 & sin(roll) & cos(roll \end{pmatrix}$$

$$R_y = \begin{pmatrix} cos(pitch) & 0 & sin(pitch) \\ 0 & 1 & 0 \\ sin(pitch) & 0 & cos(pitch) \end{pmatrix}$$

$$R_z = \begin{pmatrix} cos(yaw) & -sin(yaw) & 0 \\ sin(yaw) & cos(yaw) & 0 \\ 0 & 0 & 1 \end{pmatrix}$$

In which R_x is the rotation matrix of roll which rotates around the x-axis of the local coordinate system, R_y is the rotation matrix of pitch which rotates around the y-axis and R_z is the rotation matrix of yaw which rotates around the z-axis. Yaw is the rotation in the direction of the Heading - $90\mathrm{deg}$. The rotation has been performed on the LLC LiDAR point cloud in the local coordinate system as demonstrated in Equation 2.11. The order of rotation is first roll, then pitch and lastly yaw. Translation values come from the RD-coordinates of the LLC LiDAR puck.

$$A_{RD} = R_x R_y R_z A_{local} + P_{origin} \tag{2.11}$$

In which:

$$A_{RD} = \begin{pmatrix} E_1(t) & N_1(t) & U_1(t) \\ \vdots & \vdots & \vdots \\ E_n(t) & N_n(t) & U_n(t) \end{pmatrix}$$

$$A_{local} = \begin{pmatrix} x_1(t) & y_1(t) & z_1(t) \\ \vdots & \vdots & \vdots \\ x_n(t) & y_n(t) & z_n(t) \end{pmatrix}$$

$$P_{origin} = \begin{pmatrix} E_{origin} & N_{origin} & U_{origin} \end{pmatrix}$$

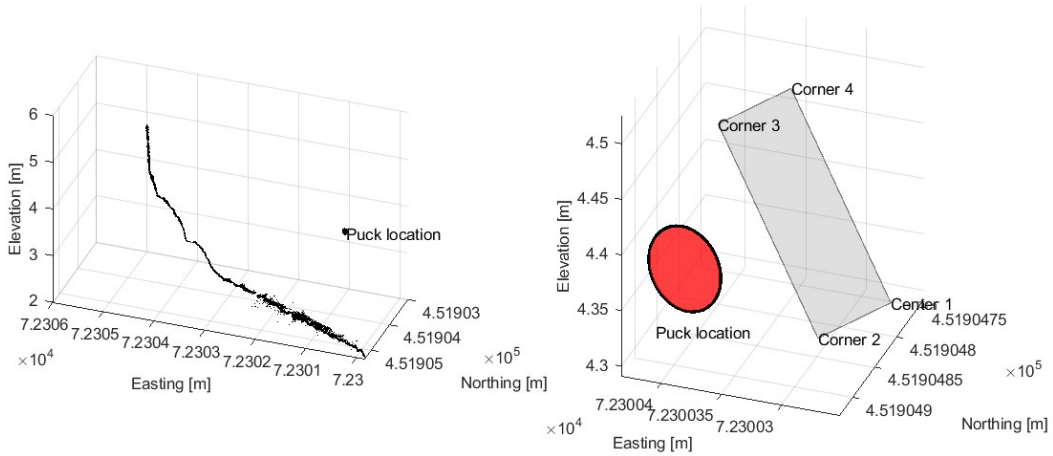

Figure 2.29: On the left, the rotated and translated point cloud in RD-coordinates of the first 45 seconds of the measurement. On the right, the orientation of the LLC LiDAR and LiDAR puck in RD-coordinates.

Thirdly, the RD-coordinates of the point cloud of the LLC LiDAR have been transformed to the local cross shore coordinate system. The conversion of Easting and Northing to the cross shore system has is done using Equation 2.12.

$$x = \sqrt{(E - E_{ref})^2 + (N - N_{ref})^2} \tag{2.12}$$

In which x is the cross shore location, E are the Eastings of the LLC LiDAR point cloud and N are the Northings of the LLC LiDAR point cloud. Since the orientation of the LLC LiDAR is not exactly cross shore, there might occur small errors from this conversion. But for the sake of this research, this is neglected. This assumption is made since the main interest lies in the height of data, and not the cross shore location. The LLC LiDAR also has a significant amount of roll ($7\,\mathrm{deg}$) during placement. This could also lead to errors in the conversion of the point cloud.

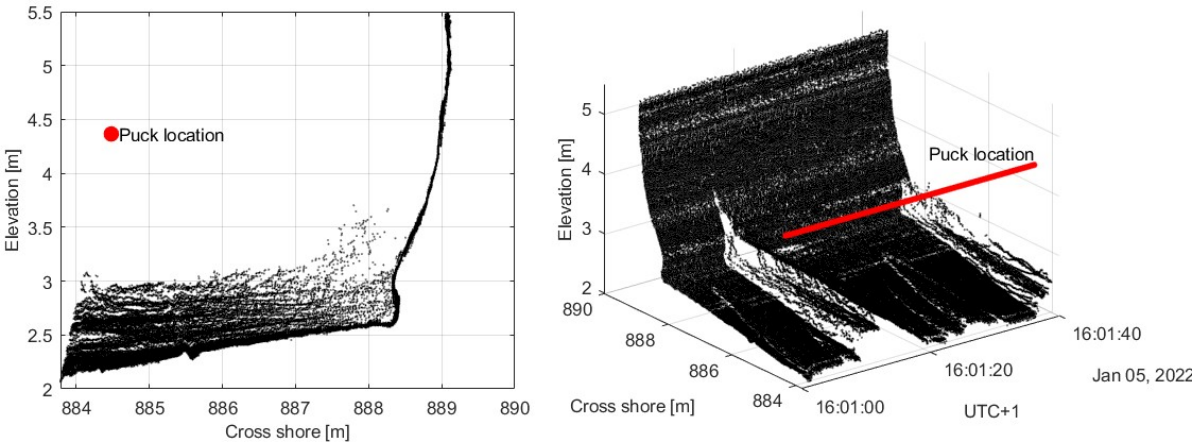

Figure 2.30: First 45 seconds of the LLC LiDAR segment from 16:00-16:25 in the local (cross shore) coordinate system. On the left the 2D version of the coordinate system, and on the right the cross shore changes in time.

LLC LiDAR point cloud grid

The randomly scattered point cloud has been has been structured by creating a grid with a fixed bin size. This conversion is made since the scattered point cloud is difficult to work with. The dimensions of a grid bin are $dt = 0.2s$ in time, and $dx = 15cm$ in cross shore direction. In order to ensure the enough points are within a grid bin, the number of pints within the grid bins have been checked. The average sample size of the bins in cross shore orientation has been plotted in Figure 2.31. It is interesting to see that the bin size directly under the LLC LiDAR is largest. The sample size at around the dune face ($889m$ to $891m$ cross shore) is changing significantly. This is due to the slumping during the time segment. Due to the dune retreat, the LLC LiDAR could measure further in crosshore direction, which created the spikes in the sample points in that region. Using the grid size with $dt = 0.2s$ and $dx = 15cm$, the average number of sample points is well above 2 in most bins. Any grid points without data are filled via linearly interpolation.

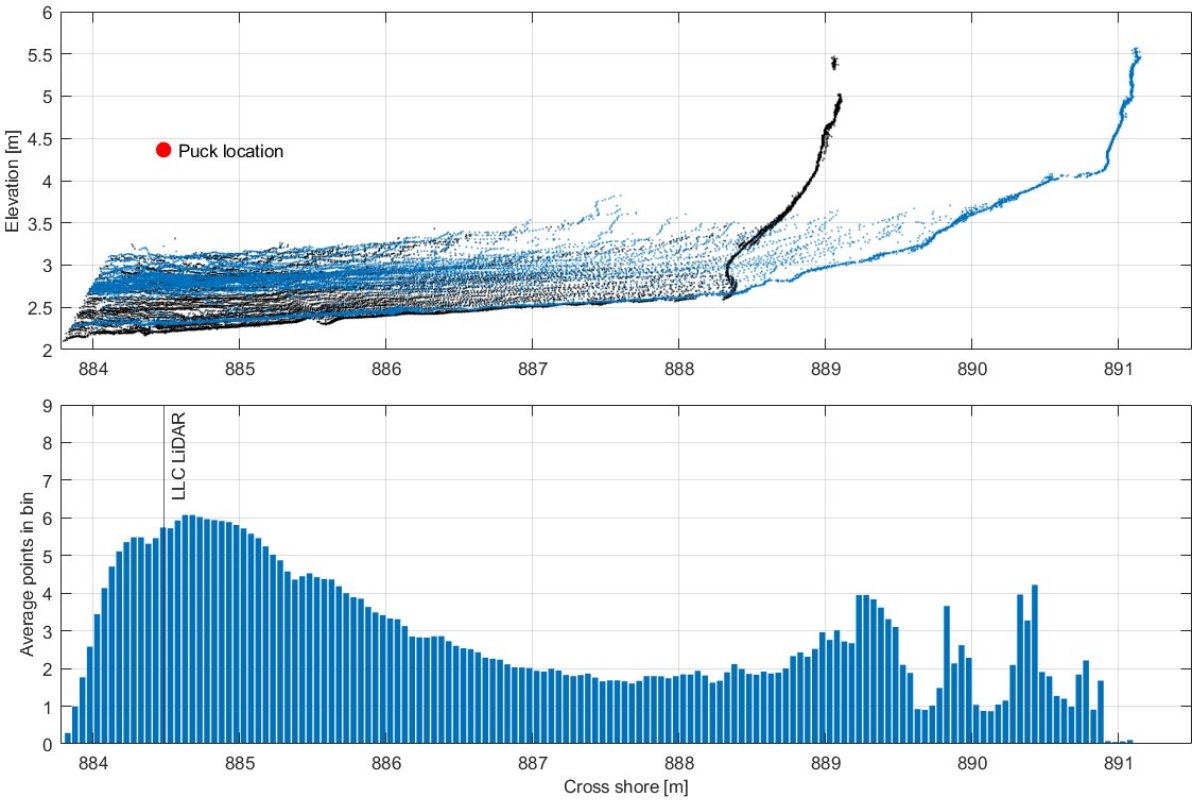

Figure 2.31: Top figure shows the LLC LiDAR point cloud of the first 45 seconds in black, and the last 45 seconds of the point cloud in blue during during 16:00 to 16:50 UTC+1. The bottom figure shows the number of points in cross shore direction of the the grid of the LLC LiDAR point cloud with $dx = 15cm$ and $dt = 0.2s$ during the same time range. The vertical line and text in the plot indicate the cross shore position of the LLC LiDAR. In total, there are a 189 bins in cross shore direction.

Extracting elevation time series at the pressure sensor location

One of the goals of this research is to compare the LLC LiDAR to the pressure sensor. In order to achieve this, the elevation of the LLC LiDAR point cloud needs to be extracted at the location of the pressure sensor. The pressure sensor at location 3b (during the January deployment) to be more precise. The cross shore location of the pressure sensor has already been determined (in Section 2.4.1) and is $x_{rbr3b} = 885.72m$. This is located within the FOV of the LLC LiDAR. In alongshore orientation, the two instruments are $1.65m$ apart from each other. It is assumed that the alongshore differences are minimal. The height of the point cloud of the LLC LiDAR at the location of the pressure sensor has been extracted (see Figure 2.32).

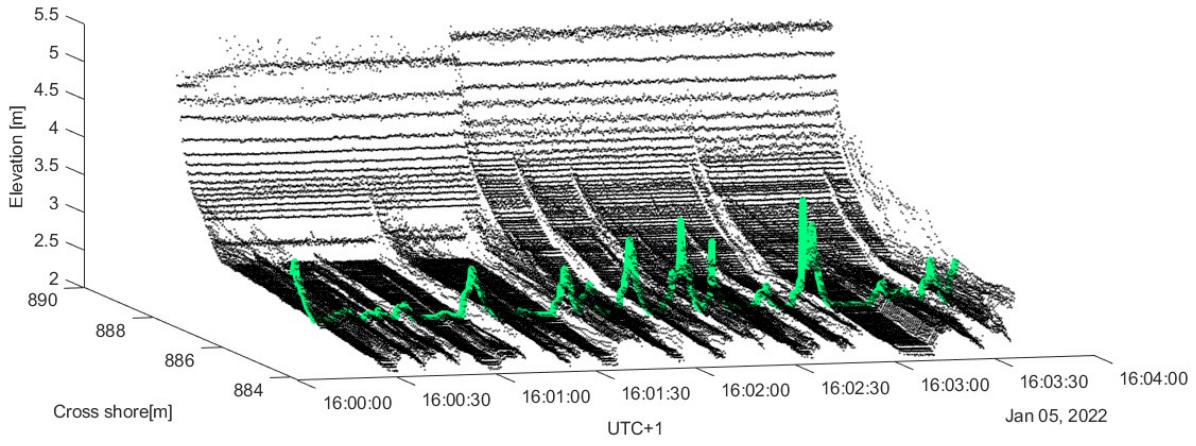

Figure 2.32: A section of the LLC LiDAR point cloud with a green line indicating the data points at the same crosshore distance as the pressure sensor at location 3b.

Time synchronisation
An error in clock of the LLC LiDAR has been corrected by fitting the dataset of the LLC LiDAR to the pressure sensor. The pressure sensor at location 3b (during the January deployment) to be more precise. The internal clock of the LLC LiDAR has been corrected around 3 months in advance of the measurements, meaning a correction is necessary to adjust the dataset of the LLC LiDAR to the correct time. The error of the internal clock is called the Time Error (TE). The TE over the duration has been in the order of seconds. The time series from the pressure sensor has already been synchronized in time, and is as such regarded as having the correct time.

The best fit of the LLC LiDAR data and the pressure sensor has been found by identifying the largest correlation (r) between the two datasets. By correcting the LLC LiDAR dataset by $+3.9s$, the pressure sensor and the LLC LiDAR data sets have the highest correlation (r_{fit}). Table 2.5.

Segment	r_{fit}
16:00 - 16:25	0.91
16:25 - 16:50	0.95
17:00 - 17:25	0.95
17:25 - 17:50	0.95

Table 2.5: The corner coordinates of the LLC LiDAR during the January 5th event. The center is the mean of all the corner coordinates.

Extracting morphodynamic data
The morphodynamics have been identified from the point cloud by finding the cross sections during moments of run downs. Since the LLC LiDAR has not measured the entire runup and run down, the morphology should be the lowest elevation measured by the LLC LiDAR. For this reason, cross sections are created by finding the lowest elevation in each cross shore cell (dx) during certain time intervals (Δt). The time interval has been chosen such that it is certain a run down event takes place during the time interval. This is in order to be certain the morphology is extracted and no hydrodynamics are included. The time interval has been chosen iteratively, and depends on the swash period, and water level during the event.

The ideal time interval has been investigated by looking at the outcome of the of the different time intervals. In this evaluation, several time intervals have been used. The ideal morphology extraction is found when using a time interval of $\Delta t = 60s$ (see Figure 2.33). When using a lower time interval, the beach in the cross section would be elevated. This elevation change is around $10cm$ in 1 minute, and would be too large to be able to be attributed to morphological change. This means part of the hydrodynamic data in the point cloud would also have been extracted together with the morphology when a lower time interval would be used.

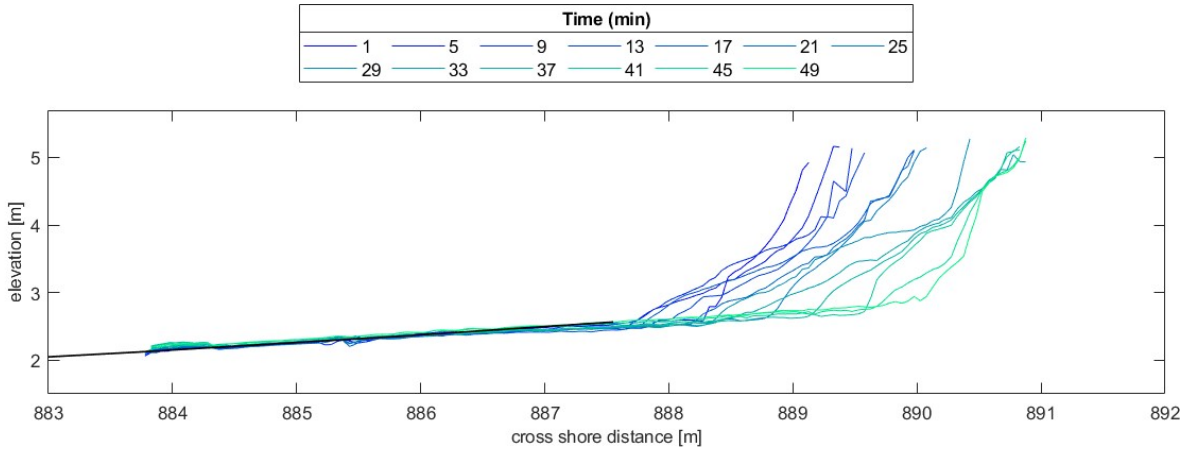

Figure 2.33: Cross shore morphology time series between 15:00 and 15:50 UTC+1. Time series in the plot has a time interval duration of 60s. Large dune retreat of around 2 meters is visible during this time periods.

Extracting hydrodynamic data
The hydrodynamic motion in the dataset is extracted by removing the morphology from the LLC LiDAR data. A cutoff height is created by adding $10cm$ to the morphology data. The $10cm$ cutoff height is introduced otherwise many points remain in the dataset from the LLC LiDAR. Any data points lower than the cutoff height are removed from the LLC LiDAR dataset. This method gets rid of most of the morphology in the dataset, and any remaining data points are removed manually. The manual removal of the data points is only minimal. The remaining points are mostly located around moments where slumping has occured. Figure 2.34 shows a comparison between the hydrodynamic motions and the full morphology.

The waterline has been extracted from the hydrodynamic motions. At each time interval, the point with maximum excursion in cross shore direction ($x(t)$) was selected. This results in a time series from the water level of the maximum hydrodynamic excursion. The waterline elevation can be found in Figure 2.34.

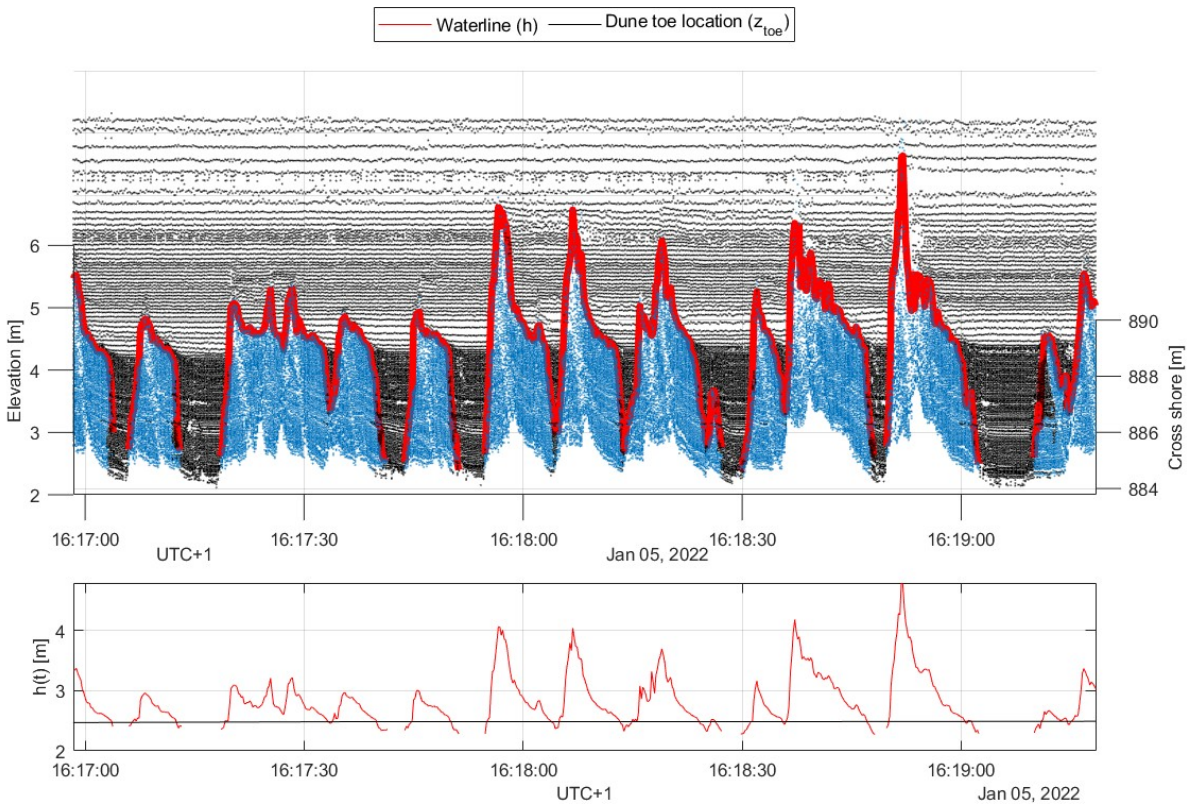

Figure 2.34: The waterline has been extracted by selecting a series of points with maximum cross shore excursion. The top plot shows the hydrodynamic data in blue, and the data from the LLC LiDAR in black. The red line represents the extracted waterline. The bottom plot shows the waterline, in red, relative to the dune toe, in black.

Runup heights during collision conditions

During the collision conditions, the maximum runup elevations have been extracted from the swash motions by using the same technique used in Section 2.4.2, with one difference, the waterline elevation from the collision dataset is discontinuous (see Figure 2.34). For this reason, the following solution has been found in order to derive the (partial) distribution of the discontinuous waterline elevation. In this solution, the amount of zero down crossings from the pressure sensor at location 2b ($N_{pressure}$) and the LLC LiDAR (N_{lidar}) are compared. In this comparison, the sum of zero down crossings of pressure sensor 2b are assumed to be the total amount of zero down crossings in the swash zone. Thus, the percentage of runup excursions missed by the LLC LiDAR (P) have been calculated by using Equation 2.13.

$$P = \left[1 - \frac{N_{lidar}}{N_{pressure}}\right] 100\% \tag{2.13}$$

Using this method, an approximation of the amount of missing surge events has been calculated. The approximated gap within the LiDAR data is summarized in Table 2.6.

Segment	$N_{lidar}[-]$	$N_{pressure}[-]$	$P[\%]$
16:00 - 16:25	158	205	23
16:25 - 16:50	181	223	19
17:00 - 17:25	148	189	22
17:25 - 17:50	112	193	42

Table 2.6: Approximation of missing percentage of runup events.

From this approximation of missing excursion events, the (partial) cumulative distributions have been created (see Figure 2.35).

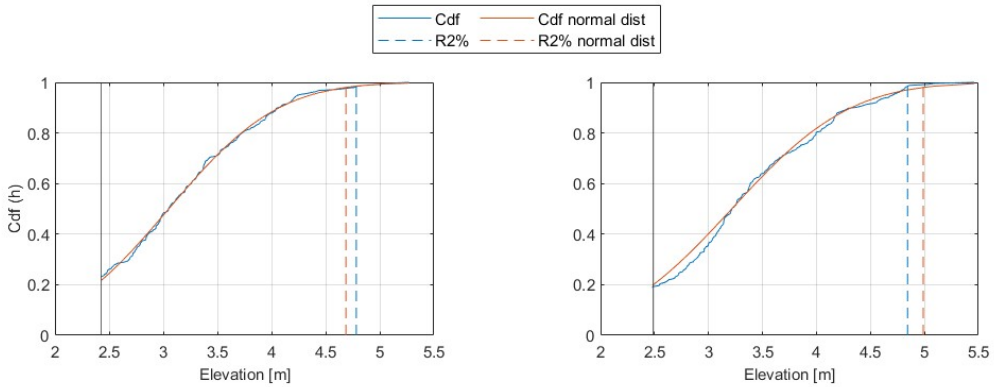

Figure 2.35: The runup elevations of the incomplete waterline. The vertical lines (black and red) show the corresponding $R_{2\%}$ levels of the segments.

2.5. Beach conditions

The beach and dune morphology at the fieldwork site during the experiment were in constant fluctuation. During the events, the upper part of the beach profile has been measured before and after the high water event using an RTK-GPS (Real-Time-Kinematic Global-Positioning-System), which gives an overview of the bed level changes during the events. The GPS is also used to measure the beach conditions before and after each event, in order to see the morphological changes during the high water event. In between the events of December 1st to December 2nd, the beach profile underwent large changes (see Figure 2.36). These changes are mainly caused by a highly energetic event during the night of December 1st to December 1nd. During this night, a large section of the dune and the beach has been eroded, resulting in the beach profile changes between the December 1st and December 2nd events.

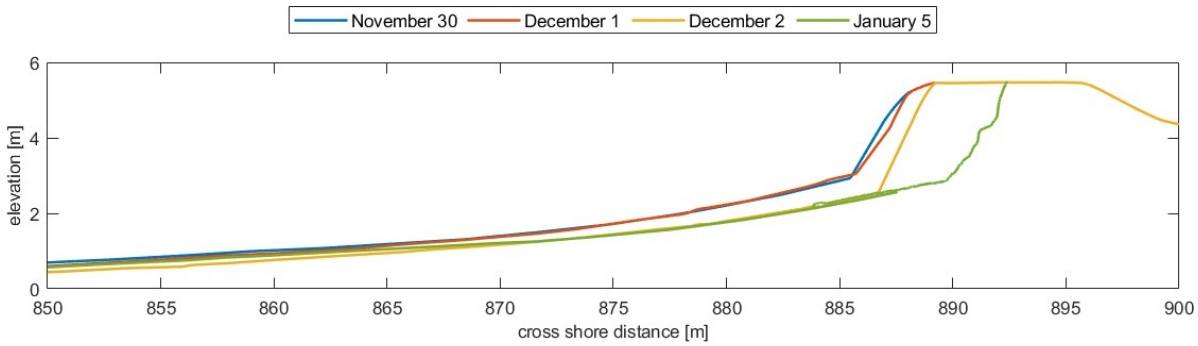

Figure 2.36: The beach profile measured using an RTK-GPS system at the day of each event. This plot shows the swash events of November 30, December 1 and December 2, as well as the event during the collision conditions. The dune toe height during the swash events is $2.97[m]$, $3.08[m]$ and $2.53[m]$ respectively. The dune toe height of the collision event is between ????.

During the events, the upper part of the beach profile has been measured before and after the high water event, which gives an overview of the bed level changes during the events. The beach profiles during the events from November 30th to December 2nd, including the before and after profiles, are presented in Figure 2.37. Only minor bad level elevation changes took place during the swash events. The maximum bed level elevation change, which was 10cm, was reported on December 1st.

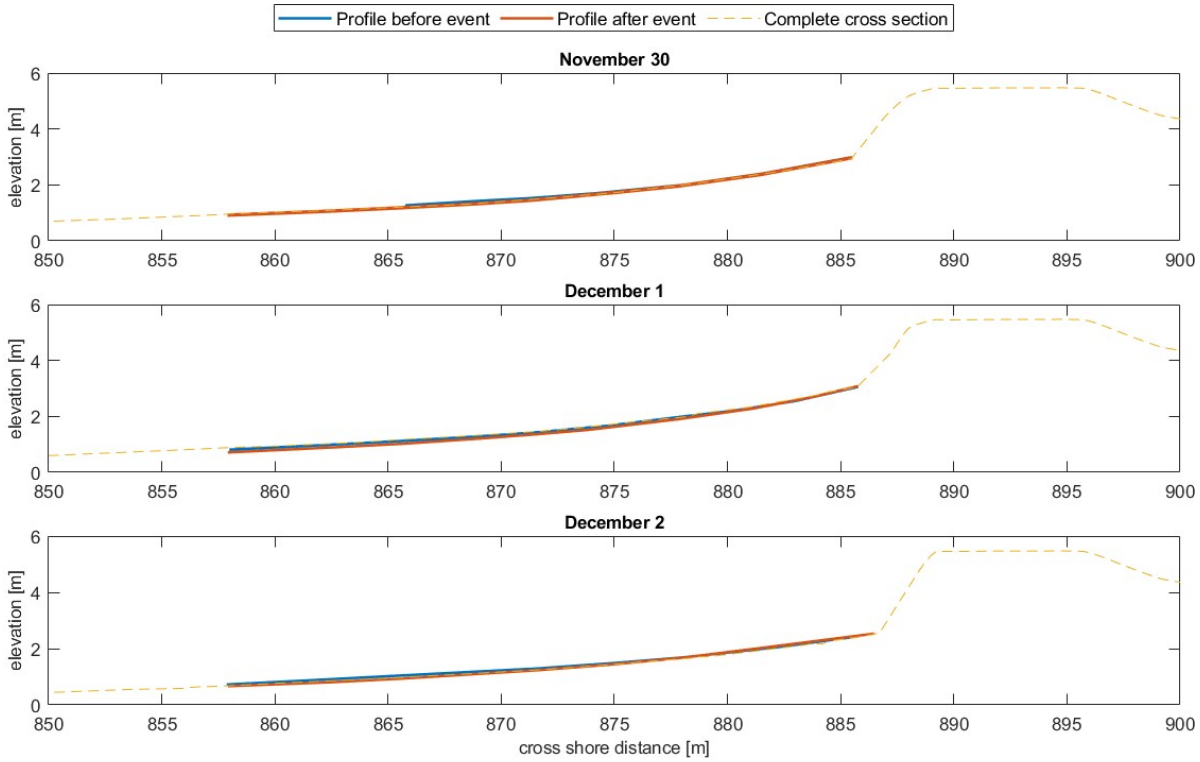

Figure 2.37: The beach profile is measured before and after each high water event. Changes between the before and after situations are minimal. The largest beach level fluctuation at a certain cross shore location is observed in the event of December 1st, which has a maximum difference of $0.07[m]$.

During collision conditions the profile has also been measured before the start of the high water event. During the event, the LLC LiDAR has been used to measure the topography of the beach. From the data of the LLC LiDAR, Large dune retreat is visible during the event, and the dune face is undergoing continuous slumping (see Figure 2.38). During this time, the dune retreat was around 4 meters.

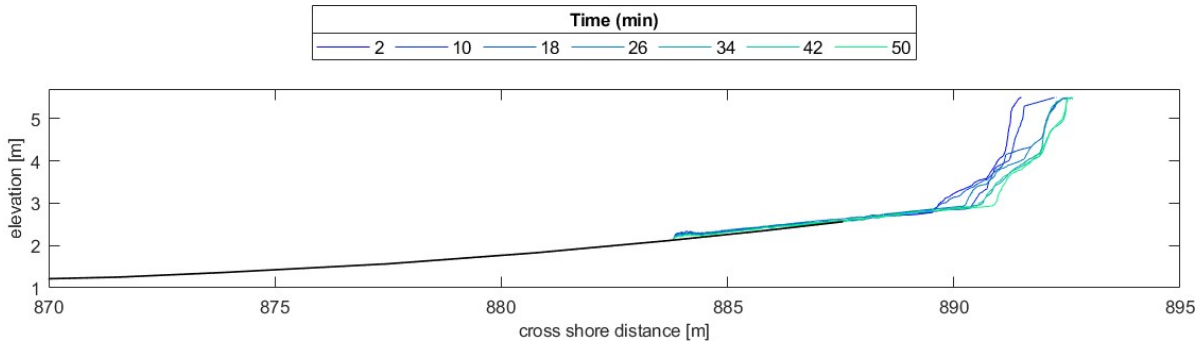

Figure 2.38: The complete beach profile is measured before the collision event. Changes of an upper section of the beach and the duneface are measured using the lidar from 16:00 untill 16:50. Starting at 16:00 changes in the beach profile can be followed. During this time segment the dunface has retreated several meters due to the forcing of the waves.

The dune toe has been tracked during the collision event by using the methods described in Section 2.4.3. The tracked dune toe location can be seen in Figure 2.39, together with the morphological changes during the Jnauary 5th event.

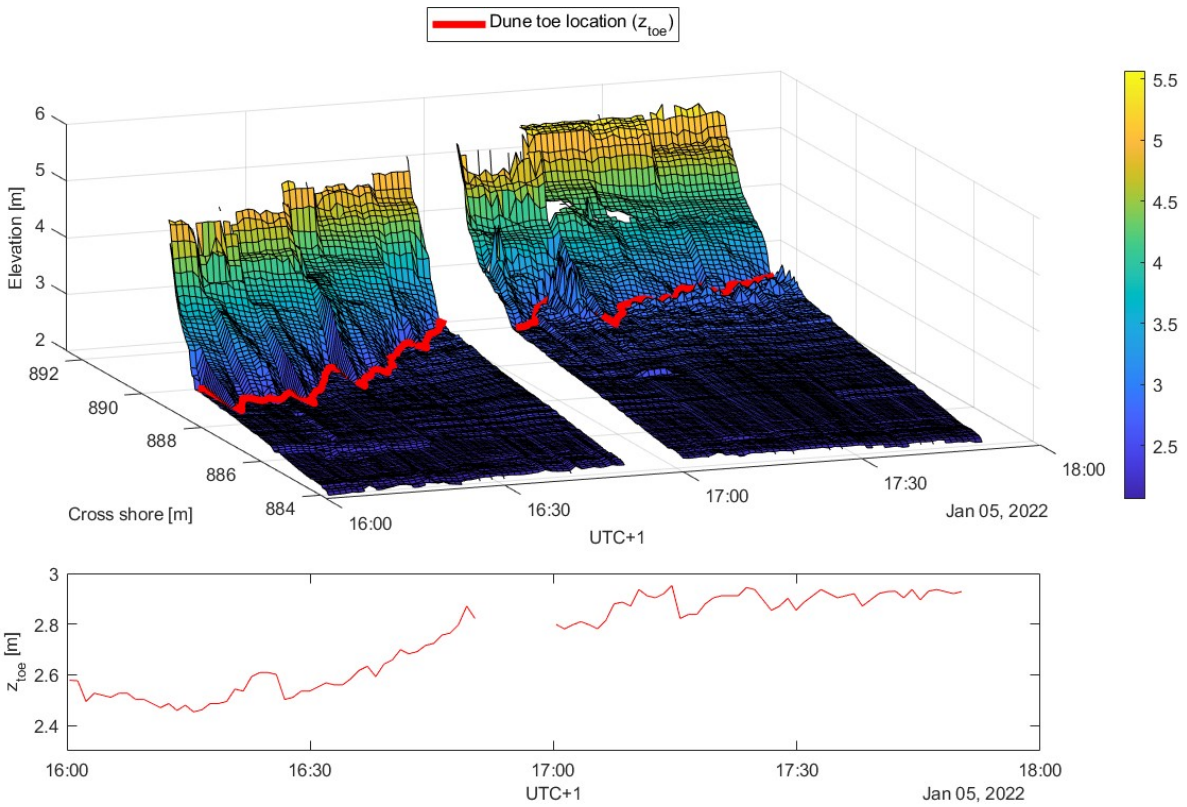

Figure 2.39: The plot above shows the dune retreat over time during the entire all the segments of the January 5th event. The red line in this plot show the location of the dune toe in the plot.

For each time segment during the events, the average beach slope, Dean parameter and Irribarren number have been calculated. The beach slope has been calculated by taking the average beach slope between two ranges of the total total setup elevation during the segments (see Equation 2.14). The method of deriving the beach slope is the same as the methods used by Stockdon et al., 2006, Brinkkemper et al., 2013 and de Beer et al., 2021. This has been done in order to provide consistency between studies, and to find out if this simplification of the beach slope is still valid during collision conditions.

$$\beta_f = \frac{h_{upper} - h_{lower}}{\Delta x} \tag{2.14}$$

$$h_{upper}, h_{lower} = \mu_{total} \pm 2\sigma_h \tag{2.15}$$

Where h_{upper} and h_{lower} indicate the upper and lower boundary which are used to calculate the average beach slope. μ_{total} is the sum of all setup elevations ($\mu_{tide} + \mu_{wind} + \mu_{wave}$) and σ_h is the standard deviation of the total water level during each time segment.

Since the waterline of the January event is discontinuous, the standard deviation of the waterline could not be calculated. Another method has been realized for the purpose of calculating the beach slope during collision conditions. The proposed method calculated the ratio between: $R_{2\%}/2\sigma_h$. The ratio between runup heights and the standard deviation of the waterline was quite consistent during the swash conditions. The ratio during swash conditions was $R_{2\%}/2\sigma_h = 1.55$, calculated with a standard deviation of 0.08. Thus a the upped bounds during the collision conditions were calculated according to Equation 2.16.

$$h_{upper}, h_{lower} = \mu_{total} \pm R_{2\%}/1.55 \tag{2.16}$$

Since the calculation for the beach slope during collision conditions seemed quite artificial, another method has also been employed. This method still used the same lower limit of $h_{lower}] = \mu_{total} - R_{2\%}/1.55$, but now the upper limit of the beach slope is the location of the dune toe (z_{toe}). The new method proposed for calculating the dune slope is calculated from: $\mathrm{B}_d = \frac{z_{toe} - h_{lower}}{\Delta x} h_{lower}]$.

The Dean parameter is calculated using a constant sediment fall velocity of $\omega = 0.0268[m/s]$, which is an estimate used by van Gent et al., 2008 in their study on dune erosion at the Dutch coast, and is assumed to be comparable to this study. Other parameters are indicated in tables 2.1 and 2.7.

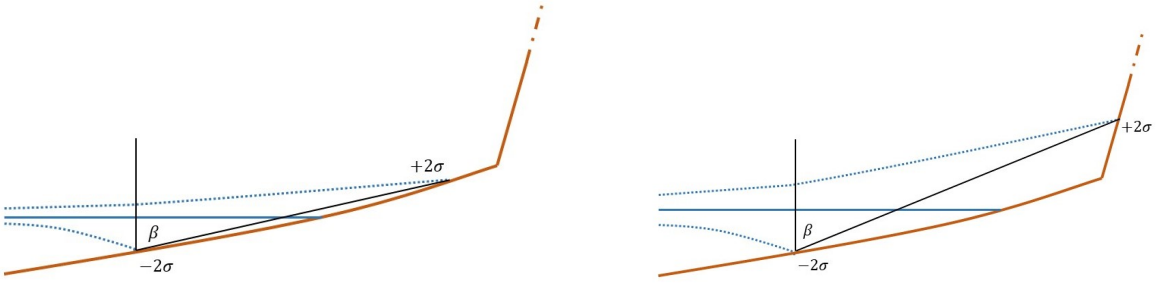

(a) Beach slope during swash conditions.

(b) Beach slope during collision conditions.

Figure 2.40: An abstract representation of the derivation of the average beach slope during swash conditions. The locations of -2σ and $+2\sigma$ show the locations from which the beach slope has been averaged. The left Figure represents the derivation of the beach slope during swash conditions and the right Figure represents the derivation of the beach slope during collision conditions. Contrary to the swash conditions, the upper bound now lies on the dune face.

The beach characteristics (ξ and Ω) differ significantly between swash and collision conditions. All the beach characteristics during the collision event are summarized in Table 2.7. During swash conditions, the beach characteristics were relatively equal, but during collision conditions both the Irribarren number and the beach slope increased compared to the swash conditions. The Irribarren number indicated that the breaker type were mostly spilling breakers during swash conditions, whilst during collision conditions the breaker type shifted to the plunging breaker regime. The breaker type moved just into the plunging breaker regime during some instances in swash conditions. During collision conditions, the beach slope, and thus the Irribarren number, have been calculated using just the beach slope or with the dune face in mind. Adding the dune slope to the analysis changes the beach slope and Irribarren number drastically.

Event date	Segment	$1/tan\beta$	Ω	ξ
November 30	10:18 - 10:51	14.13	15.2	0.37
	10:51 - 11:24	12.96	14.8	0.41
	11:24 - 11:57	13.35	15.0	0.39
	11:57 - 12:31	15.06	14.9	0.35
	12:31 - 13:04	18.20	13.7	0.30
	13:04 - 13:37	22.49	14.3	0.23
December 1	10:42 - 11:14	16.18	13.0	0.35
	11:26 - 11:59	11.05	13.7	0.49
	11:59 - 12:32	10.19	14.9	0.52
	12:32 - 13:06	10.20	15.2	0.52
	13:06 - 13:39	10.93	16.3	0.47
	13:39 - 14:12	12.35	15.8	0.43
December 2	12:33 - 13:06	13.74	11.8	0.48
	13:06 - 13:40	13.02	11.1	0.51
	13:40 - 14:13	13.42	11.0	0.50
	14:13 - 14:46	15.38	11.0	0.43
	14:46 - 15:20	19.91	10.8	0.33
	15:20 - 15:52	21.81	9.4	0.32
January 5 (β_d)	16:00 - 16:25	15.52	11.39	0.72
	16:25 - 16:50	11.43	11.35	0.71
	17:00 - 17:25	12.25	11.35	0.94
	17:25 - 17:50	12.97	11.35	0.94
January 5 (β_f)	16:00 - 16:25	9.54	11.39	1.14
	16:25 - 16:50	6.87	11.35	0.94
	17:00 - 17:25	8.02	11.35	0.94
	17:25 - 17:50	9.81	11.35	0.94

Table 2.7: Beach conditions calculated from offshore parameters and beach shape. $tan\beta$ is the average slope between station 5 and the beach toe. The Irribarren number is calculated using the offshore significant wave height and wave length. 'β_d' Indicates that the duneface is included in the computation of the beach slope.

2.6. Variance density spectra

In order to find the differences in the INC band and the IG band within the swash motions and the incoming wave field, variance density spectra have been calculated (see Equation C.2). Variance density spectra can be a useful method when looking at the shift in energy from the higher wave frequencies to the lower wave frequencies.

$$E(f_i) = \frac{1}{\Delta f_i} E\{\frac{1}{2} a_i^2\} \tag{2.17}$$

In which $E(f_i)$ is the variance density spectrum for all f_i. Δf_i is the frequency interval between the harmonic components, and a_i is the wave amplitude of the harmonics. The variance density spectra has been calculated for each segment of the pressure sensors and the waterline extracted from the runup camera. The variance density spectra has not been calculated for the waterline from the LLC LiDAR in Section 2.4.3, since the LLC LiDAR did not cover the full runup and run-down.

The time segments have been separated into a blocks (p) with the aim to create accurate variance density spectra with a long enough block period to capture the IG waves. The block length should not be lower than the maximum wave period for long waves, which is around $150s$ for the IG waves. Usually, acceptable resolutions are reached using $p = 20-30$ and $D = 15-30[min]$. As stated in Chapter 2.1, time segments with a length of 25 - 30 minutes have been used, which is acceptable considering the above. Separating the time segments into 20 blocks would result in a maximum wave period of 90 seconds, which would not encapsulate the entire long wave spectrum. For this reason, the data has been divided into 15 blocks, which can still captures wave periods of $120s$. Lowering p would result in an error in the variance density spectra that would be too large. An example of the segment during December 1st can be found in Figure 2.41.

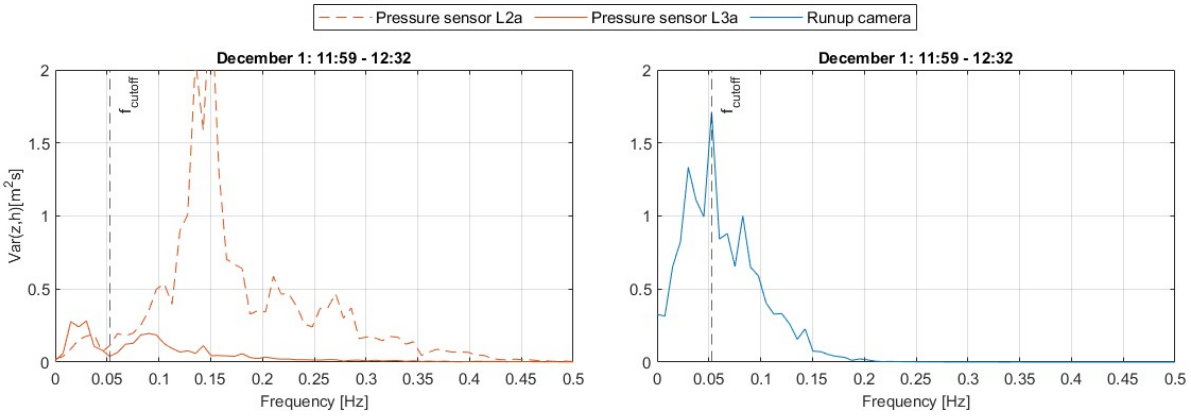

Figure 2.41: The plots show the ED-spectra at L1a and L2a during December 1st. A clear reduction in the total variance can be seen when comparing the spectrum at L2a to L3a. This reduction is mainly visible in the high frequency part of the spectrum. In the low frequencies the spectrum increased. This increase is possibly by the transfer of the energy of the high frequencies to the low frequencies. The vertical line indicates the cutoff frequency between the INC and IG band in the frequency spectrum.

During the January event, the spacing of the pressure sensors was much closer (see Figure 2.5) which resulted in relatively similar variance density spectra. The pressure sensors were located just below the swash zone, meaning the energy in the waves was already significantly dissipated when arriving at L2b and L3b.

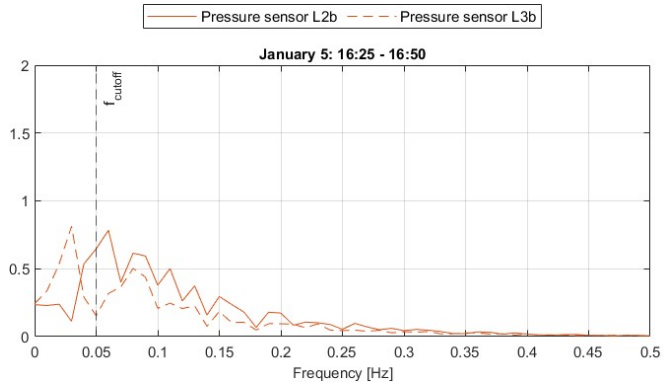

Figure 2.42: The ED-spectra at L1b and L2b during the peak of January 5th. Since the locations of the instruments are much closed compared to the swash events, the change in variance between L2b and L3b is much smaller. however, a shift of energy towards the lower frequencies is still visible. The vertical line indicates the cutoff frequency between the INC and IG band in the frequency spectrum.

The separation of the INC band and IG band done by finding the frequency cutoff between the two spectral bands (f_{cutoff}). Usually a value of $0.05Hz$ is taken as the frequency cutoff between the IG band and the INC band, but this value can also be site and event specific, which has been evaluated for this experiment. The cutoff frequency has been located by finding the minimum value of the ED-spectra of the pressure sensors within the range of $0.03 - 0.07Hz$, and averaging over all time segments during each event. Locations L1a and L2a have been used for this calculation during the swash condition events, and location L2b during collision conditions. Locations L3a and L3b have been omitted from this evaluation, since the wave were mostly dissipated before reaching this station, and the ED-spectrum at these location mostly showed only energy present within the IG band. The border locations of each event can be found in the list below, and have also been plotted in Figures 2.41 and 2.42.

- November 30: $f_{cutoff} = 0.058Hz$
- December 1: $f_{cutoff} = 0.053Hz$
- December 2: $f_{cutoff} = 0.037Hz$
- January 5: $f_{cutoff} = 0.050Hz$

2.7. Characteristic wave heights

Characteristic wave heights within the IG band and INC band can calculated from the ED-spectra. Characteristic wave heights have been be computed from the spectral moments using Equations 2.18 and .

$$m_{0,IG} = \int_0^{f_{cutoff}} f^n E(f) \mathrm{d}f \qquad \text{for} \quad n = -1, 0, 1, 2 \tag{2.18}$$

$$m_{0,INC} = \int_{f_{cutoff}}^{\infty} f^n E(f) \mathrm{d}f \qquad \text{for} \quad n = -1, 0, 1, 2 \tag{2.19}$$

(2.20)

In which m_n is the spectral moment, f is the frequency, n is the order of the spectral moment and $E(f)$ is the variance within the specturum. Characteristic wave heights (H_s and S) have been calculated form the zeroth moment (m_0) using Equation 2.21.

$$H_s = 4\sqrt{m_0} \tag{2.21}$$

Combining Equations 2.18 and 2.21 and combing Equations 2.19 and 2.21 give Equations 2.22 and 2.23.

$$H_{s,IG} = 4\sqrt{\int_0^{f_{border}} E_H(f) \mathrm{d}f} \tag{2.22}$$

$$H_{s,INC} = 4\sqrt{\int_{f_{border}}^{\infty} E_H(f) \mathrm{d}f} \tag{2.23}$$

In which $E_H(f)$ is the variance density spectra of the waves at the pressure sensors and $E_S(f)$ is the variance density spectra of the runup. Table B.1 shows the outcome of the computations of the characteristic wave heights ($H_{s,IG}$, $H_{s,INC}$, S_{IG} and S_{INC}) during each segment.

2.8. Runup characteristics

By computing the runup characteristics in the swash spectra, the differences between swash and collision conditions can be identified. Increases or decreases in $\mu_w ave$, S_{INC} and S_{IG} are connected to changes in the coastal environment (Davidson-Arnott et al., 2019). The runup characteristics calculated as followed. Firstly, the mean waterline is subtracted from the tide and wind setup in order to determine the wave setup (see Equation 2.24).

$$\mu_{wave} = h_{mean} - \mu_{tide} - \mu_{wind} \tag{2.24}$$

Secondly, the INC and IG swash heights can be computed from the swash spectra. S_{INC} and S_{IG} can be calculated using Equations 2.25 and 2.26.

$$S_{IG} = 4\sqrt{\int_0^{f_{cutoff}} E_S(f) \mathrm{d}f} \tag{2.25}$$

$$S_{INC} = 4\sqrt{\int_{f_{cutoff}}^{\infty} E_S(f) \mathrm{d}f} \tag{2.26}$$

Where $E_S(f)$ is the swash spectrum. The results from the calculations can be found in Table 3.3. The complete swash spectra could not be determined during the collision conditions since only a discontinuous waterline is extracted from the LiDAR measurements. For this reason, S_{INC} and S_{IG} could not be determined, and μ_{wave} could only be estimated by using the offshore conditions. However, data from the nearshore pressure sensors have been used to determine the IG and INC components relative to each other. The wave setup is estimated using Equation 1.5 and 1.6. Equation 2.27 proposed by Battjes and Stive, 1985 has been used in order to derive γ_b. The empirical formula for this breaker

parameter has been derived in a field study at the Dutch coast, which is assumed to have similar conditions the the Fieldwork site used in this experiment. Since the influence of the beach characteristics is to be investigated, this breaker parameter has been chosen, since it does not implement the beach slope into the equation.

$$\gamma_b = 0.39 + 0.5tanh(33s_0) \tag{2.27}$$

Where s_0 is the offshore wave steepness. Swash conditions have been used to compare the the outcome of the derivation to the field measurements, which confirmed the outcome of Equation 2.27.

2.9. Statistical quantification

In order to give a statistical indication to in the results, the root mean square error ($RMSE$), the coefficient of determination (R^2) and Wilmott's index of agreement (d) have been calculated . This is for both the differences between the pressure sensor and LLC LiDAR datasets, and the linear dependence between runup and offshore wave or beach parameters. The $RMSE$ and R^2 have been calculated according to Equations 2.28 and 2.29.

$$RMSE = \sqrt{\frac{\sum_{i=1}^{N} |X_i - Y_i|^2}{N}} \tag{2.28}$$

$$R^2 = 1 - \frac{\sum_{i=1}^{N}(X_i - Y_i)^2}{\sqrt{\sum_{i=1}^{N}(X_i - \bar{X}_i)^2}} \tag{2.29}$$

With X_i as the observed value, Y_i as the fitted value and dataset. Willmott's index of agreement is another method of comparing two datasets to each other (Willmott, 1981). Albeit between a dataset of computed values and a dataset of measured values, or 2 datasets of measured values. The index ranges between 2 values, $d = 1$ indicating the datasets are in perfect agreement, and $d = 0$ meaning the datasets are not in agreement. The index is computed as indicated in Equation 2.30.

$$d = 1 - \frac{\sum_{i=1}^{N}(X_i - Y_i)^2}{\sum_{i=1}^{N}(|X_i - \bar{X}_i| + |Y_i - \bar{X}_i|)^2} \tag{2.30}$$

3

Results

In this Chapter, the processed data from the fieldwork experiment will be analysed with the aim of answering the research questions of this thesis. The research questions are answered in chronological order, starting with the comparison of two measuring techniques. Thereafter answering how the composition of the runup characteristics are during swash and collision conditions and lastly comparing the measured runup heights to the modelled runup heights calculated with the runup equation proposed by Stockdon et al., 2006.

3.1. LLC LiDAR evaluation

Since the LLC LiDAR is a new instrument used in coastal fieldwork deployments, data from the LiDAR is evaluated in terms of effectiveness of measuring hydrodynamic conditions. In order to evaluate the effectiveness of measuring the total water level, the water level elevation of the LLC LiDAR is compared to water level from the pressure sensor (see Figure 3.1).

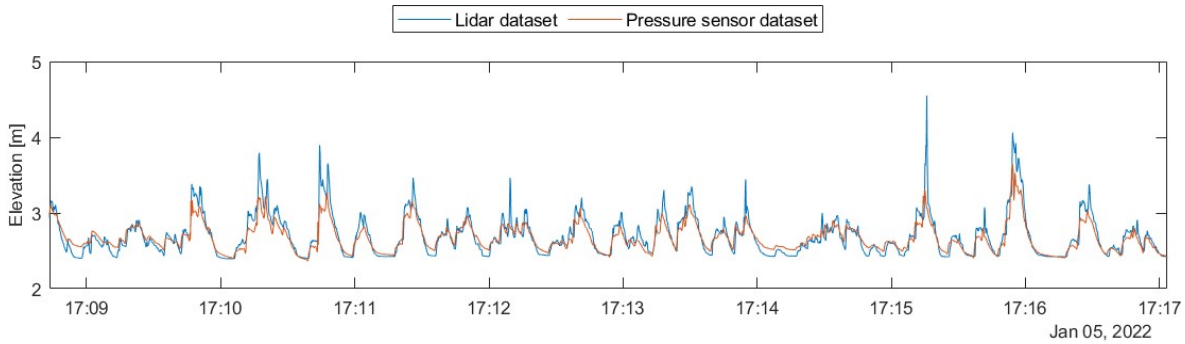

Figure 3.1: The section of the LiDAR dataset is compared to the pressure sensor measurements at location 3 during the storm conditions of the January 5th event.

A few things become obvious in the comparison. Firstly, both measurements coincide pretty well visually, which is also seen in the statistical parameters (see Table 3.1). Secondly, main differences between the LLC LiDAR and pressure sensor lie in the peak elevation of the runup events (see Figure 3.1 at 17:15). Peaks in the LLC LiDAR dataset are higher than the peaks of the pressure sensor dataset (see Table 3.1). Thirdly, in the lower end of the water Figure 3.2 there is a border on the bottom left side of the plot, which is the the bed level elevation measured by the LLC LiDAR.

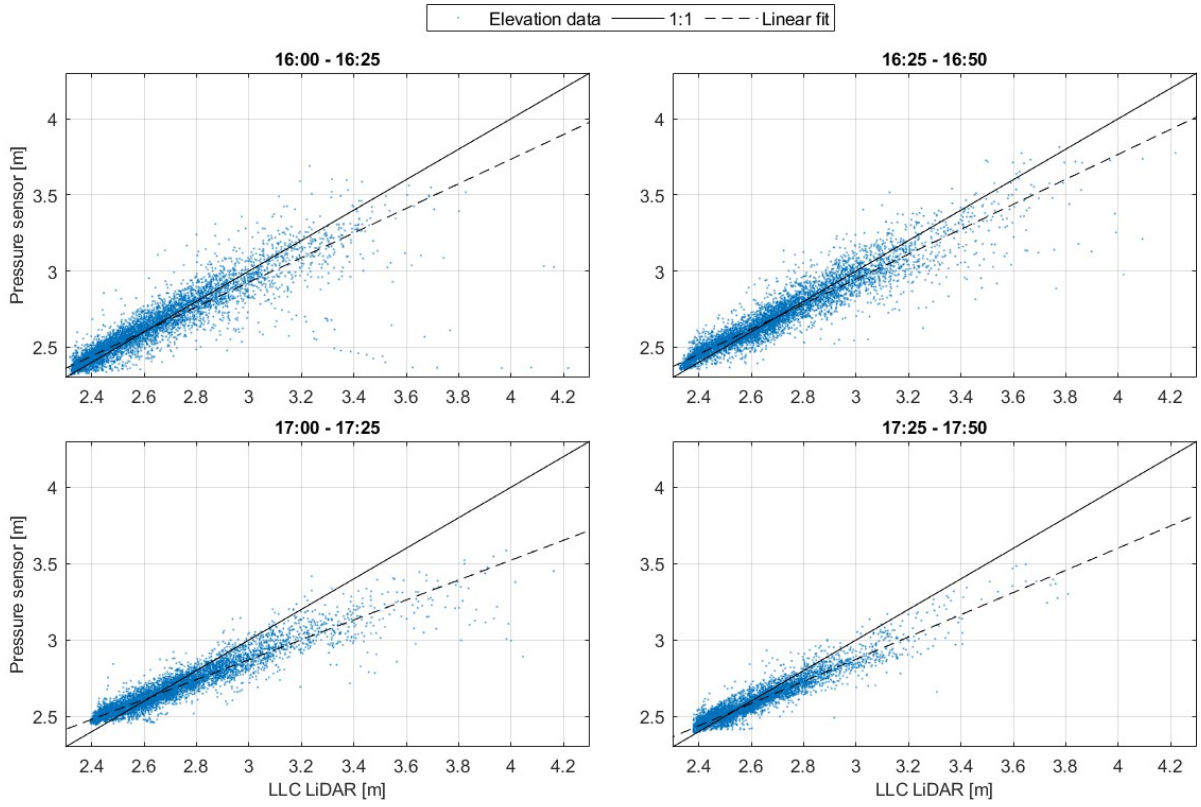

Figure 3.2: LiDAR and pressure sensor elevations are compared at each segemnt of January 5th. The left graph is the time segment of 17:00 to 17:25 and the right figure is the time segment of 17:25 until 17:50.

The linear fit in Figure 3.2 shows a systematical difference between the LLC LiDAR and the pressure sensor at high elevations. The LLC LiDAR tends to measure the same waves higher than the pressure sensor. The best linear fit is can be fitted with the equation: $y = az + b$, in which a and b are the fitted constants and y is the elevation of the pressure sensor, z is the elevation of the LLC LiDAR. The Fit shows that the later segments have a larger linear difference compared tot the earlier segments. Segment 17:00 - 17:25 has the largest deviation from the 1:1 expected value. The statistical results of the comparison are summarized in Table 3.1.

Segment	$RMSE[m]$	$R^2[-]$	$d[-]$	a	b
Analysis of continuous waterline elevation					
16:00 - 16:25	0.10	0.78	0.93	0.81	0.5005
16:25 - 16:50	0.09	0.86	0.95	0.82	0.4848
17:00 - 17:25	0.11	0.61	0.90	0.65	0.9165
17:25 - 17:50	0.07	0.74	0.93	0.73	0.6938
Analysis of peak water levels					
16:00 - 16:25	0.13	0.74	0.87	-	-
16:25 - 16:50	0.11	0.78	0.92	-	-
17:00 - 17:25	0.18	0.34	0.83	-	-
17:25 - 17:50	0.11	0.65	0.91	-	-

Table 3.1: $RMSE$, R^2 and Willmott's d between the pressure sensor at location 8 and the LiDAR scanner during the segments of the January 5th. a and b are constants for the linear best fit of the pressure sensor data.

Table 3.1 indicates small errors between the two datasets. When Willmott's index gives $d \geq 0.86$, the two datasets are in good agreement, which is the case for all continuous waterline time segments. In the datasets of the peak water level elevations, the difference between the pressure sensor and the LLC LiDAR become larger. This confirms the conclusions of the visual observations of the two datasets.

3.2. Runup behaviour during swash and collision conditions

The characteristic wave heights (H_{IG}, and H_{INC}) and runup characteristics (μ_{wave}, S_{inc} and S_{IG}) are compared between the swash and collision conditions. In order to identify the changes in the runup characteristics during the conditions, the nearshore wave conditions and the waterline motion are analysed. The wave conditions have been inspected by determining the amount of dissipation in the INC waves and the IG waves.

The nearshore conditions during the swash conditions of December 1st are plotted in Figure D.2. The conditions during the collision conditions of January are plotted in Figure 3.4. The height of the runup spectra and pressure sensor spectra cannot directly be correlated since the runup data moves in a Lagrangian frame and the wave from the pressure sensor are measuring in an Eularian frame, which is also the reason why the spectrum from the runup camera is larger than the pressure sensors.

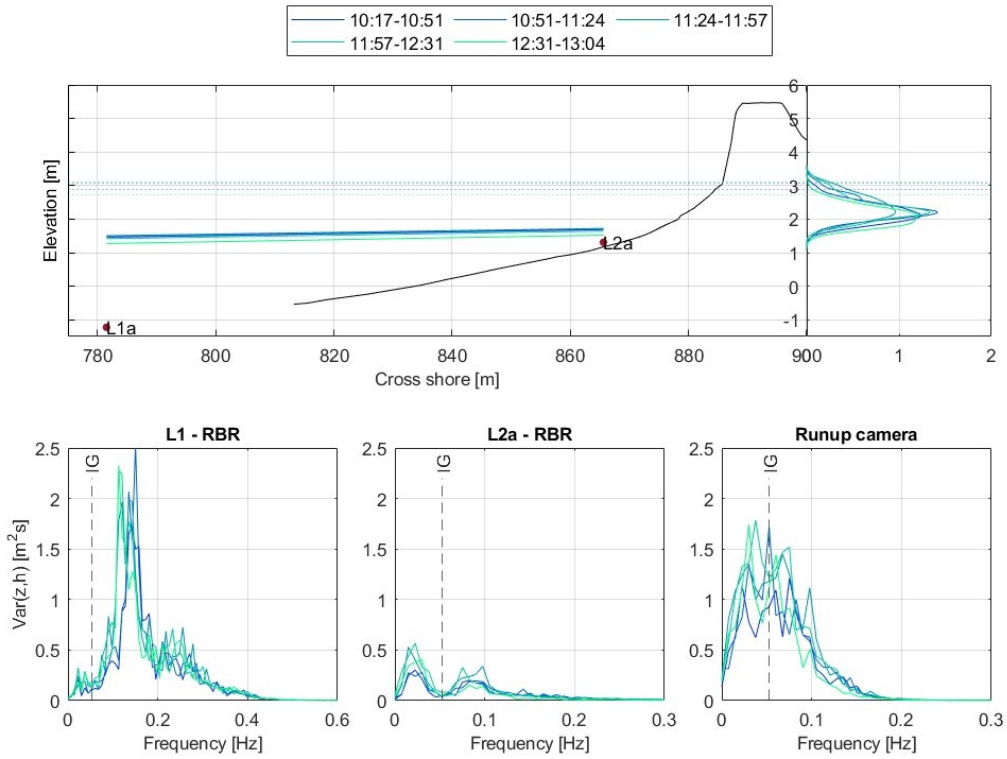

Figure 3.3: A summation of the data on December 1st. The top-left plot shows the beach profile together with the mean water levels at location L1a, location L2a and the total wave setup at the waterline. The gray area shows the FOV of the runup camera. The top right plot shows the runup distributions. The bottom plots show the ED-spectra at each location within the transect.

During December 1st, the water level elevation was well below the dune toe, and the maximum runup excursion only incidentally reached the dune toe. The runup elevation $R_2\%$ was also located below the dune toe. The situation during November 30th and December 2nd were similar to December 1st. A situational sketch of these events can be found in Appendix D. During the collision conditions on January 5th, the wave runup height went well above the dune toe. However, the total wave setup elevation (μ_{tide}+μ_{wind}+μ_{wave}) was still below the dune toe during each segment, which can be seen in Figure 3.4. Wave heights during the collision event ($H_0 = 3.31 - 3.60$) were much higher than during the swash events ($H_0 = 2.42 - 3.22$).

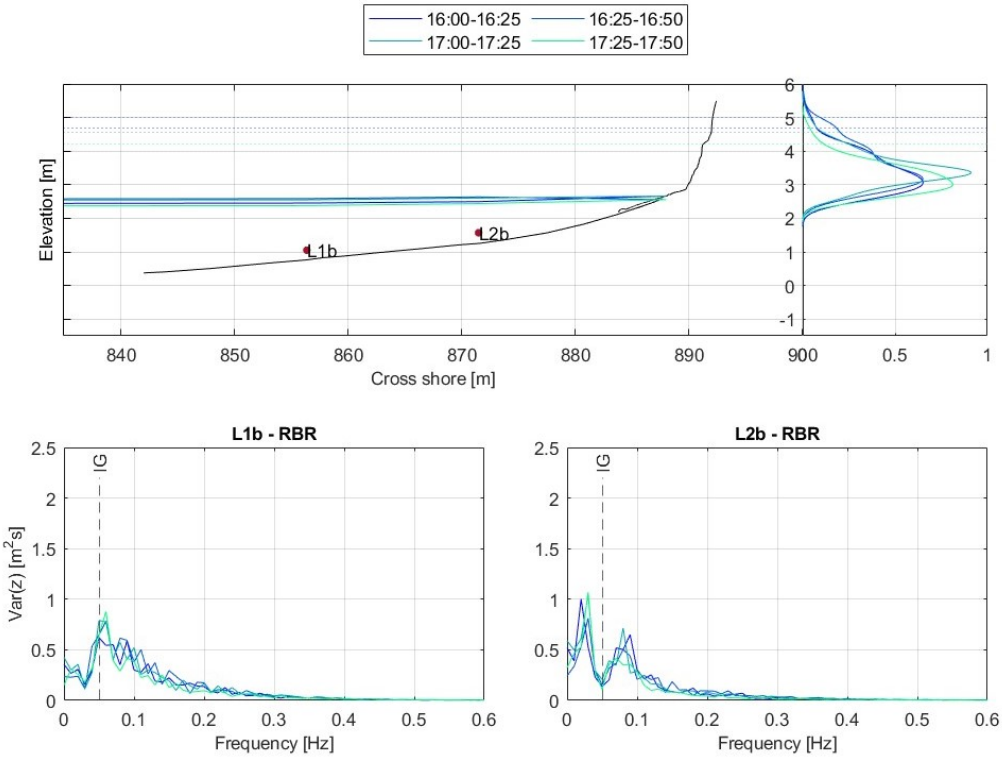

Figure 3.4: A summation of the data on January 5th. The top-left plot shows the beach profile together with the mean water levels at location L1b, location L2b and the total wave setup at the waterline. The gray area shows the FOV of the runup camera. The top right plot shows the runup distributions. The bottom plots show the ED-spectra at each location within the transect.

Wave dissipation

The spectra from the pressure sensors are evaluated in terms of incoming wave height in the INC band (H_{INC}) and IG wave height (H_{IG}). During the swash conditions, a shift in energy is found in the variance density spectra at location L1a to L2a (see Figure D.2). This is also shown in the characteristic wave heights in Table 3.2, where H_{INC} reduces significantly from L1a to L2a, while H_{IG} increases in size when comparing the wave height between location L1a to L2a.

The nearshore wave field during collision conditions showed similar characteristic wave heights to the swash conditions. The changed location of the pressure sensor between the collision and swash conditions limits the comparison between the swash and collision conditions. However, Locations L2a and L2b are in a quite similar position with regards to their average depth (see Table 3.2) and cross shore position, since both pressure sensors are located just before the swash zone. At these pressure sensor locations the energy in the INC band relative to the energy in the IG band does not appear to change between swash and collision conditions. This behaviour is also seen in the characteristic wave heights, since the ratio between H_{INC}/H_{IG} is relatively similar. This is also visually confirmed by the similarity of the variance density spectra of L2a and L2b.

	L1a			L2a		
Segment [hh:mm]	Depth [m]	$H_{s,IG}$	$H_{s,INC}$	Depth [m]	$H_{s,IG}$	$H_{s,INC}$
November 30						
10:18 - 10:51	2.50	0.25	1.54	-	-	-
10:51 - 11:24	2.55	0.27	1.51	-	-	-
11:24 - 11:57	2.52	0.24	1.45	-	-	-
11:57 - 12:31	2.42	0.26	1.49	-	-	-
12:31 - 13:04	2.29	0.26	1.42	-	-	-
13:04 - 13:37	2.10	0.26	1.43	-	-	-
December 1						
10:42 - 11:14	2.37	0.23	1.47	-	-	-
11:26 - 11:59	2.69	0.27	1.55	0.38	0.34	0.47
11:59 - 12:32	2.73	0.30	1.60	0.41	0.35	0.50
12:32 - 13:06	2.72	0.35	1.73	0.41	0.43	0.55
13:06 - 13:39	2.64	0.35	1.72	0.33	0.48	0.49
13:39 - 14:12	2.50	0.34	1.61	0.21	0.41	0.37
December 2						
12:33 - 13:06	2.41	0.27	1.49	0.29	0.32	0.40
13:06 - 13:40	2.48	0.24	1.52	0.34	0.32	0.45
13:40 - 14:13	2.44	0.30	1.44	0.28	0.32	0.40
14:13 - 14:46	2.27	0.21	1.35	-	-	-
14:46 - 15:20	1.95	0.20	1.15	-	-	-
15:20 - 15:52	1.80	0.20	1.07	-	-	-
	L1b			L2b		
Segment [hh:mm]	Depth [m]	$H_{s,IG}$	$H_{s,INC}$	Depth [m]	$H_{s,IG}$	$H_{s,INC}$
January 5						
16:00 - 16:25	1.40	0.43	1.06	0.92	0.57	0.84
16:25 - 16:50	1.54	0.46	1.16	1.07	0.55	0.88
17:00 - 17:25	1.50	0.43	1.06	1.03	0.57	0.84
17:25 - 17:50	1.33	0.46	1.16	0.87	0.55	0.88

Table 3.2: Characteristic wave heights ($H_{s,IG}$ and $H_{s,INC}$) and characteristic swash heights (S_{IG} and S_{INC}) during the events in meters. Data when during low waterlevels when the pressure sensors ran dry have been removed.

Runup characteristics

The swash spectrum during the swash conditions in Figure D.2 shows a relatively even distribution between the energy in the IG band and the INC band, which is confirmed by the runup characteristic heights S_{INC} and S_{IG} in Table 3.3. In a further inspection, the runup characteristics have been compared to offshore wave parameters (H_0, $H_{0,eff}$, L_0), beach slope and Irribarren parameter. In this comparison, the wave setup on January 5th does not seem to be influenced by the changing conditions (see Figure 3.5). However, take into account that wave setup elevations are not direct measurements and have been calculated from the offshore conditions. The main interest in the comparison lies in the runup height $R_{2\%}$, since $R_{2\%}$ has been measured during collision conditions.

Segment [hh:mm]	$R_{2\%}[m]$	$\mu_{wave}[m]$	$S_{IG}[m]$	$S_{INC}[m]$
November 30				
10:18 - 10:51	1.21	0.33	0.84	0.60
10:51 - 11:24	1.24	0.33	0.86	0.64
11:24 - 11:57	1.15	0.32	0.75	0.60
11:57 - 12:31	1.02	0.31	0.75	0.51
12:31 - 13:04	1.00	0.29	0.76	0.45
13:04 - 13:37	0.86	0.24	0.67	0.32
December 1				
10:42 - 11:14	1.30	0.22	0.74	0.70
11:26 - 11:59	1.32	0.34	0.76	0.87
11:59 - 12:32	1.47	0.40	0.84	0.87
12:32 - 13:06	1.51	0.46	0.91	1.00
13:06 - 13:39	1.57	0.42	0.97	0.98
13:39 - 14:12	1.32	0.39	0.87	0.78
December 2				
12:33 - 13:06	1.09	0.28	0.77	0.59
13:06 - 13:40	1.17	0.26	0.82	0.72
13:40 - 14:13	1.09	0.28	0.76	0.67
14:13 - 14:46	1.11	0.37	0.66	0.49
14:46 - 15:20	0.80	0.23	0.55	0.29
15:20 - 15:52	0.86	0.41	0.52	0.26
January 5				
16:00 - 16:25	2.10	0.37	-	-
16:25 - 16:50	2.16	0.37	-	-
17:00 - 17:25	1.91	0.35	-	-
17:25 - 17:50	1.49	0.35	-	-

Table 3.3: Runup elevation and the runup characteristics of during swash and collision events events.

In a first comparison, the influence of the offshore wave height (H_0) and the effective offshore wave height ($H_{0,eff}$) is investigated. A slight improvement in the linear fit is found between the runup height and the effective offshore wave height (see Table 3.3. This was especially noticeable in S_{INC} and S_{IG} ($R^2 = 0.27$ and $R^2 = 0.26$ to $R^2 = 0.47$ and $R^2 = 0.76$). In a further investigation of the offshore and beach parameters, the effective offshore wave height has been used. The strongest relation is found between S_{IG} and $H_{0,eff}$, which is interesting since the relation between S_{IG} and H_0 show low correlation. In a further investigation of the offshore and beach parameters, the effective offshore wave height has been used.

When comparing the different beach slopes (β_f and β_d) we find a larger dependence between beach slope β_f and the runup $R_{2\%}$. This is also supported by the improved fit when using beach slope β_f to calculate the Irribarren number (ξ_f) ($R^2 = 0.31$ to $R^2 = 0.77$ for $R_{2\%}$). S_{IG} and μ_{wave} are found to be independent from beach slope from in this dataset, since no improvement was found when adding them to the comparison. These findings are supported by the studies Brinkkemper et al., 2013, Stock-

don et al., 2006 and Senechal et al., 2011. This implies that the majority of the swash height during collision conditions comes from incident wave spectrum, which is also confirmed by the findings from the pressure sensors.

Parameters that traditionally influence runup have also been analysed. These parameters include:

$$(H_{0,eff}L_0)^2$$
$$\beta_f(H_{0,eff}L_0)^2$$
$$\beta_d(H_{0,eff}L_0)^2$$

Of which the best fit for $R_{2\%}$ is found in $\beta_f(H_{0,eff}L_0)^2$, meaning a combination of beach slope (β_f) wave length and effective wave height shows a large correlation ($R^2 = 0.88$). However, the fit for μ_{wave} improved when using $\beta_f(H_{0,eff}L_0)^2$, although the improvement in the data was only minimal ($R^2 = 0.33$). The characteristic S_{INC}, which has only been gathered during swash conditions, showed and improved fit for β_f and $\beta_f(H_{0,eff}L_0)^2$ with a $R^2 = 0.89$ and $R^2 = 0.85$ respectively, meaning a high dependence of the beach slope. S_{IG} did not show this relation with beach slope. The IG swash height showed that it was mostly dependent on offshore effective wave height.

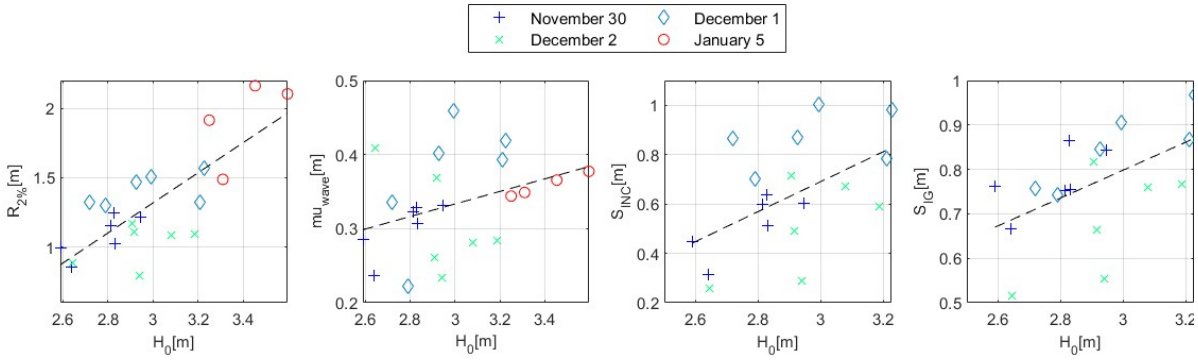

(a) Offshore wave height (H_0)

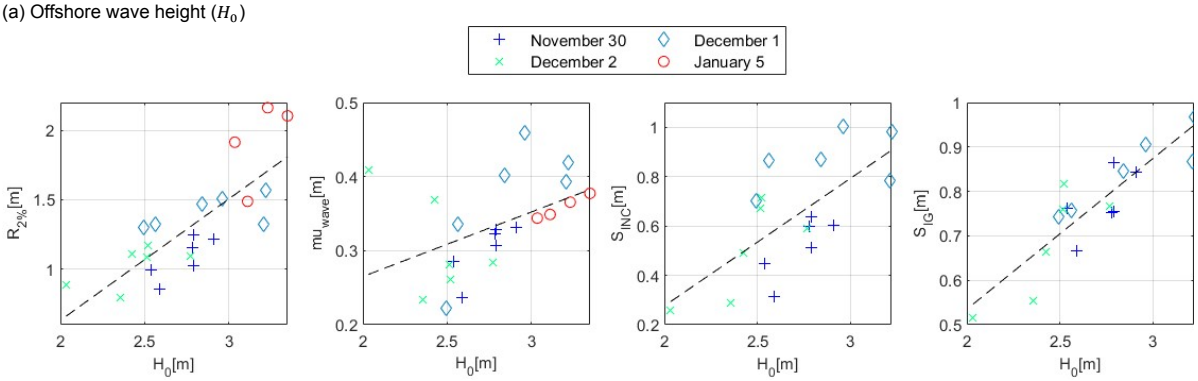

(b) Effective offshore wave height ($H_{0,eff}$)

Figure 3.5: The runup characteristics plotted against the offshore wave height and effective offshore wave height. An improvement in the linear fit is found in the effective offshore wave height. This improvement is mainly visible in S_{INC} and S_{IG}.

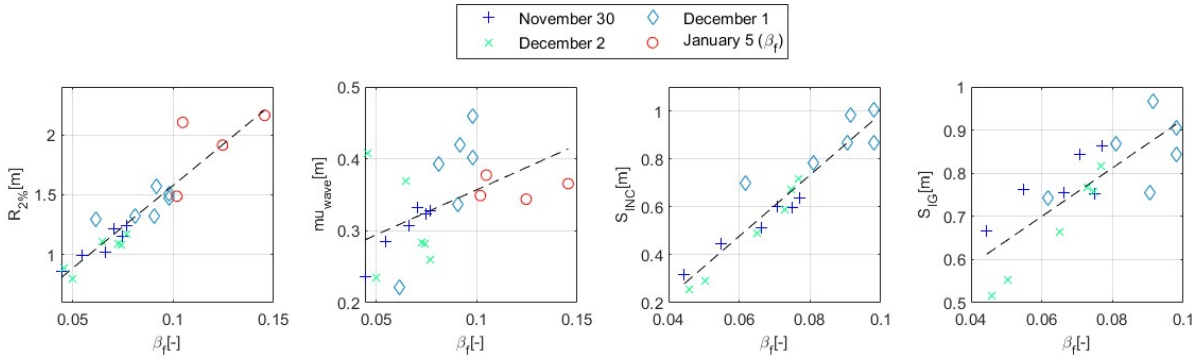

(a) Beach slope (β_f)

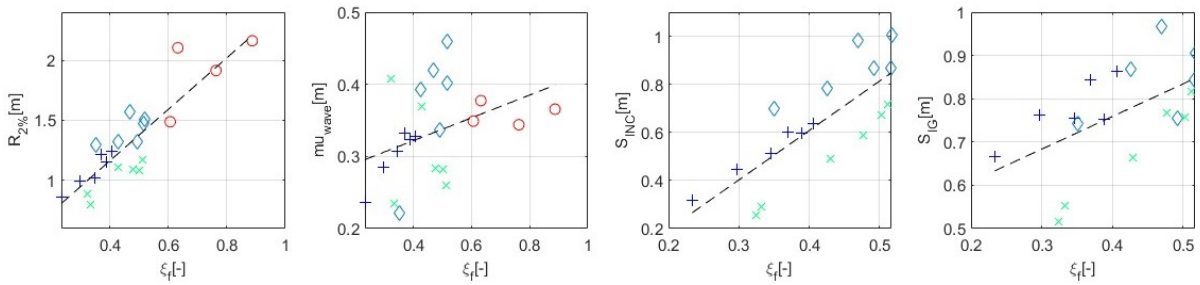

(b) Irribarren parameter (ξ_f)

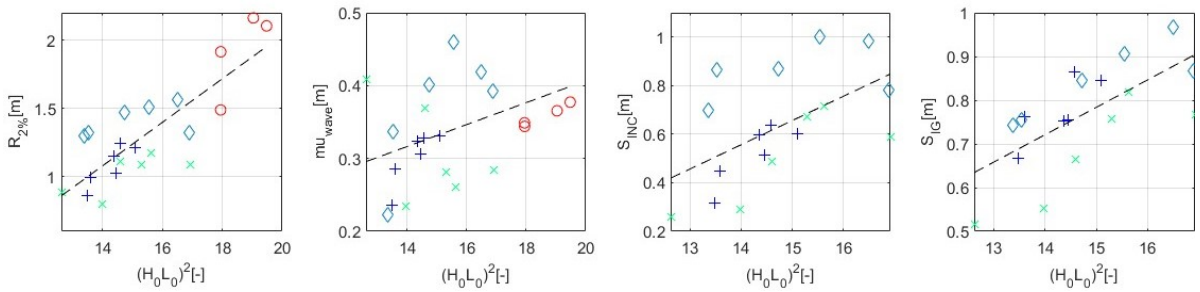

(c) Parameter ($(H_{0,eff}L_0)^2$)

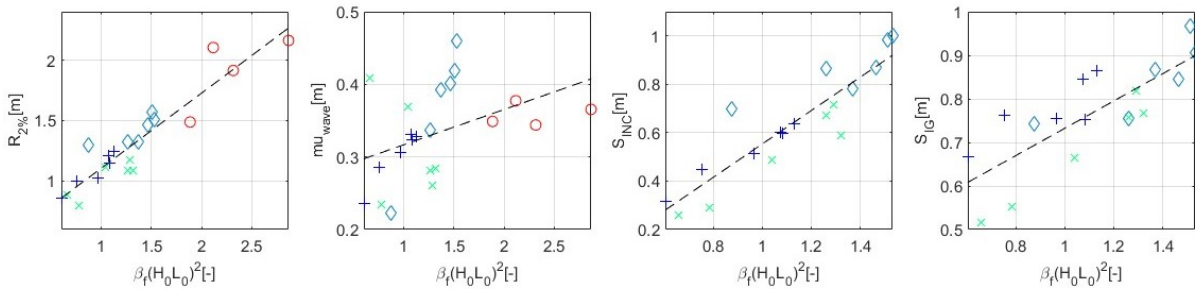

(d) Parameter ($\beta_f(H_{0,eff}L_0)^2$)

Figure 3.6: The runup characteristics plotted against the offshore wave parameters and beach parameters. The runup characteristics S_{INC} and S_{IG} could only be calculated during swash conditions.

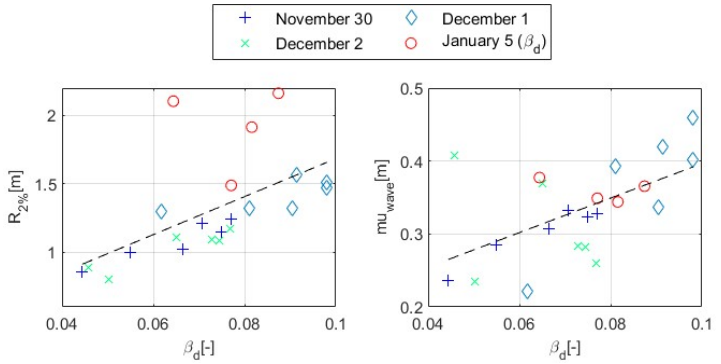

(a) Beach slope (β_d)

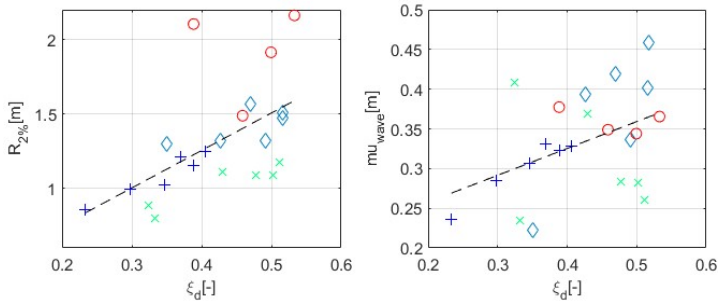

(b) Irribarren parameter (ξ_d)

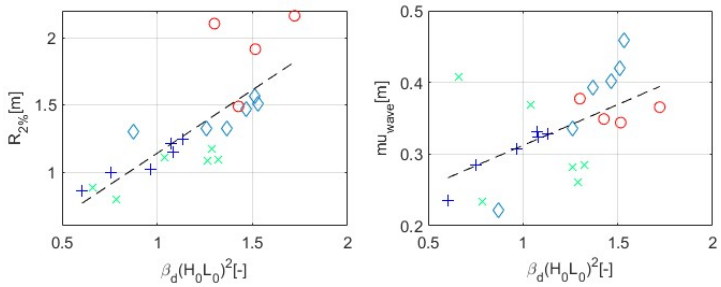

(c) Parameter ($\beta_d(H_{0,eff}L_0)^2$)

Figure 3.7: The runup characteristics plotted against the offshore wave parameters and beach parameters, while using beach slope $\beta_d f$, which excludes the dune slope into from calculation of the average beach slope. A linear trend is fitted to the comparison in order to find correlation between the runup characteristics and the wave and beach parameters.

Parameter	$RMSE[m]$	$R^2[-]$	$d[-]$	$RMSE[m]$	$R^2[-]$	$d[-]$
		$R_{2\%}$			μ_{wave}	
H_0	0.22	0.61	0.81	0.05	0.12	0.27
$H_{0,eff}$	0.22	0.61	0.79	0.05	0.20	0.27
β_d	0.29	0.33	0.42	0.32	0.05	0.44
β_f	0.13	0.86	0.94	0.05	0.23	0.28
ξ_d	0.29	0.31	0.46	0.05	0.19	0.27
ξ_f	0.17	0.77	0.90	0.05	0.14	0.15
$(H_{0,eff}L_0)^{1/2}$	0.20	0.67	0.84	0.05	0.11	0.13
$\beta_d(H_{0,eff}L_0)^{1/2}$	0.22	0.62	0.77	0.05	0.33	0.44
$\beta_f(H_{0,eff}L_0)^{1/2}$	0.12	0.88	0.95	0.05	0.19	0.24

Table 3.4: $RMSE$, R^2 and Willmott's d between the trend in the data from Figures 3.5, 3.6 and 3.7 and $R_{2\%}$ and μ_{wave}.

Parameter	$RMSE[m]$	$R^2[-]$	$d[-]$	$RMSE[m]$	$R^2[-]$	$d[-]$
	S_{INC}			S_{IG}		
H_0	0.18	0.27	0.39	0.09	0.27	0.45
$H_{0,eff}$	0.15	0.47	0.62	0.05	0.76	0.85
β_f	0.06	0.89	0.94	0.06	0.64	0.76
ξ_f	0.13	0.62	0.75	0.09	0.31	0.42
$(H_{0,eff}L_0)^{1/2}$	0.18	0.31	0.40	0.08	0.45	0.60
$\beta_f(H_{0,eff}L_0)^{1/2}$	0.08	0.85	0.91	0.05	0.71	0.82

Table 3.5: $RMSE$, R^2 and Willmott's d between the trend in the data from Figures 3.5, 3.6 and 3.7 and S_{INC} and S_{IG}.

3.3. Comparison of Stockdons equation to measured wave runup

The predicted runup heights ($R_{2\%,O}$, using Stockdon et al., 2006) calculated from the offshore conditions are compared to the observed runup heights ($R_{2\%,O}$) from the runup camera and LiDAR. In the calculation of $R_{2\%,O}$, the effective offshore wave height ($H_{0,eff}$) is used. From these effective offshore wave heights, the predicted runup height can be estimated using the Equation 1.7. The effective wave heights, computed runup heights by the Stockdon equation and the observed runup heights ($R_{2\%,O}$) from the runup camera and LiDAR have been added to Table 3.6 for a direct comparison between the two variables.

Segment [hh:mm]	$H_{0,eff}[m]$	$R_{2\%,P}$	$R_{2\%,O}$
November 30			
10:18 - 10:51	2.91	1.10	1.21
10:51 - 11:24	2.79	1.12	1.24
11:24 - 11:57	2.78	1.09	1.15
11:57 - 12:31	2.79	1.02	1.02
12:31 - 13:04	2.54	0.86	1.00
13:04 - 13:37	2.59	0.77	0.86
December 1			
10:42 - 11:14	2.49	0.95	1.30
11:26 - 11:59	2.56	1.20	1.32
11:59 - 12:32	2.84	1.36	1.47
12:32 - 13:06	2.96	1.42	1.51
13:06 - 13:39	3.22	1.43	1.57
13:39 - 14:12	3.21	1.34	1.32
December 2			
12:33 - 13:06	2.42	1.34	1.09
13:06 - 13:40	2.36	1.28	1.17
13:40 - 14:13	2.39	1.27	1.09
14:13 - 14:46	2.49	1.10	1.11
14:46 - 15:20	2.59	0.93	0.80
15:20 - 15:52	2.47	0.82	0.89
January 5			
16:00 - 16:25	2.61	1.69/2.51	2.48
16:25 - 16:50	2.56	1.65/2.07	2.28

Table 3.6: A comparison between the observed runup heights from the runup camera and LiDAR scanner and the predicted runup heights from Stockdon's equation. The predicted runup heights on January 5th have two values. The left one indicates only the beach slope is used and the right one indicates the beach and dune slope are used.

In order to create a clear comparison between the predicted runup from Equatuion 1.7 and the measured runup during the events, the two values are directily compared in Figure 3.8. In this Figure is becomes clear that the runup elevations dusing swash conditions are generally well estimated by Stockdon's formula, but the runup values during collision conditions are underestimated quite significantly.

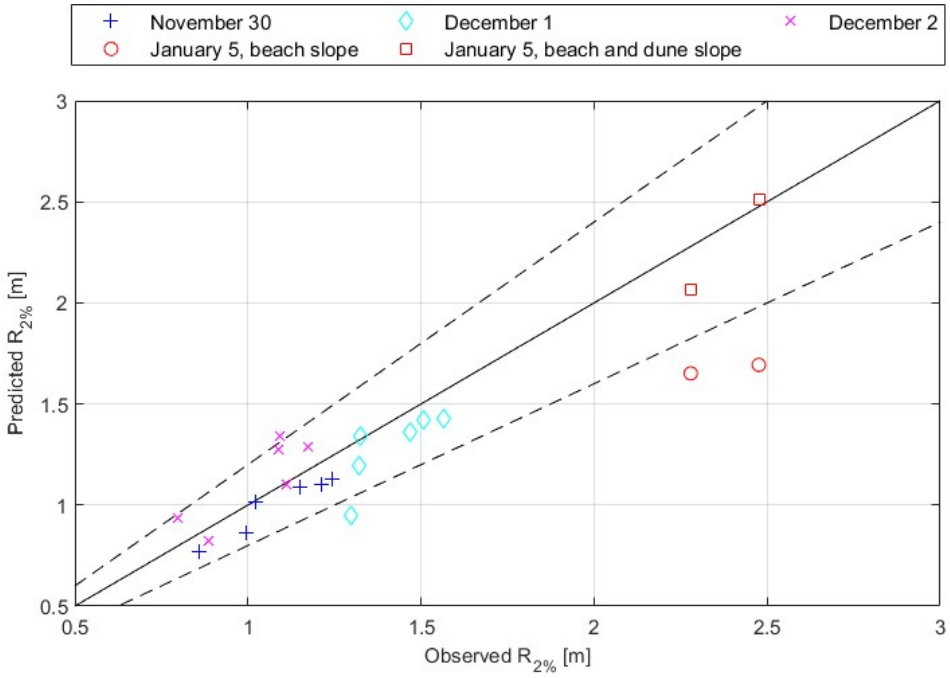

Figure 3.8: The predicted runup levels from Stockdon et al., 2006 and the observed runup levels from the runup camera and LiDAR are plotted against each other. The dashed lines indicate the 80% confidence bounds estimated by Stockdon et al., 2006

.

In order to create a clear indication of the disparity between the different conditions, $RMSE$, R^2 and Willmott's d (see Equations 2.28, 2.29 and 2.30) are calculated from the predicted and measured runup values (see Table 3.6). From Figure 3.8 and Table 3.7 it becomes clear that the Stockdon's equation predicts the runup during swash conditions relatively well. The estimated deviation from Equation 1.7 is $\%Error_{R_{2\%}} = 20\%$ (Stockdon et al., 2006).

$RMSE[cm]$	$R^2[-]$	$d[-]$
swash conditions		
14	0.55	0.99
collision conditions beach slope		
71	-	0.61
collision conditions beach and dune slope		
15	-	0.89

Table 3.7: $RMSE$, R^2 and Willmott's d between the observed runup elevations during swash conditions and collision conditions and the predicted runup values from the Stockdon Equation (see Equation 1.7). R^2 coefficients have been left out during collision conditions due to it being nonsensical data, which is most likely caused by the low amount of data points.

The comparison between the observations and predictions during swash conditions in this study are within the predicted errors, and the collision conditions are predicted accurately when the dune slope is incorporated in the derivation of the average beach slope.

4

Discussion

Final results from the data analysis are discussed in this chapter with the aim to giving a final verdict on the research questions of this master thesis. A discussion is held on the validity and range of applicability of these results. Any recommendations for subsequent research have also been made, which have been added to Chapter 6. During this master thesis, the topics in the list below have been followed.

1. **Fieldwork experiment:** In field measurements have been performed over the span of 6 weeks, during which offshore and nearshore coastal conditions have been monitored with the intend of, nor only capturing swash conditions, but also collision conditions.
2. **Data processing:** Data from the fieldwork project has been collected and processed.
3. **Data analysis:** Processed data has been analysed and the coastal behaviour has been determined from the dataset.

The ideas behind the setup and processing techniques mentioned above, as well as their uncertainties and limitations are elaborated upon in this chapter.

4.1. Fieldwork experiment

During the fieldwork experiment, that from the start of November to halfway December, offshore and nearshore hydrodynamic conditions have been measured. The deployed instruments have performed as expected. However, due to the placement, only high tide conditions have been measured with the runup camera and LiDAR scanner. Thus, beach characteristics during low tide conditions are unknown.

The runup camera could only measure in conditions with high visibility. Since the Fieldwork Experiment took place during winter, sunlight durations were short. This made it hard to find a window of opportunity to capture an entire high tide event using the runup camera.

During the Fieldwork Experiment two collision events have been captured, however, only one of these events has been evaluated. During the first collision event, the LiDAR scanner has moved in an unknown manner, which would decrease the accuracy of the results stemming from the LiDAR significantly. For this reason, another deployment has been made on January 5^{th} in order to capture storm conditions. During these conditions, the location of the pressure sensors has changed compared to the original fieldwork experiment. This has reduce the comparability between the pressure sensors between the January event and the events from November to halfway December.

4.2. Data processing

Data collection and processing can be described in five steps:

1. Collection of the offshore hydrodynamics.

2. The changes in the beach characteristics and the morphological changes during the events.

3. Transformation of the raw dataset (pressure, point cloud and images) to waterlevel elevation ($z(t)$) and total waterline elevation ($h(t)$).

4. Extraction of characteristic wave heights (H_{IG}, H_{INC}, S_{IG} and S_{IG}) from waterlevel elevation.

5. The extraction of the runup elevations ($R_{2\%}$) and setup levels (μ_{total} and μ_{wave}) form the total waterline elevation ($h(t)$).

1. Collection of the offshore hydrodynamics
Data from offshore stations, which measured the incoming wave in setup conditions during the Fieldwork Experiment, have been simplified. Firsly, since the offshore station measuring wave height and wave period is located quite far from the fieldwork site, slightly different offshore wave conditions could be causing the nearshore conditions at the Fieldwork Site. This could be due to time lag between the waves moving from the offshore station towards the Fieldwork site, and due to the wave field located at the offshore station moving in a different direction than the Fieldwork site. Secondly, offshore wave heights have been corrected with respect to the waterline using the refraction coefficient (K_R). This simplifies the dataset, but neglects the influence of cross shore conditions that could play a role in runup behaviour. Thirdly, as for the offshore tidal stations, the averaging technique between the stations cause inaccuracies in the dataset.

2. The changes in the beach characteristics and the morphological changes during the events
Since morphological changes during swash conditions are small, these have been neglected, which is relevant for runup camera processing and the beach slope calculations. However, this simplification can be made since the largest morphological change change measured during a high water event is $7cm$, but over all the morphological change was below $3cm$ (see Figure 2.37).

The average coastal slope during each event is calculated using Equation 2.14. The beach slope during collision conditions is highly sensitive to the location of the mean total waterline level (h_{mean}), since the upper bound (h_{upper}) will be located on the duneface. A slight difference in h_{mean} will have a significant effect on the calculated average coastal slope (see Section 2.5).

The amount of slumping during the collision conditions could have had a temporary effect on the runup characteristics. Slumps occurred in intervals of around 5 to 10 minutes. This changed the beach slope around/above the dune toe, which could have resulted in the a change in the runup characteristics during the collision conditions.

3. Transformation of the raw dataset (pressure, point cloud and images) to water level elevation and total waterline elevation

Runup time stacks
Images from the runup camera have been manually processed by selecting the waterline elevations from the time-stacked images. This manual selection could have resulted in unexpected errors in the location of the waterline. The assumption of constant morphology in during a swash event could also result in inaccuracies, although these are expected to stay within $3cm$.

In order to visually create the best fit, a spline method has been used to interpolate between the manually selected points in the time stacks. This spline method causes rounding of the sharp changes in $h(t)$ and could have affected the high frequency part of the variance density spectrum during swash conditions. A comparison is made between the the spline interpolation method and a linear interpolation (see Figure 4.1).

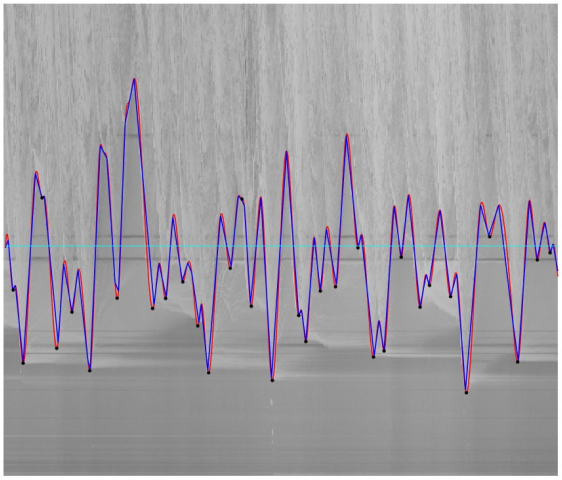

Figure 4.1: A comparison between the spline interpolation method and the linear interpolation method in the time stack during a segment of November 30th, at 11:24 - 11:57. The red line shows the spline interpolation method and the blue line the linear interpolation method. The spline interpolation rounds off the edges of the tracked waterline, while the linear interpolation causes sharp edges.

The interpolation method mainly seems to have an effect on the variance density spectrum calculated the data (see Figure 4.2). The higher frequencies (above $0.025Hz$) showed lower energy within the spectrum of the linear interpolation method than the spline method. This can be explained by the fact that the spline method has rounded edged around the peaks of the waterline. The amplitude next to the peaks is higher with the spline interpolation method. This means there will be more energy within the data from which uses the spline interpolation method. The runup height between the interpolation methods changed $0.03cm$ (see Figure 4.2, whit the higher being from the spline interpolation method. The rounding of the edges could have led to a slight increase of the $R_{2\%}$ value, but this difference is only minor.

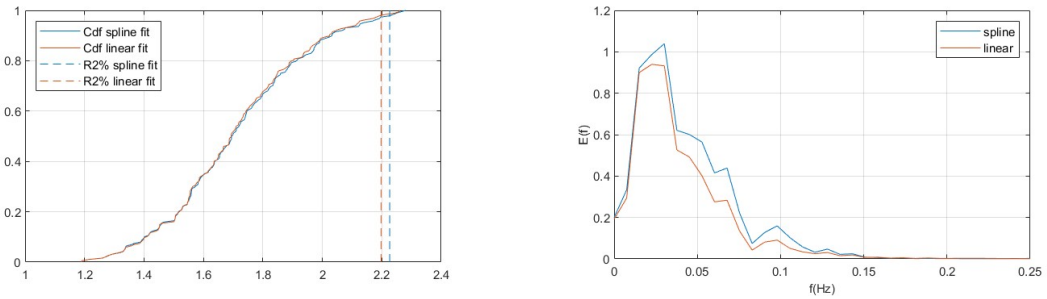

(a) Distribution of runup elevations

(b) Spectrum

Figure 4.2: The difference between the runup height and spectral distribution between spline interpolation (red) and linear interpolation (blue) during a segment of November 30th, at 11:24 - 11:57.

LLC LiDAR alignment

Estimating the correct position and orientation of the LLC LiDAR is crucial. Small errors in the alignment, and especially the orientation of the LLC LiDAR can lead to large errors in the point cloud of the morphology and hydrodynamics. The difference the incorrect positioning and alignment of the LiDAR scanner can have a translatory effect on the complete water level time series. The location of the LiDAR scanner has been determined by a RTK-GPS. In the data of the January 5th event, the LLC LiDAR orientation has a heading of $\theta_{heading} = 287°$ relative to true North, a pitch of $\theta_{pitch} = 53°$ and a roll of $\theta_{roll} = -7°$ (see Figure 2.27).

The standard deviations in these orientations are, in the same order $\sigma_{heading} = 1.4°$, $\sigma_{pitch} = 1.2°$

and $\sigma_{roll} = 2.5°$. Of these orientation errors, the pitch error has the highest influence in the over all transect. An error in the pitch orientation directly translates to an error in the elevation of the cross shore point cloud. The other orientation errors have less of an effect on the cross shore elevation. Taking the location of the dune toe as an example, the error in the pitch orientation gives a local standard deviation at the dune to of $\sigma_z = 0.05[m]$ in elevation and $\sigma_l = 0.03m$ in cross shore location.

4. Extraction of characteristic wave heights from water level elevation
The water levels and have been transformed to variance density spectra in order to extract the characteristic wave heights. In the calculations of the characteristics wave heights it is important to attribute the correct interpolation ranges between for the IG and INC band. The cutoff between the INC band and IG band has been determined by locating the lowest trough in the spectrum in between $0.03Hz$ and $0.07Hz$. The location of the cutoff between IG and INC seems to be correct looking at the wave spectra, however during the event on December 2nd this cutoff frequency is low compared to the other reported cutoff frequencies (0.037 compared to $0.050 - 0.058$). A possible causes for this could be the larger wave periods reported on December 2nd compared to the November 30th and December 1st which could also have resulted in the lowering of the cutoff frequency. However, during January 5th the wave periods were larger than during December 2nd and did not result in the lowering of the frequency cutoff. Another possibility could be the increase in offshore wave angle (α_0), since this was reported to be the highest during December 2nd. Alongshore effects could have played a role in the distribution of the IG and INC wave energy, but this is not certain.

5. The extraction of the runup elevations and total setup levels from the total waterline elevation
Since the total water elevation during collision conditions is incomplete, assumptions were needed to be made in order to extract $R_{2\%}$ and μ_{wave}. In order to extract $R_{2\%}$, the missing amount of runup excursions are estimated. The number of zero down crossings at pressure sensor at location L2b have been used to calculate the amount of waves present at the pressure sensor during each segment. The amount of waves at location L2b are compared to the amount of runup excursions measured by the LLC LiDAR. The comparison is supposed to show the missing amount of waves during each segment, however, bore bore merging could affect this comparison. When bore bore merging takes place between the , the missing amount of runup events could be over-estimated. This would result in a lower amount of waves missing from the runup distributions, which could result in an over estimation of the percentage of missing waves. Thus the actual runup height $R_{2\%}$ would likely be slightly higher than the one presented in this paper.

The wave setup during collision conditions is another parameter for which estimation needed due to the fact that the total water level motion could not be captured. The estimation will cause uncertainties in the location of the wave setup level during collision conditions. The wave setup is derived using Equation 2.24, in which γ empirically derived from Battjes and Stive, 1985. This should suffice, however, the exact error of the breaker index during the conditions in this fieldwork experiment is unknown.

4.3. Data analysis
The following topics have been analysed.

1. The use of a LiDAR scanner to measure shallow water hydrodynamic conditions.
2. The impact of the changing storm regimes to the runup characteristics.
3. The ability of the Stockdon equation in predicting runup elevations during swash and collision conditions.

1. Capturing hydrodynamic conditions with the LLC LiDAR
Since the LLC LiDAR is a new instrument used during coastal fieldwork deployments, data from the LLC LiDAR is evaluated in terms of effectiveness of measuring hydrodynamic and morphological conditions. Possible causes for inaccuracies in the LLC LiDAR datasets can be summarized into three

causes, which are positioning errors, instrument errors and processing errors. In order to evaluate the effectiveness of the LLC LiDAR in measuring the total water level, two methods have been used. Firstly, the accuracy in the position and orientation of the LLC LiDAR dataset is estimated. Secondly, the dataset of the LLC LiDAR is compared to pressure sensor data. Thirdly, the differences in the difference in the errors between the instruments is analysed.

A first reason behind the errors between the pressure sensor and the LLC LiDAR could be the alignment errors of the LLC LiDAR, which could have led to errors in the order $\sigma_z = 0.05[m]$ in elevation and $\sigma_l = 0.03m$ in cross shore location. These errors would however be of minor influence, since in Figure 3.1 it is visible that the pressure sensor data is too high in the troughs of the data and too low in the peaks of the data. Thus this would not be the only influence of the errors between the two datasets.

A second reason behind the differences between the pressure sensor and LLC LiDAR datasets could come from spreay being measured by the LLC LiDAR. This is mainly indicated by the differences in the peak elevations between the datasets. The LLC LiDAR scans the surface of the water, while the pressure sensor measures the water level pressure above the instrument. Due to the different methods, the differences could be attributed to the spray or foam present in the surge events. From these arguments it could be argued that the LLC LiDAR could have difficulties dealing with spray during high energy events. This could be negated by filtering or smoothing the LLC LiDAR data, which could improve the fit between the data of the two instruments. This

Lastly, data quality from the LLC LiDAR worsened the longer the experiment endured. There is a difference in R^2 between the first two segments ($R^2 = 0.78 - 0.86$) of the comparison between the LLC LiDAR and the last two segments ($R^2 = 0.61 - 0.74$). The first two segments (16:00 - 16:50) did not see an average cross shore bin size of below 1.8 (see Figure 2.31). However, in the last two segments (17:00 - 17:50) the average cross shore bin size dropped below one in multiple cross shore bins (see Figure 4.3). Interpolation has been used between the missing grid points, which could lead to errors in the LLC LiDAR datasets.

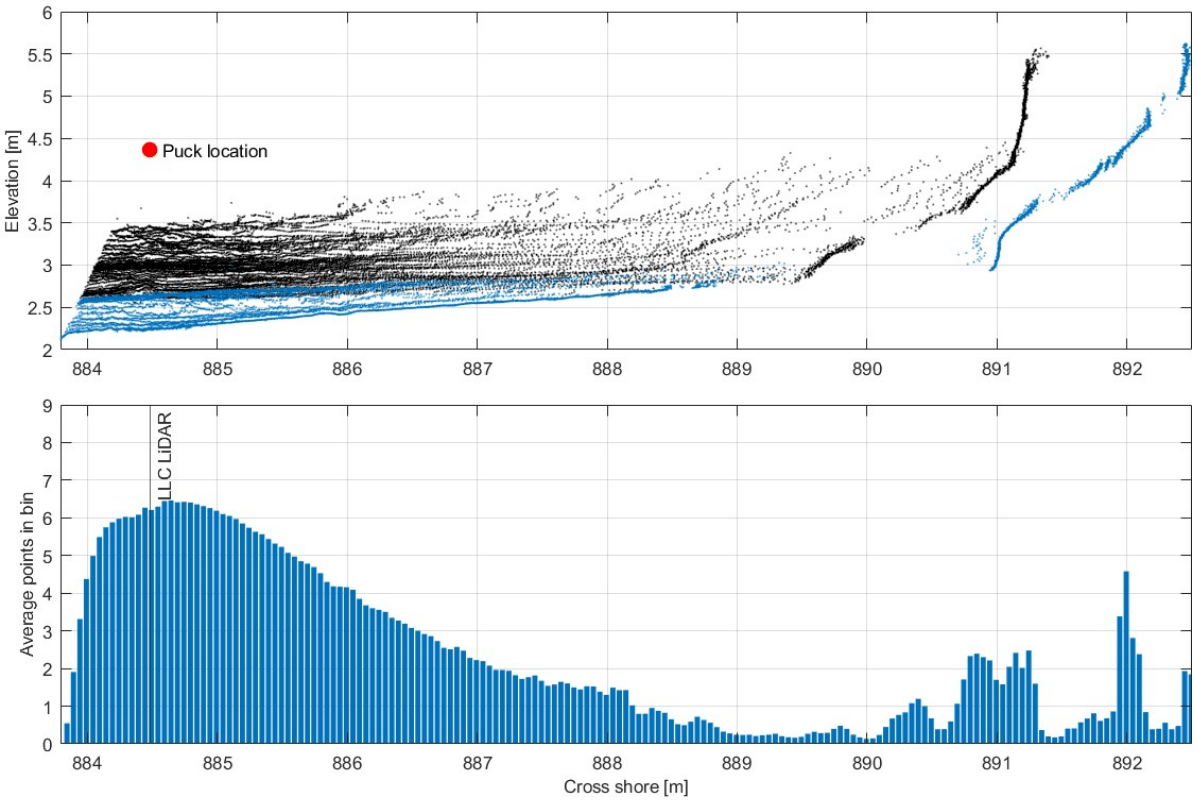

Figure 4.3: Top figure shows the LLC LiDAR point cloud of the first 45 seconds in black, and the last 45 seconds of the point cloud in blue during during 17:00 to 17:50 UTC+1. The bottom figure shows the number of points in cross shore direction of the the grid of the LLC LiDAR point cloud with $dx = 15cm$ and $dt = 0.2s$ during the same time range. The vertical line and text in the plot indicate the cross shore position of the LLC LiDAR. In total, there are a 189 bins in cross shore direction.

2. The impact of the changing storm regimes to the runup characteristics

The amount of wave dissipation during both conditions is compared by looking at the ratio of H_{INC}/H_{IG} at certain cross shore distances from the total setup level. In Section 1.2, it was suggested that at dissipative coasts, high energy dissipation takes place in the INC band of the wave spectrum. This means reflective beaches are dominated by IG band energy and reflective beaches by INC band wave energy, since the incoming wave field generally has more energy in the INC band than the IG band. During the events analysed in this experiment, the energy just before the swash zone was comparable in both spectral bands, since the ratio of $H_{INC}/H_{IG} = 1.43$ during swash conditions. During collision conditions the ratio of $H_{INC}/H_{IG} = 1.63$ was observed. Although the energy during the collision conditions was higher, we can conclude that the characteristics of the beach performed generally the same during both conditions. Davidson-Arnott et al., 2019, showed that wave dissipation is mainly related to the water level depth and breaker type and Irribarren number. Wave data from Fieldwork Experiment showed an intermediate beach state when looking at the nearshore wave field for both the collision conditions and swash conditions, since neither the INC band energy or IG band energy can be neglected during all events analysed in this research.

In a further analysis, the runup elevations during collision conditions showed an increase in runup elevation compared to swash conditions. This can mainly be explained by the increase in offshore wave height ($R^2 = 0.61$), but also by an increase in beach slope β_f ($R^2 = 0.86$ and see Figure 3.6). This suggest that the interaction with the dune face has a significant influence of the runup height, since the fit of beach slope B_f, which includes the dune face, is much better than the fit for the beach slope B_d. Since the wave field during the collision and swash conditions are quite similar, this suggests that the wave dissipation during collision conditions show the same characteristics as the swash conditions until the waves reach the dune toe. Waves that interact with the dune face will likely behave more like waves with a higher Irribarren number than waves which do not reach the dune toe. This is also

suggested by the improved fit of the Irribarren number ξ_f ($R^2 = 0.77$) compared to ξ_d ($R^2 = 0.31$). However, the assumption for average beach slope over the dune and beach seems artificial. It would likely be better to dissect the nearshore coastal system into a beach section and a dune face section. For example, runup in the beach section would have a dissipative behaviour and runup in the dune face section would act reflective. An investigation into the variance spectra of swash during collision conditions could provide more insight into the behaviour of runup during collision conditions. This could also where the increase in runup height actually comes from.

Additionally, runup height also showed to be slightly dependent on offshore wave length, due to the improvement in the fit when wave length was included ($(H_{0,eff}L_0)^{1/2}$ was $R^2 = 0.77$). This has aslo been shown in the study by Stockdon et al., 2006. This improvement was also seen in the runup characteristics S_{INC} and S_{IG} during the swash conditions, which both seem to be partially dependent on L_0 (see Table 3.5.

S_{IG} showed a significant improvement in the dependence to offshore wave height when refraction was taken into account (see Table 3.5. This improvement was also found in the characteristic S_{IG}, but slightly smaller. During the Fieldwork Experiment, the refraction during December 2nd was quite significant ($K_r = 0.77 - 0.87$). The refraction correction resulted in an improvement of the data, which means it could be possible that refraction should be taken into account when using empirical runup formula's like the equation from Stockdon et al., 2006.

Concluding, the increase in runup could result from an increase of energy in the INC band of the swash spectrum. However, since the swash spectrum could not obtained from the data processed data, the exact increase of energy in the INC band or IG band remains unknown. Until the full runup and run-down is measured during collision conditions, the behaviour of the runup characteristics remains unknown. A dependence on beach slope β_f does suggest an increase of energy in the INC band is present during collision conditions, but the derivation of β_f seems artificial in nature, and a better parameter describing the behaviour of the interaction of runup with the dune face needs to be found.

3. Evaluation of Stockdon for predicting runup elevations during swash and collision conditions
The runup height calculated using the Stockdon equation follow the measured runup elevations from the runup camera and the LiDAR within the expected error bounds. for the swash conditions this is to be expected, but during the collision conditions the ability of the Stockdon equation to predict runup levels during needed to be analysed. In this comparison, a correct definition of the beach/coastal slope played a mayor role. The difference between the predicted values of the Stockdon equation and the observed values during the collision conditions is values is quite high when only the beach slope is used. A reason causing the difference could be a wrong assessment of the beach slope (β_f). In Section 2.5, the beach slope during the collision event has been taken from the dune toe downward, which is is most likely a wrong assessment looking at the comparison. When the beach slope for the collision conditions is calculated in the same manner as during the swash conditions (from using the average slope between $h \pm R_{2\%}/1.55$, see Section 2.5), $R_{2\%,P}$, increases to $2.51[m]$ and $2.07[m]$, which is comparable to the observed runup heights. From these observations is clear that runup is highly sensitive to the beach slope, and a correct derivation of the beach slope is necessary to come to an accurate runup prediction using the Stockdon Equation.

5

Conclusion

The aim of this research is to improve the understanding of the implications to changing storm regimes (swash and collision) to the runup behaviour. Several coastal parameters have been looked at in order to determine any relation between runup and offshore hydrodynamics and beach conditions during both regimes. In order to gather more information about the runup conditions during collision conditions, a LLC LiDAR system has been used. This system has been tested in terms of its effectiveness of measuring hydrodynamic conditions. The runup elevations have also been compared to Stockdon's empirical equation for predicting runup.

5.1. LLC LiDAR evaluation

In order to determine the hydrodynamic conditions at the waterline, use has been made of a LLC LiDAR scanner, which is a state of the art measuring device measuring the water level elevation. In order to determine the accuracy of the scanner, the LiDAR has been compared to a pressure sensor located within the transect measured by the scanner. The water level elevation measured by both devices is seems to be similar, with a correlation of $R^2 = 0.61$ to $R^2 = 0.86$. However, in the peaks of the datasets, there is a higher difference between the devices ($R^2 = 0.34$ to $R^2 = 0.78$). The most likely causes for this difference are likely the water spray measured by the LLC LiDAR, which could lead to higher measurements in the LLC LiDAR data compared to the pressure sensor, and the alignment errors of the LLC LiDAR data, which could lead to errors in the order of $5cm$ and the conversion errors in the pressure signal to water level. The conversion errors arise from the the hydrostatic conversion of the pressure signal, and the fact that the pressure sensor was buried during the measurements.

5.2. Runup behaviour during collision conditions

During all events measured in this research, runup follows a normal distribution on the beach. Even during collision conditions still seems to follow a normal shaped distribution, meaning no difference is visible in the runup distribution due to the sudden steepening of the coastal profile.

Runup heights increased during collision conditions, which is caused by an increase of the offshore significant wave height, but likely also by the interaction with the dune face, which is expected to lower the dissipation in the runup event. In the data from the fieldwork experiment, a linear relation between average beach slope (B_f) and $R_{2\%}$ runup has been found. In this comparison, the average coastal slope is derived in between the total setup level (μ_{total}) and two standard deviations of the total water-line fluctuations ($R_{2\%}/1.55$). The beach slope (B_d, until the dune toe) alone does not seem to have any relationship with the wave runup. In order for a better representation of the beach characteristics during the collision conditions, the Irribarren parameter should be computed using the beach slope (B_f), since this will result in a better fit from the data in this research.

The runup height increase during collision conditions could result from more INC band energy will reaching the waterline. This could be caused by waves reaching the dune toe behaving like surging waves, which is a likely casue for an increase in runup height. Observations of the nearshore wave

field during collision conditions show an equal distribution in energy in the INC band and the IG band close to the swash zone during both swash and collision conditions. The interaction with the dune face will cause the runup height to be influenced more by INC band energy, since a larger portion of the energy in the incident wave band can travel all the way to the dune toe. The behaviour during collision conditions is close to that of intermediate coastal conditions described by Ruggiero et al., 2004. Neither the IG waves nor INC waves can be neglected near the dune toe during the collision conditions.

5.3. Validity of Stockdon Equation during collision conditions

When comparing the measured runup elevations by the runup camera and the LLC LiDAR to the Stockdon Equation (see Equation 1.7), it is confirmed that the Stockdon Equation is still valid when used during collision conditions. The one caveat however, is the determination of the coastal slope, which will be more difficult since the location of the waterline needs to be quite precise when using Equation 2.14.

Conclusively, the changing conditions cause an increase in runup elevations due to the lower dissipation during collision conditions. Due to this change in coastal behaviour, higher water levels will not only cause a linear increase in runup levels due to the changing water level, but will also allow for reduced dissipation when the storm regime changes from swash to collision conditions.

6

Recommendations

Since limited amounts of data are available during storm conditions, subsequent research will need to prove the findings presented in this report. Only one hour of data during one storm will not prove sufficient in providing conclusive results. However, it does provide an indication of the possible changes in the beach characteristics and hydrodynamic conditions.

The waterline measurements obtained during collision conditions are incomplete, which has lead to assumptions. In an ideal world, the entire total water level elevation was captured. Since the LLC LiDAR used in this experiment only has a range of $8m$, the use of one LLC LiDAR will not be able to capture the complete runup and run down of the swash motions. A solution could be to place several LLC LiDAR's at different cross shore location in the transect. The scanners should have overlapping FOV in order to be sure the entire swash motions are being captured.

Runup cameras can only operate during the day since they are a video based instrument. This has lead to difficulties in the operation of the instrument during the Fieldwork Experiment since winter time allowed for limited time the instrument could be used. It is recommended that an instrument other than a runup camera is used during winter which is able to operate in the dark. The LLC LiDAR could be an option in this regard.

During this research, alongshore motions are disregarded, however coastal characteristics have been reported that could be explained by alongshore hydrodynamic effects. A future research goal could be the effect of the angle of incidence to the distribution of energy in the IG band and INC band.

It seems that the interaction of runup with the dune face has an effect on the runup elevation. An idea could be that the distance of the mean water level/setup level to the dune toe could pose as a parameter which describes the behaviour of the runup in the transition from swash conditions to collision conditions. however, this has to be researched further. This could be ideally tested in a situation with an irregular wave field where the water level rises slowly. The investigation would mainly be in the transition of the runup not reaching the dune toe to where the runup height does reach the dune toe.

Bibliography

Asbury H. Sallenger, J. (2000). Storm impact scale for barrier islands. *Journal of Coastal Research*, *16*(3), 890–895. http://www.jstor.org/stable/4300099

Battjes, J. (1974). Surf similarity. *Coastal Engineering Proceedings*, *1*(14), 26. https://doi.org/10.9753/icce.v14.26

Battjes, J., Bakkenes, H., Janssen, T., & van Dongeren, A. (2004). Shoaling of subharmonic gravity waves [doi: 10.1029/2003JC001863]. *Journal Of Geophysical Research-Oceans*, *109*(C02009), 1–15. https://doi.org/doi:10.1029/2003JC001863

Battjes, J., & Stive, M. (1985). Calibration and verification of a dissipation model for random breaking waves. *Journal of Geophysical Research 90(C5), 9159-9167. (1985)*, *90*. https://doi.org/10.1029/JC090iC05p09159

Bertin, X., de Bakker, A., van Dongeren, A., Coco, G., André, G., Ardhuin, F., Bonneton, P., Bouchette, F., Castelle, B., Crawford, W. C., Davidson, M., Deen, M., Dodet, G., Guérin, T., Inch, K., Leckler, F., McCall, R., Muller, H., Olabarrieta, M., … Tissier, M. (2018). Infragravity waves: From driving mechanisms to impacts. *Earth-Science Reviews*, *177*, 774–799. https://doi.org/https://doi.org/10.1016/j.earscirev.2018.01.002

Brinkkemper, J., Torres-Freyermuth, A., Mendoza, E., & Ruessink, G. (2013). Parameterization of wave run-up on beaches in yucatan, mexico: A numerical study. *Coast. Dynam.*, 225–234.

Clifton, H. E. (2005). Shoreface. In M. L. Schwartz (Ed.), *Encyclopedia of coastal science* (pp. 877–881). Springer Netherlands. https://doi.org/10.1007/1-4020-3880-1_290

Davidson-Arnott, R., Bauer, B., & Houser, C. (2019). *Introduction to coastal processes and geomorphology* (2nd ed.). Cambridge University Press. https://doi.org/10.1017/9781108546126

de Beer, A., McCall, R., Long, J., Tissier, M., & Reniers, A. (2021). Simulating wave runup on an intermediate–reflective beach using a wave-resolving and a wave-averaged version of xbeach. *Coastal Engineering*, *163*, 103788. https://doi.org/https://doi.org/10.1016/j.coastaleng.2020.103788

Dean, R. G. (1973). Heuristic models of sand transport in the surf zone.

Elfrink, B., & Baldock, T. (2002). Hydrodynamics and sediment transport in the swash zone: A review and perspectives. *Coastal Engineering*, *45*, 149–167. https://doi.org/10.1016/S0378-3839(02)00032-7

Goda, Y. (2000). *Random seas and design of maritime structures* (2nd). WORLD SCIENTIFIC. https://doi.org/10.1142/3587

Guedes, R. M. C., Bryan, K. R., & Coco, G. (2013). Observations of wave energy fluxes and swash motions on a low□sloping, dissipative beach. *Journal of Geophysical Research*, *118*, 3651–3669.

Guo, J. (2002). Simple and explicit solution of wave dispersion equation. *Coastal Engineering*, *45*, 71–74. https://doi.org/10.1016/S0378-3839(02)00039-X

Hallermeier, R. J. (1980). A profile zonation for seasonal sand beaches from wave climate. *Coastal Engineering*, *4*, 253–277. https://doi.org/https://doi.org/10.1016/0378-3839(80)90022-8

Hoekstra, P., & Stolk, A. (1990). The dutch coastal zone: An outline of physical processes and coastal morphodynamics. *Journal of Coastal Research*, 358–375. http://www.jstor.org/stable/44868645

Holthuijsen, L. (2010). *Waves in oceanic and coastal waters* (1st ed.). Cambridge University Press.

Longuet-Higgins, M. S., & Stewart, R. W. (1962). Radiation stress and mass transport in gravity waves, with application to 'surf beats'. *Journal of Fluid Mechanics*, *13*(4), 481–504. https://doi.org/10.1017/S0022112062000877

Longuet-Higgins, M., & Stewart, R. (1964). Radiation stresses in water waves; a physical discussion, with applications. *Deep Sea Research and Oceanographic Abstracts*, *11*(4), 529–562. https://doi.org/https://doi.org/10.1016/0011-7471(64)90001-4

Pinault, J., Morichon, D., & Roeber, V. (2020). Estimation of irregular wave runup on intermediate and reflective beaches using a phase-resolving numerical model. *Journal of Marine Science and Engineering*, *8*(12). https://doi.org/10.3390/jmse8120993

Ruggiero, P., Holman, R. A., & Beach, R. A. (2004). Wave run-up on a high-energy dissipative beach. *Journal of Geophysical Research*, *109*.

Senechal, N., Coco, G., Bryan, K., & Holman, R. (2011). Wave runup during extreme storm conditions. *JOURNAL OF GEOPHYSICAL RESEARCH-OCEANS*, *116*. https://doi.org/10.1029/2010JC006819

Stockdon, H., Thompson, D., Plant, N., & Long, J. (2014). Evaluation of wave runup predictions from numerical and parametric models. *Coastal Engineering*, *92*, 1–11. https://doi.org/10.1016/j.coastaleng.2014.06.004

Stockdon, H., Holman, R., Howd, P., & Sallenger, A. (2006). Empirical parameterization of setup, swash, and runup. *Coastal Engineering*, *53*, 573–588. https://doi.org/10.1016/j.coastaleng.2005.12.005

Thornton, E. B., & Guza, R. T. (1982). Energy saturation and phase speeds measured on a natural beach. *Journal of Geophysical Research: Oceans*, *87*(C12), 9499–9508. https://doi.org/https://doi.org/10.1029/JC087iC12p09499

van Gent, M., van Thiel de Vries, J., Coeveld, E., de Vroeg, J., & van de Graaff, J. (2008). Large-scale dune erosion tests to study the influence of wave periods. *Coastal Engineering*, *55*(12), 1041–1051. https://doi.org/https://doi.org/10.1016/j.coastaleng.2008.04.003

Willmott, C. J. (1981). On the validation of models. *Physical Geography*, *2*(2), 184–194. https://doi.org/10.1080/02723646.1981.10642213

A

Wave heights and water levels during the events

Wave heights and wave periods at each location are determined using zero down crossing techniques. The mean square wave height (H_{rms}) and significant wave height ($H_{1/3}$) have been calculated using Equations A.1 and A.2.

$$H_{rms} = \left(\frac{1}{N} \sum_{i=1}^{N} H_i^2 \right)^{1/2} \tag{A.1}$$

$$H_{1/3} = \frac{1}{N/3} \sum_{j=1}^{N/3} H_j \tag{A.2}$$

(A.3)

The duration of each event has been separated into segments of 30 minutes and the characteristic wave heights have been calculated for every segment. Because of the shallow location of the pressure sensors at location 7 and 8, these stations ran dry at certain times. Segments of the data have been removed when the pressure sensors ran dry. The characteristic wave heights of each location are plotted in figures A.1, A.2 and A.4.

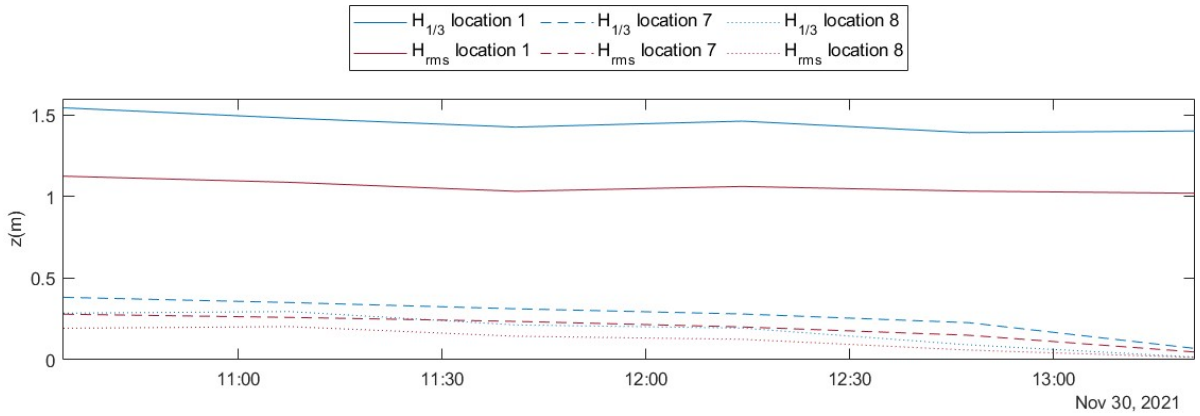

Figure A.1: Wave characteristics on November 30th at all pressure sensor locations.

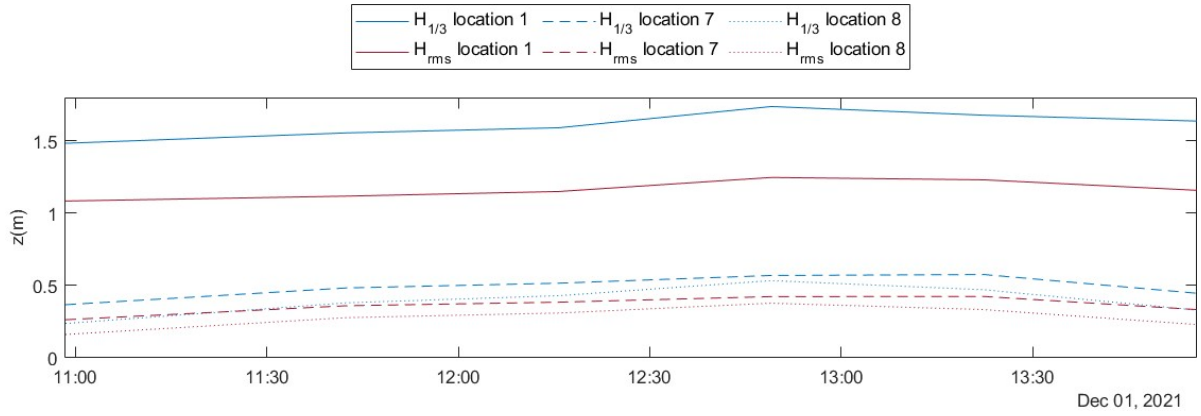

Figure A.2: Wave characteristics on December 1st at all pressure sensor locations.

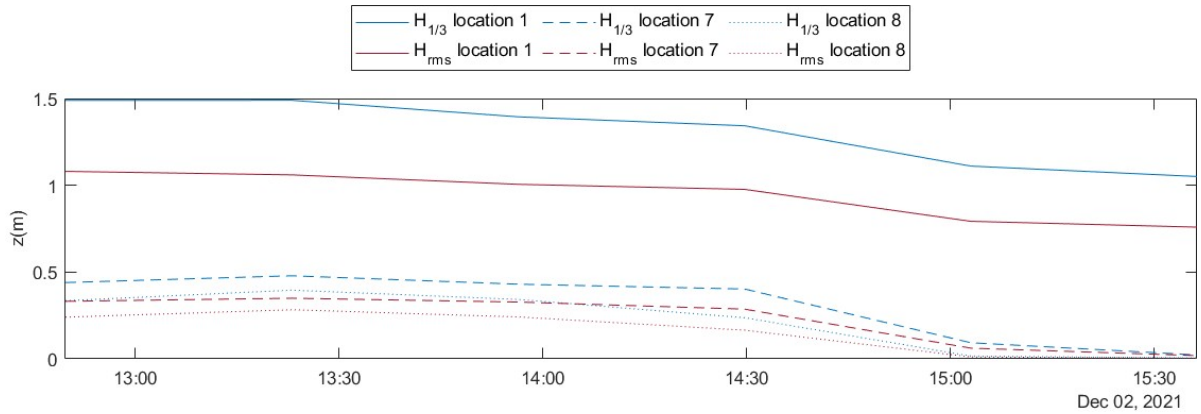

Figure A.3: Wave characteristics on December 2nd at all pressure sensor locations.

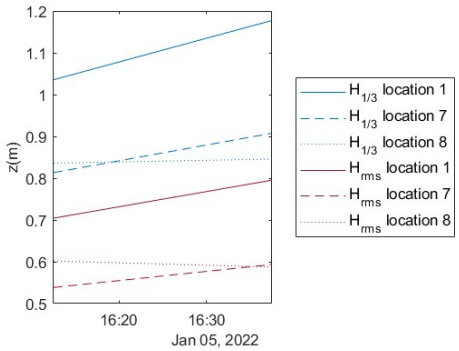

Figure A.4: Wave characteristics on Janury 5th at all pressure sensor locations.

B

Mean wave periods

Wave characteristics, like mean wave periods and significant wave heights, can be calculated from the ED-spectra. The ED-spectra can be characterized by calculating the spectral moments using equation B.1.

$$m_n = \int_0^\infty f^n E(f) \mathrm{d}f \qquad \text{for} \quad n = -1, 0, 1, 2 \tag{B.1}$$

In which m_n is the spectral moment, f is the frequency, n is the order and $E(f)$ is the variance. Characteristic wave periods can be calculated using different combinations of spectral moments. Higher order wave moments give more significance to the higher frequencies in the spectra, and lower order wave moments more significance to lower frequencies. The characteristic wave periods are calculated using equations B.2 and B.3.

$$T_{m_{01}} = f_{m_{01}}^{-1} = \left(\frac{m_1}{m_0}\right)^{-1} \tag{B.2}$$

$$T_{m_{-10}} = f_{m_{-10}}^{-1} = \left(\frac{m_0}{m_{-1}}\right)^{-1} \tag{B.3}$$

In which $T_{m_{01}}$ and $T_{m_{-10}}$ are characteristic mean wave periods, of which the latter gives more significance to the lower frequencies in the spectral domain. Since the primary interest lies in the low frequencies, due to the importance of long waves on the dissipate beach, the latter wave period could give a more reliable estimate for the wave period. Again, looking at the values of the second of December in table B.1, a clear increase in wave period is observed in the nearshore location when compared to the offshore location.

Segment [hh:mm]	Location 1		Location 7		Location 8		Runup camera	
	$T_{m_{01}}$	$T_{m_{-10}}$	$T_{m_{01}}$	$T_{m_{-10}}$	$T_{m_{01}}$	$T_{m_{-10}}$	$T_{m_{01}}$	$T_{m_{-10}}$
November 30								
10:51 - 11:24	5.61	7.33	-	-	-	-	18.11	25.83
11:24 - 11:57	5.44	7.12	-	-	-	-	17.77	23.95
11:57 - 12:31	5.53	7.18	-	-	-	-	19.02	26.67
12:31 - 13:04	5.46	7.32	-	-	-	-	20.73	28.33
13:04 - 13:37	5.26	7.06	-	-	-	-	22.29	29.55
December 1								
10:42 - 11:14	5.27	6.97	-	-	-	-	17.94	24.08
11:26 - 11:59	5.49	7.29	9.61	21.90	-	-	14.42	20.23
11:59 - 12:32	5.64	7.50	9.10	20.94	-	-	14.88	20.33
12:32 - 13:06	5.85	7.93	10.49	24.94	-	-	14.55	20.56
13:06 - 13:39	5.95	8.11	12.42	28.89	-	-	15.14	21.21
13:39 - 14:12	5.75	7.95	14.36	31.22	-	-	16.64	22.64
December 2								
12:33 - 13:06	6.14	8.82	13.06	30.66	-	-	17.66	24.45
13:06 - 13:40	6.18	8.51	11.56	25.45	-	-	16.62	22.09
13:40 - 14:13	6.21	9.03	12.63	27.62	-	-	17.09	23.00
14:13 - 14:46	5.85	7.93	-	-	-	-	-	-5
14:46 - 15:20	5.95	8.11	-	-	-	-	-	-
15:20 - 15:52	5.75	7.95	-	-	-	-	-	-

Table B.1: Characteristic wave periods, $T_{m_{01}}$ and $T_{m_{-10}}$, during the events in [sec]. A clear increase in both wave periods can be seen when going to shoreward sensor locations. This increase can be attributed to the dissipation of the high frequency part of the spectrum, and the transfer of energy of the high frequency region to the low frequency region.

C

Variance density spectra

Energy density spectra can be a useful method when looking at the A method of looking at, and extracting useful parameters from the waterlevel time series ($h(t)$) from the pressure sensor and runup camera data, is to transform the time series to a (one dimensional) variance density spectra (Hereafter named ED-spectra) (Holthuijsen, 2010). This is done by executing a Fourier transformation, but now using the dataset of the waterlevel time series. The dataset is detrended, thus mean waterlevel values are extracted from the dataset and only wave amplitudes are used in the Fourier transform. The variance of each harmonic component is calculated using equation C.1.

$$E(f) = \lim_{\Delta f \to 0} \frac{1}{\Delta f} E\{\frac{1}{2} a^2\} \tag{C.1}$$

In which $E(f)$ is the variance density, Δf is the frequency interval between the harmonic components, and a is the wave amplitude of the harmonics. Equation C.1 is a continuous version of the ED-spectra where the frequency interval approaches zero. Since the used time series is finite, only a discontinuous version of the ED-spectra can be calculated. In this discontinuous time spectra, the frequency interval can be calculated as $\Delta f = 1/D$, in which D is the duration of the time series. Δf stands for the resolution of the discontinuous ED-spectra.

$$E(f_i) = \frac{1}{\Delta f_i} E\{\frac{1}{2} a_i^2\} \tag{C.2}$$

In which $E(f_i)$ is the variance density spectrum for all f_i. However, since the time series is finite, this raw ED-spectrum is quite uncertain due to the variance estimation using one amplitude at each frequency. The error using this method is around the order of 100% (Holthuijsen, 2010), which is too unreliable. To increase certainty within the ED-spectra, the time series can be divided into blocks (p), and applying the Fourier transform to each of these blocks (Holthuijsen, 2010). After the Fourier transform, the ED-spectrum of each of these blocks are averaged. This method reduces the frequency resolution of the time segment, since the new resolution of each block is $\Delta f = 1/(D/p)$, but increases the expected error with, $error = 100\%/p$. This averaging method is called (quasi-) ensemble averaging.

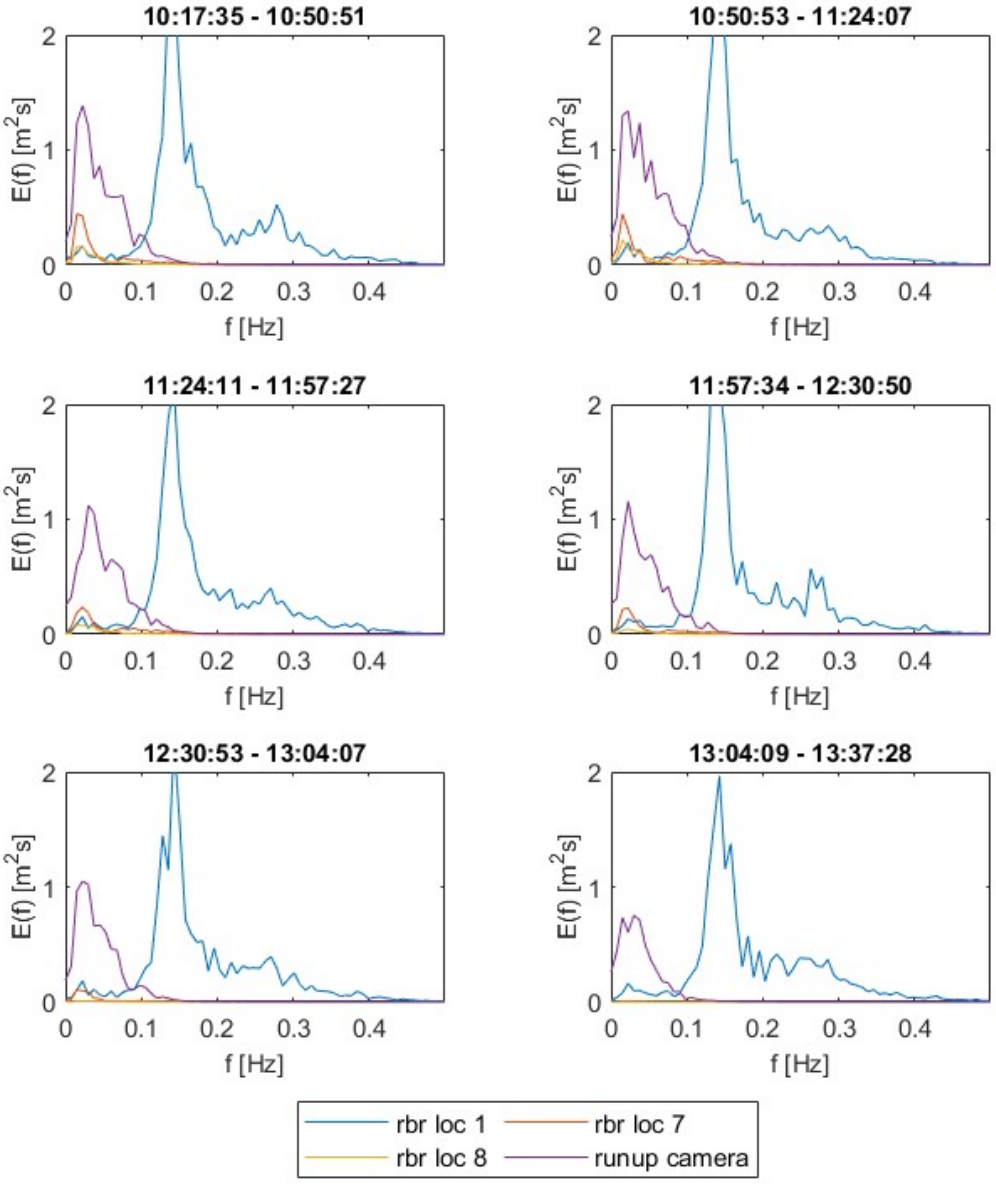

Figure C.1: The figures show the ED-spectra at all locations during the same time segments on November 30th. A clear reduction in the total variance can be seen when comparing the offshore locations to the onshore locations. This reduction is mainly visible in the high frequency part of the spectrum. In low frequencies the spectrum increased. This increase is possibly by the transfer of the energy of the high frequencies to the low frequencies.

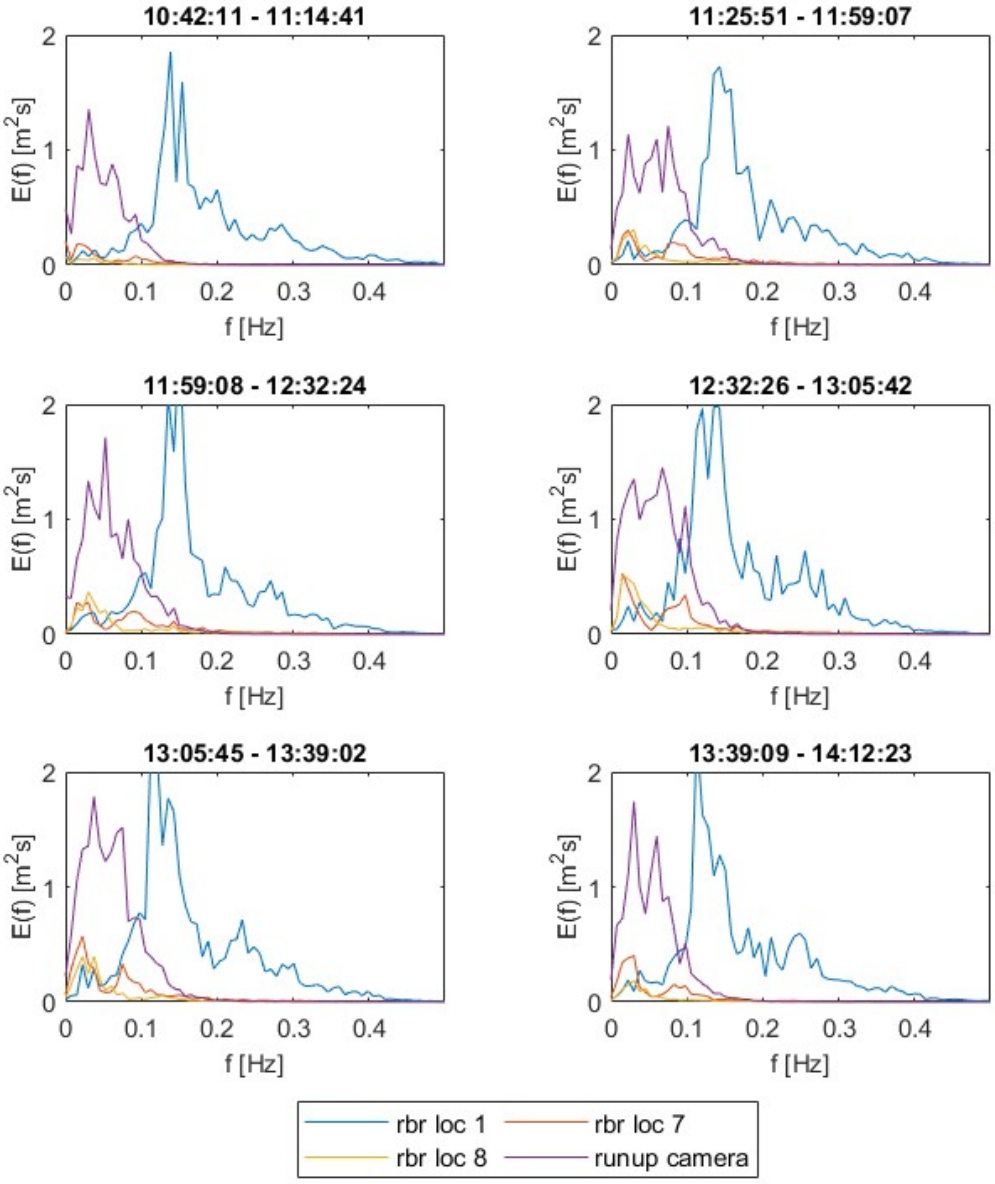

Figure C.2: The figures show the ED-spectra at all locations during the same time segments on December 1st. A clear reduction in the total variance can be seen when comparing the offshore locations to the onshore locations. This reduction is mainly visible in the high frequency part of the spectrum. In low frequencies the spectrum increased. This increase is possibly by the transfer of the energy of the high frequencies to the low frequencies.

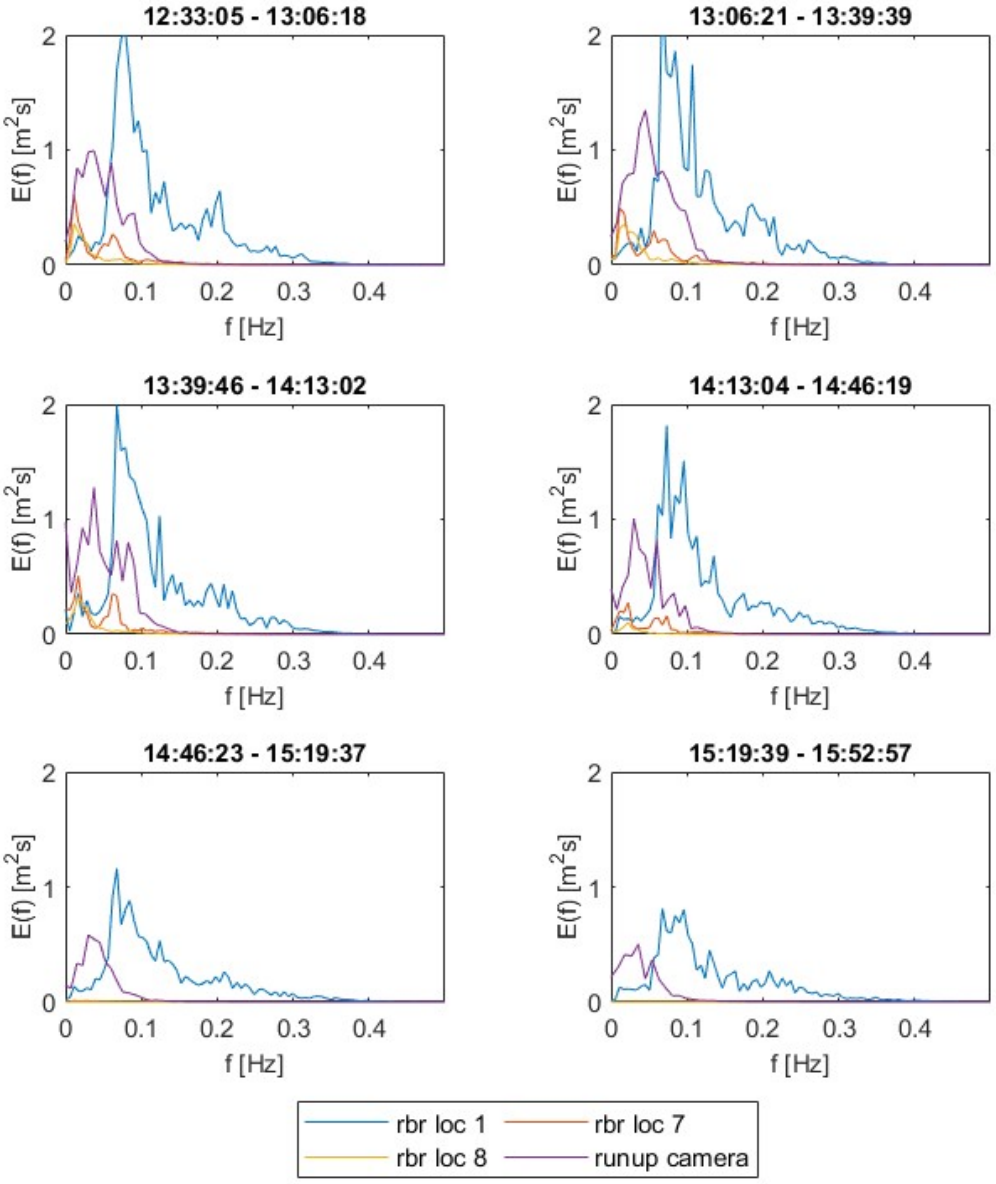

Figure C.3: The figures show the ED-spectra at all locations during the same time segments on December 2nd. A clear reduction in the total variance can be seen when comparing the offshore locations to the onshore locations. This reduction is mainly visible in the high frequency part of the spectrum. In low frequencies the spectrum increased. This increase is possibly by the transfer of the energy of the high frequencies to the low frequencies.

D

Data summary

Data from all nearshore instruments are summarized in Figures D.1, D.2 and D.3. In these Figures, the mean water level above the pressure sensors and (distribution of) the runup heights have been plotted at the top of each Figure. The bottom Figures show the variance density spectra of the pressure sensor and runup camera data. Be careful to look at the axis, since these have been adjusted between L1, L7, L8 and the runup camera in order to visualize the spectra better.

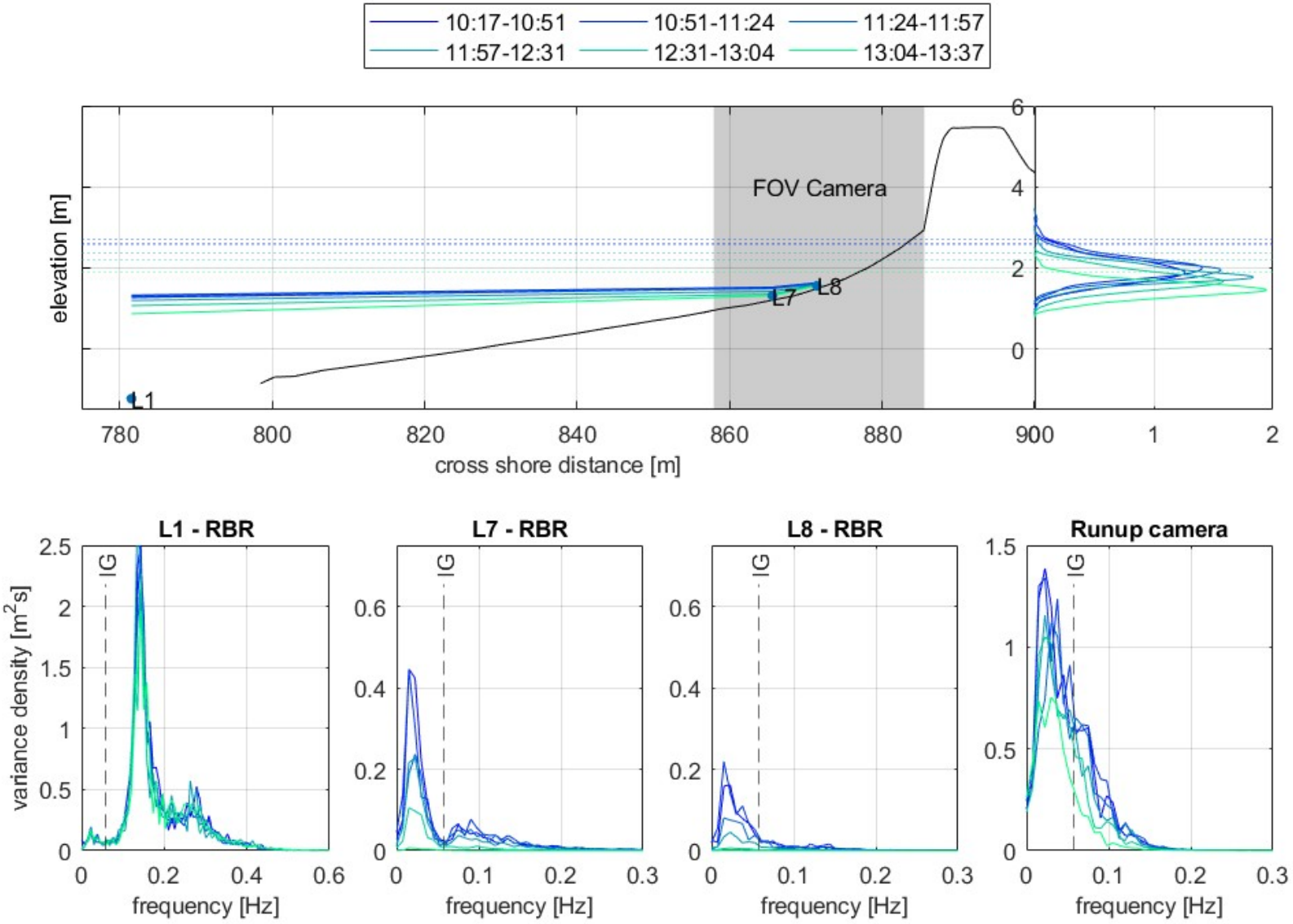

Figure D.1: The figure is a summation of the data on November 30th. The top-left plot shows the beach profile together with the mean water levels at location 1 (L1), location 7 (L7) and location 8 (L8). The gray area shows the FOV of the runup camera. The top right plot shows the runup distributions. The bottom plots show the ED-spectra at each location within the transect.

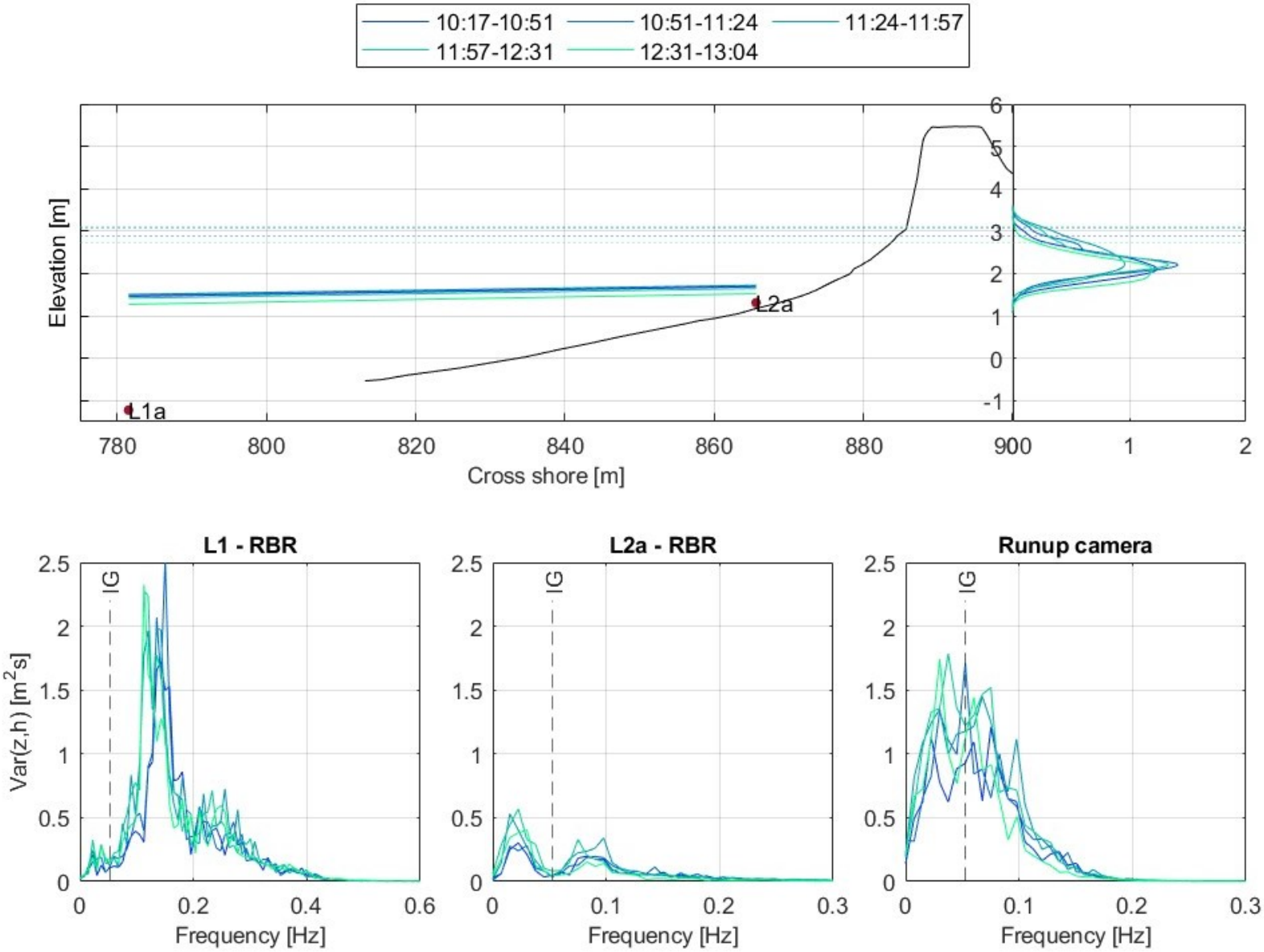

Figure D.2: The figure is a summation of the data on December 1st. The top-left plot shows the beach profile together with the mean water levels at location 1 (L1), location 7 (L7) and location 8 (L8). The gray area shows the FOV of the runup camera. The top right plot shows the runup distributions. The bottom plots show the ED-spectra at each location within the transect.

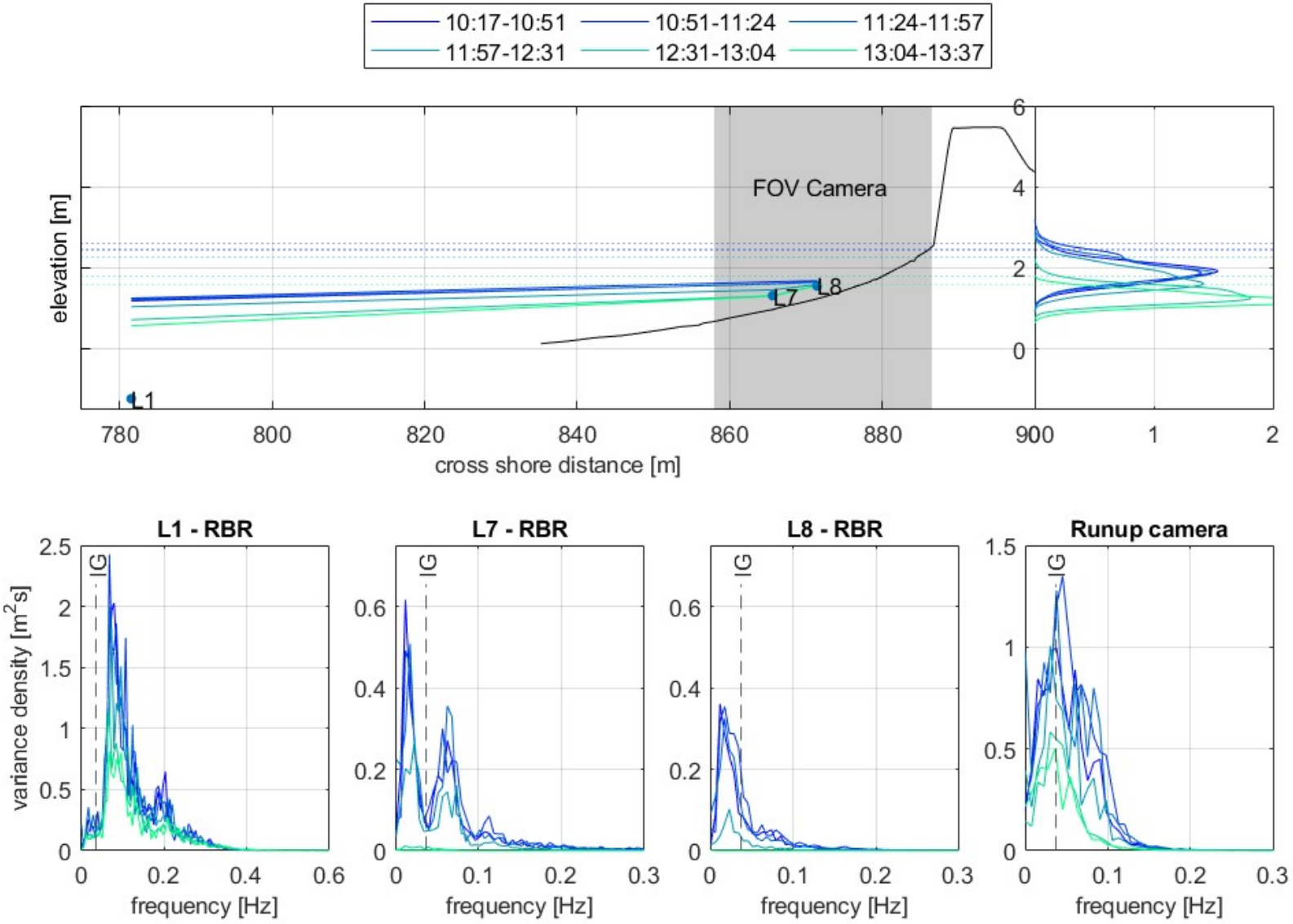

Figure D.3: The figure is a summation of the data on December 2nd. The top-left plot shows the beach profile together with the mean water levels at location 1 (L1), location 7 (L7) and location 8 (L8). The gray area shows the FOV of the runup camera. The top right plot shows the runup distributions. The bottom plots show the ED-spectra at each location within the transect.

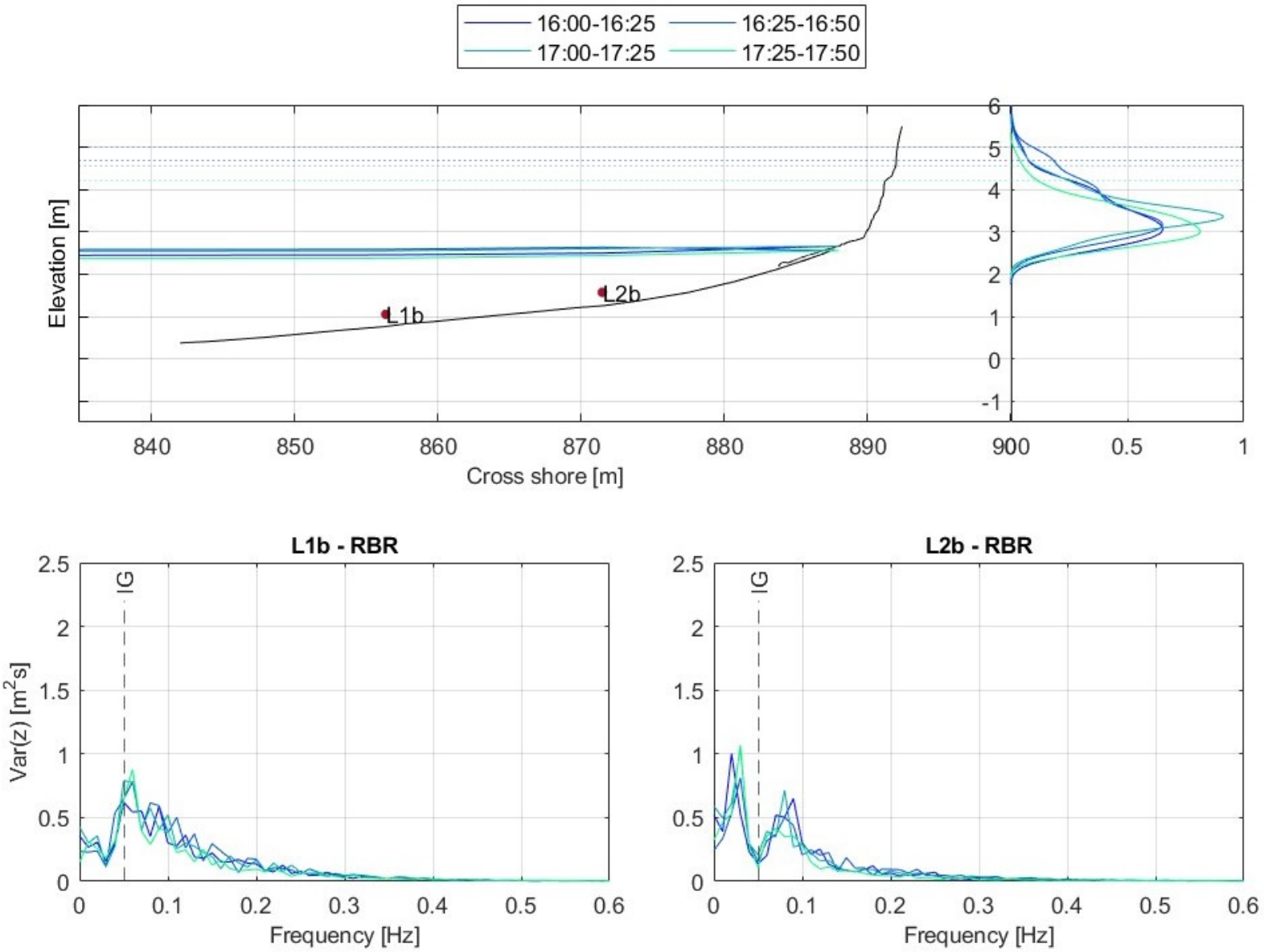

Figure D.4: The figure is a summation of the data on January 5th. The top-left plot shows the beach profile together with the mean water levels at location 1 (L1), location 7 (L7) and location 8 (L8). The gray area shows the FOV of the runup camera. The top right plot shows the runup distributions. The bottom plots show the ED-spectra at each location within the transect.

E

Runup heights

All the runup distribution during all events can be found in this Appendix.

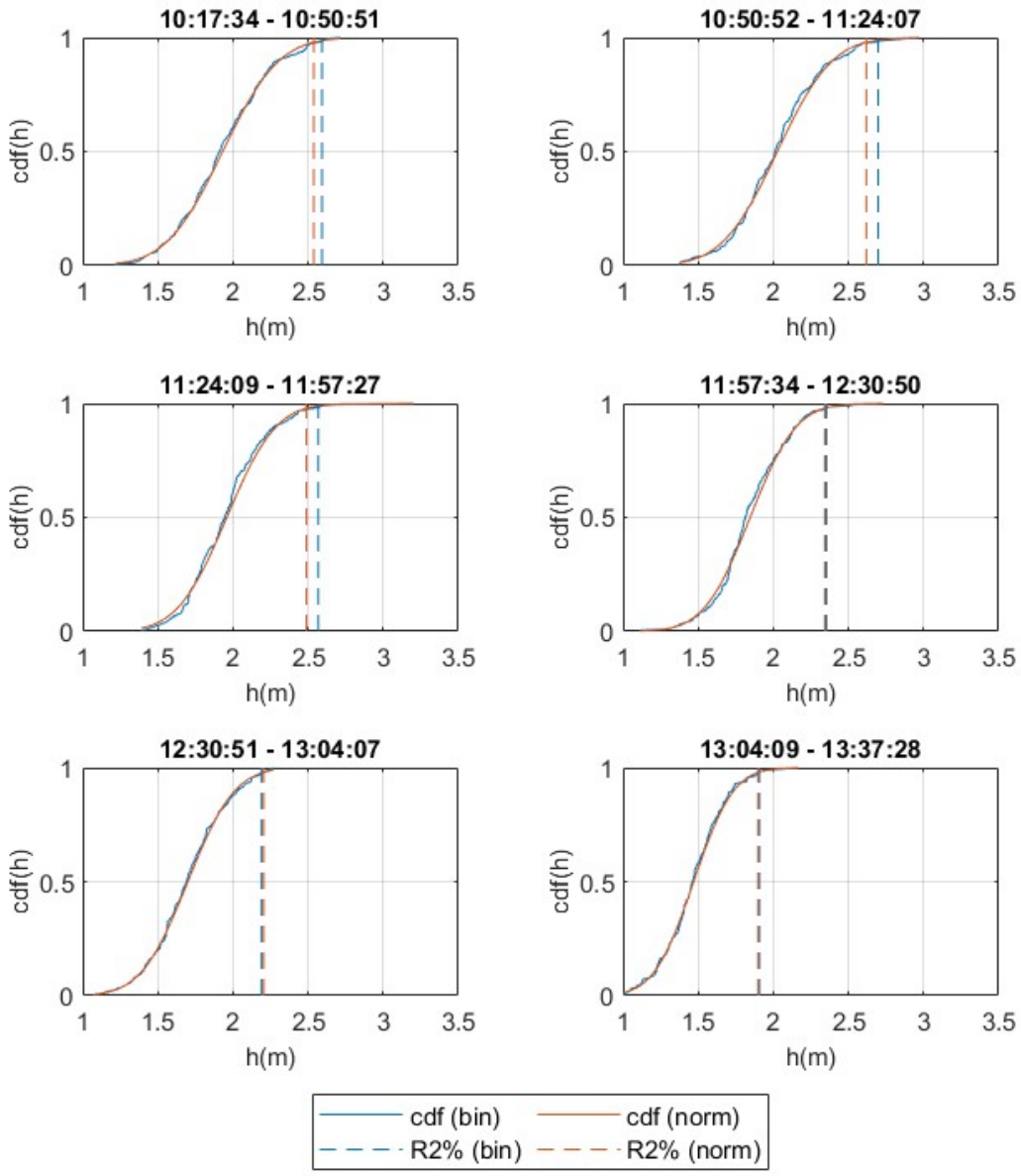

Figure E.1: The distribution of runup during the swash conditions on November 30th, with the empirical distribution in red and a fitted normal distribution in blue. The vertical lines indicate the $R_2\%$ height relative to NAP, so $R_2\% + \mu_{wave} + \mu_{wind} + \mu_{tide}$.

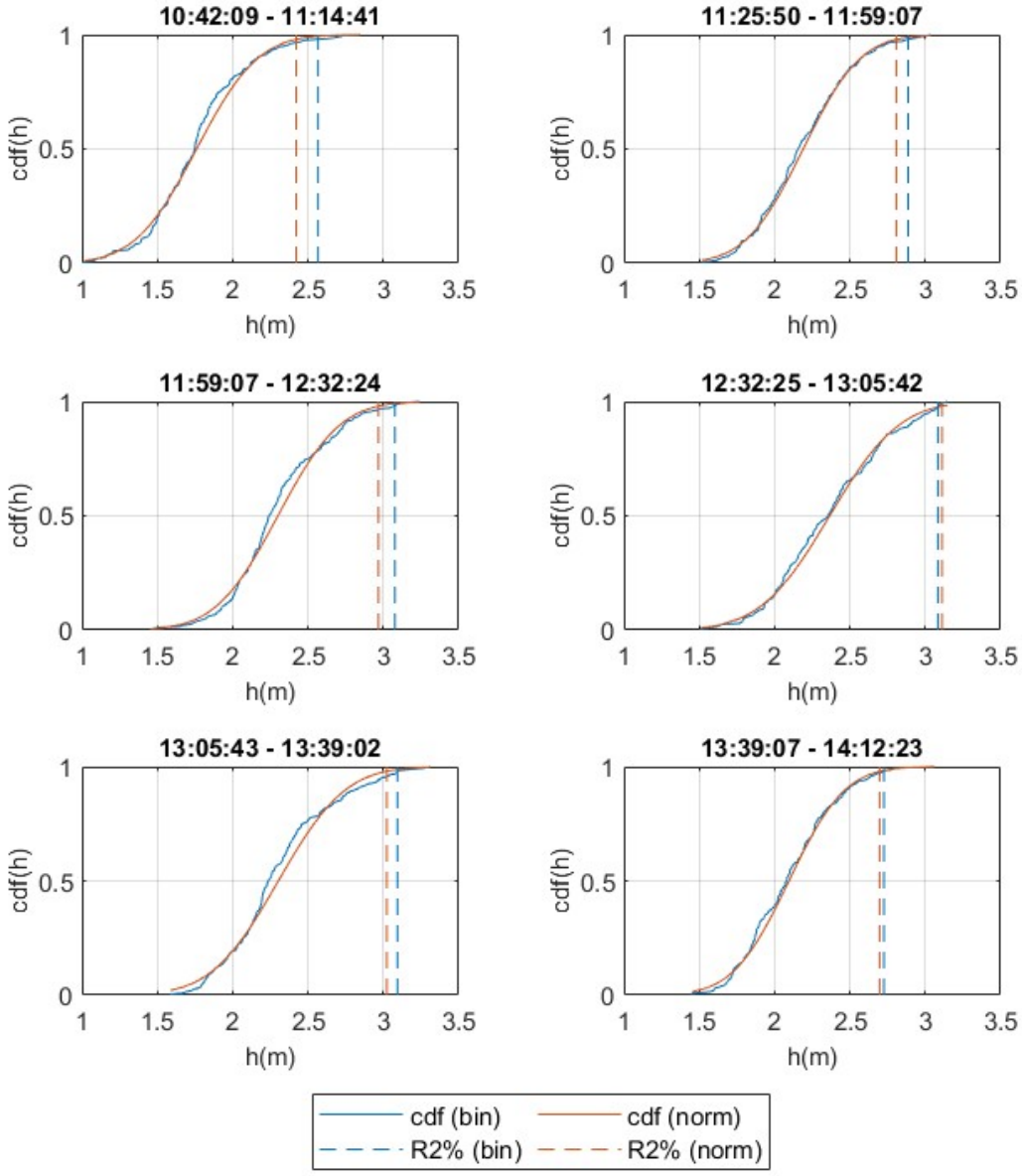

Figure E.2: The distribution of runup during the swash conditions on December 1st, with the empirical distribution in red and a fitted normal distribution in blue. The vertical lines indicate the $R_2\%$ height relative to NAP, so $R_2\% + \mu_{wave} + \mu_{wind} + \mu_{tide}$.

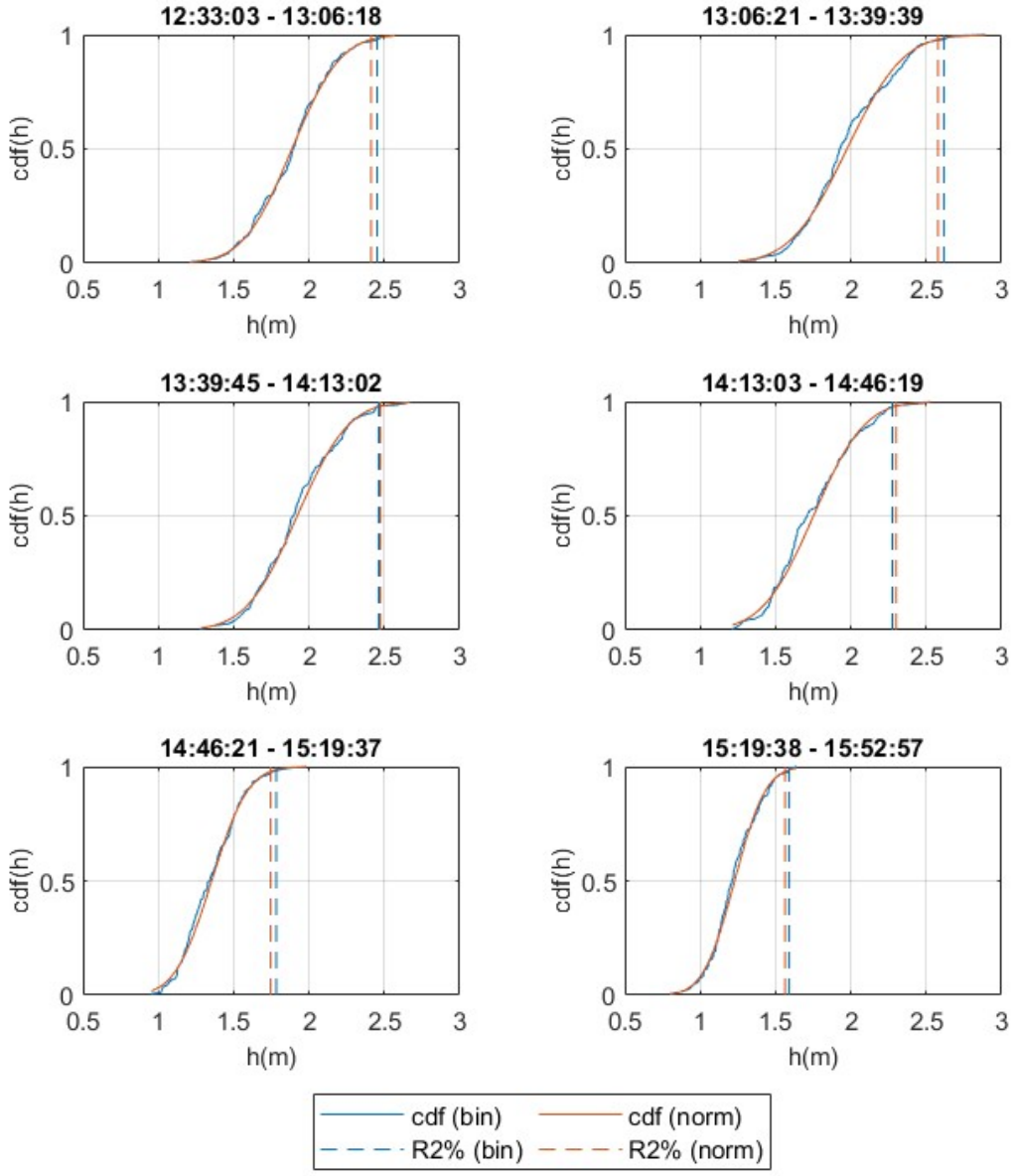

Figure E.3: The distribution of runup during the swash conditions on December 2nd, with the empirical distribution in red and a fitted normal distribution in blue. The vertical lines indicate the $R_2\%$ height relative to NAP, so $R_2\% + \mu_{wave} + \mu_{wind} + \mu_{tide}$.

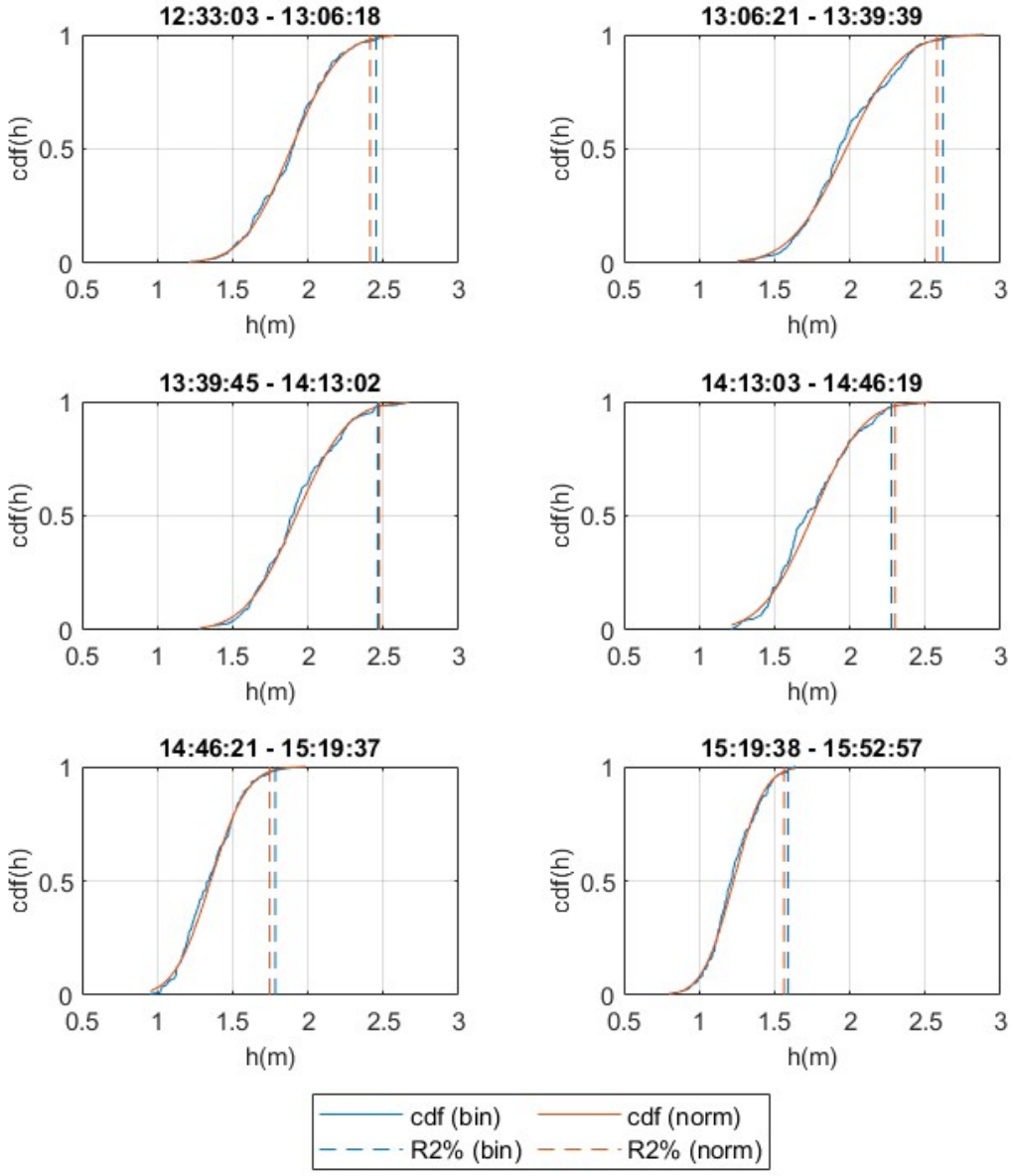

Figure E.4: The distribution of runup during the swash conditions on January 5th, with the empirical distribution in red and a fitted normal distribution in blue. The vertical lines indicate the $R_2\%$ height relative to NAP, so $R_2\% + \mu_{wave} + \mu_{wind} + \mu_{tide}$.

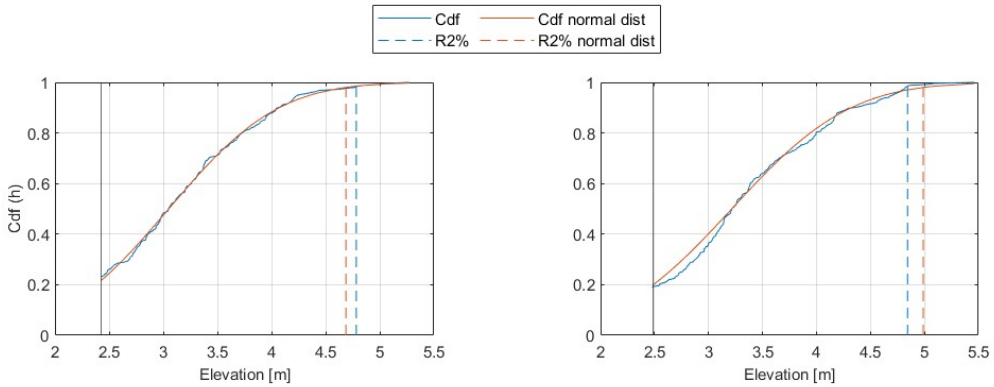

Figure E.5: The distribution of runup during the swash conditions on January 5th, with the empirical distribution in red and a fitted normal distribution in blue. The vertical lines indicate the $R_2\%$ height relative to NAP, so $R_2\% + \mu_{wave} + \mu_{wind} + \mu_{tide}$. The left plot is the distribution from 16:00 to 16:25 and the right plot is the distribution form 16:25 to 16:50.

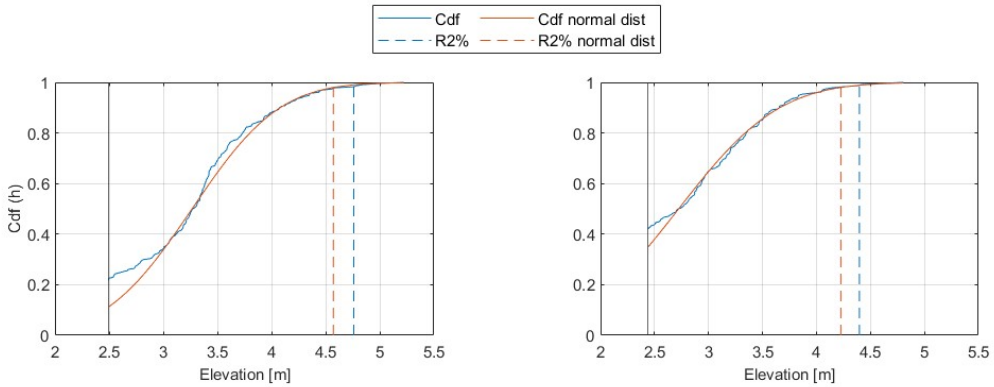

Figure E.6: The distribution of runup during the swash conditions on January 5th, with the empirical distribution in red and a fitted normal distribution in blue. The vertical lines indicate the $R_2\%$ height relative to NAP, so $R_2\% + \mu_{wave} + \mu_{wind} + \mu_{tide}$. The left plot is the distribution from 17:00 to 17:25 and the right plot is the distribution form 17:25 to 17:50.